Justus - Liebig - University Giessen

Phase Transitions in Three-Dimensional Complex Plasma

Dissertation zur Erlangung des Doktorgrades der Naturwissenschaften
(Dr. rer. nat.)

Benjamin Steinmüller

Supervised by
Prof. Dr. Markus H. Thoma

June 25, 2018

Prudens quaestio dimidium scientiae.
(Half of science is asking the right questions.)

Roger Bacon (1214 - 1292)

Zusammenfassung

Das Thema dieser kumulativen Dissertation ist die experimentelle Beobachtung und die Beschreibung der Kristallisation und der Entmischung von dreidimensionalen komplexen Plasmen. Komplexe Plasmen sind Niedertemperaturplasmen, in denen genau definierte Mikropartikel hinzugefügt wurden. Die Partikel laden sich durch Elektronen- und Ionenflüsse auf ihre Oberfläche elektrisch auf. Aufgrund ihrer Ladung können die Teilchen regelmäßige Strukturen vergleichbar mit Kristallen ausbilden. Eine Ordnung analog zu Fluiden ist ebenfalls möglich. Die typische Größen- und Zeitskalen in einem komplexen Plasma, erlauben es Übergänge zwischen unterschiedlichen Phasen auf einer Partikelebene direkt zu beobachten. Aus diesem Grund werden sie oft als Modellsysteme für Phasenübergänge genutzt.

In der ersten Veröffentlichung [1] wird der Einfluss des Gasdruckes auf die Kristallisation eines dreidimensionalen komplexen Plasmas unter Gravitation untersucht. Das *Skalarprodukt der Minkowski Struktur Metrik* wurde hier entwickelt, um den Aggregatzustand in dem sich die Partikel befinden zu bestimmen. Daneben wurden zahlreiche weitere bekannte Kristallisationskriterien eingesetzt. Alle Kriterien zeigten das gleiche Bild: Bei niedrigem Druck war das System im kristallinen, bei hohem Druck im flüssigem Zustand. Das steht im Gegensatz zu bisherigen Experimenten sowohl unter Gravitation als auch unter Mikrogravitation. Als Grund für diese Beobachtung wurden die zunehmende Bedeutung von Stößen zwischen Ionen und Neutralgas in der direkten Umgebung der Partikel sowie eine verringerte Debye Länge identifiziert.

Die zweite Veröffentlichung [2] ist eine logische Erweiterung der Ersten. In dieser Publikation wird bei unterschiedlichen Gasdrücken das Skalarprodukt der Minkowski Struktur Metrik genutzt, um den Ort der Partikel, die sich im festen bzw. im flüssigen Zustand befinden, zu visualisieren. Hierdurch konnte zusätzlich gezeigt werden, dass der Kristallisationsgrad der Partikelwolke von unten nach oben abnimmt.

In den ersten beiden Veröffentlichungen wurden die genauen Bedingungen, unter denen sich ein komplexes Plasma in einem kristallinen Zustand befindet, bestimmt. Dieses Wissen erlaubte die dritte Publikation [3], in der der Kristallisationsvorgang eines komplexen Plasmas unter Gravitation zeitaufgelöst analysiert wurde. Während des Kristallisationsprozesses wurden tomographische Scans durchgeführt, um die Entwicklung fester Domänen zu identifizieren. Die berechnete fraktale Dimension dieser Domänen ergab, dass der Erstarrvorgang durch epitaktisches Wachstum und diffusions begrenztes Wachstum dominiert wurde.

Die vierte Publikation [4] handelt von dem Entmischen zweier Partikelsorten innerhalb eines komplexen Plasmas. Unter Gravitation würden die Partikelsorten aufgrund der Massendifferenzen in unterschiedlichen Höhen innerhalb des Plasmas levitieren. Aus diesem Grund wurden die Experimente unter Milligravitation während eines Parabelfluges durchgeführt. Der Übergang zwischen einem Ein-Phasen zu einem Zwei-Phasen System konnte beobachtet und beschrieben werden.

Abstract

This cumulative dissertation discusses the experimental observation and description of crystallization and demixing processes in a three-dimensional complex plasma. Complex plasmas are low temperature plasmas to which well-defined microparticles have been added deliberately. These particles are charged by electron and ion fluxes toward their surfaces. Charged particles can then create regular structures similar to a crystal or arrange comparable to fluids. The typical size and time ranges in a complex plasma allow for observations of changes in form of distinct phases on a single-particle level. This is why they are often used as model systems for phase transitions.

In the first publication [1], the influence of neutral gas pressure on the crystallization of a three-dimensional complex plasma under gravity conditions was considered. The *scalar product of the Minkowski structure metric* was developed in this publication to identify the particles' state of aggregation. Besides this method, various well-known crystallization criteria were applied. All criteria revealed the same picture: the system was in the crystalline state at low pressure and in the liquid state at high pressure. This stands in contrast with previous experiments under gravity as well as under microgravity conditions. The increasing role of collisions between ions and neutrals in the vicinity of the particles as well as a decreased Debye length were identified as responsible for this observation.

The second publication [2] is a logical extension of the first one. In this publication, the scalar product of the Minkowski structure metric was applied to visualize the location of the particles in the solid state and in the liquid state at different pressure rates. Hereby, it could be shown additionally that the degree of crystallization was decreasing from the lower to the upper part of the particle cloud.

After the first two publications, the detailed conditions under which complex plasmas are highly ordered were determined. This knowledge facilitated the third publication [3]. In this publication, the crystallization process of a complex plasma under gravity conditions was analyzed in a time-resolved manner. During crystallization, tomographic scans were performed to identify the evolution of solid clusters. The calculated fractal dimension of these clusters showed that the solidification process was dominated by epitaxial growth and diffusion-limited growth.

The fourth publication [4] deals with the demixing of two particle types in a complex plasma. Due to the mass discrepancies, the particles would levitate at different heights in the plasma under gravity conditions. This is why the experiments were performed under milligravity during a parabola flight. The transition from a single phase into a two-phase system was observed and described.

Contents

List of Figures

1 Introduction

Complex or dusty plasmas consist of electrons, ions, neutrals, and charged solid particles, typically in a range of nano- or micrometers. The term *complex plasmas* mainly describes experiments in which monodisperse, spherical particles are deliberately inserted into the plasma[1]. By contrast, the particles in dusty plasmas are unintentionally added or formed in the plasma, thus coming in many of shapes and sizes. The different charging processes of the particles determine weather they are positively or negatively charged. In the case of dominant emission processes, such as secondary electron emission or photoeffect, the charge is positive. If charging is defined by electron and ion fluxes onto the surface, the particles are typically negatively charged. This is why the absolute charge of the particles is commonly given by a complicated interplay of photons, ions, electrons, and neutral gas atoms of the background plasma.

Although complex and dusty plasmas are diverse, they can be divided into three main types. The first type of complex or dusty plasma is industrial, the second naturally occurring (primarily in an astrophysical or atmospherically context), and the third type are particular physical experiments, often used as model systems.

1.1 Dusty Plasmas in Industrial Contexts

Processes involving plasma are growing more and more important in industrial contexts. While the size of the plasma-etched structures (e.g., in semiconductor industry) decreases, contamination through solid particles is an increasing issue. Solid macroscopic particles can be released by sputtering processes or grow directly in the discharge. Since their diameters exceed the typical length of the desired structure, these particles are able to cause shortcuts on electric circuits. Furthermore, charged particles with a typical size can gain enough kinetic energy in a plasma etching device to mechanically destroy the desired structures [7–9].

In a stellarator or a tokamak, a plasma is confined in torus by strong electromagnetic fields to produce energy via controlled fusion. Dust is produced in these fusion reactors via evaporation and sublimation out of material from the wall. These particles migrate into the plasma and charge, creating a dusty plasma. This process of deposition and re-deposition changes the surface properties and stability. Negatively charged dust particles confined in the edge plasma can grow further (up to a size of 1 μm) via agglomeration. Since a fraction of the dust grains is ferromagnetic or paramagnetic, it interacts with the existing magnetic field. A contamination with dust can impede the plasma startup, and once in the plasma, dust is considered responsible for plasma disruptions [10–13].

A controlled growth of particles, in an appropriate discharge, can also have desirable effects. Solid carbon particles, for instance, grow in a mixture of a buffer gas (e.g., argon) and a reactive gas (e.g., acetylene or methane). The produced particles have a well-defined diameter of nano- to micrometers [14–16]. In sintering processes, the plasma

---

[1]In some complex plasma experiments, different particle types are added (see, e.g., chapter 8). It should also be noted that experiments with nonspherical particles exist [5, 6].

treatment of metallic powder improves the physical properties of the product [17]. Finally, complex plasmas play a key role in many other applications, as well (see, e.g., [18]).

1.2 Dusty Plasmas in Space and Atmosphere

Dusty plasmas are widespread in the astrophysical realm, e.g., in planetary rings [19–22], interstellar clouds [21–23], comets tails [21, 24, 25], and as part of the formation of stars or planets [23]. Although dust represents only a small fraction of mass, it plays an important role in chemistry, dynamics, and thermodynamics within astrophysics. For example, during the collapse of a gas cloud and the formation of a star, the cloud gets optical thick for visible radiation. The cloud is heated by the release of gravitational energy, which cannot be carted away by direct radiation. Without any cooling process, the kinetic energy of the gas counters gravity, thereby ending the collapse. Dust particles inside the cloud emit infrared radiation, which the cloud is transparent for, thus reducing the energy of the cloud and maintaining the process of collapse [23, 26, 27].

The surface of a macroscopic solid particle can act as a catalyst for the creation of some chemical compounds. Since the formation of molecular hydrogen from two single atoms is radiation-free, a third collision partner is needed to dispose of the energy [28].

The sun's UV radiation ionizes the gases in the planetary rings of the outer planets Jupiter, Saturn, Uranus, and Neptune. Pictures from *Voyager 2* show the presence of altering radial 'spokes' in Saturn's ring. These spokes are lighter in forward scattered light and darker in backward scattered light. They were found to consist of solid low charged particles with a maximum size of a few micrometers, showing highly dynamical behavior [19–21, 29–33].

If gas flows out from the surface of comets, it can release larger dust particles. When this gas becomes ionized by UV light or by free electrons, the charged particles can create a so-called coma, i.e., a dusty plasma in the vicinity of the comet [21, 24, 25, 34].

Furthermore, a dusty plasma can be observed in the earth's atmosphere. Small icy crystals in the partly ionized atmosphere can create night shining (or noctilucent) clouds at a height of about 80 km. These clouds are visible when illuminated by the sun positioned below the horizon [35, 36]. Dusty plasmas are also considered responsible for radar back scattering in the atmosphere [37].

1.3 Complex Plasmas as Model Systems

In real physical systems, dynamic processes, such as phase transitions, take place within size and time ranges that make direct observation difficult, if not impossible. Thus, there is a need for model systems. Mainly colloidal dispersions have been applied for this purpose in the past, which, however, have the issue to be overdamped [38, 39]. To overcome these limitations, complex plasmas with a low damping rate are used. Since the diameter of the particles ($\sim \mu$m) is negligible compared to the interparticle distances (~ 0.1 mm), a complex plasma is optical thin. This means that even extended three-dimensional systems with up to hundreds of thousands of particles are still transparent,

allowing for the observation of dynamics up to an individual particle level. Depending on external and internal conditions, the particles can arrange periodically, similar to crystalline structures, or in a disordered manner, similar to a fluid or gas.

In addition, experiments with complex plasmas are easily manageable. A typical experimental setup is small, and customary cameras are sufficient to observe the particles, which are illuminated by a laser. To gain the position of particles in two or three dimensions, a range of techniques other than the tomographic scan (see chapter 4.2) have been developed, e.g., different laser colors [40, 41], bragg reflections [42], stereoscopy [43], and interferometer [44].

Various physical phenomena can be simulated with complex plasmas, including a direct measurement of the velocity of dislocations in crystalline structures [45, 46], wave propagation in the solid state and liquid state [47, 48], heat transfer and the role of the involved phonons [49, 50], and crystallization as well as the melting process, i.e., the transitions between a high and a low ordered state (see chapter 3.1). Molecular dynamic simulations predict a triple point between different crystal structures and the liquid state in complex plasmas [51]. In phase diagrams, a critical point constitutes the end point of the phase transition line for liquid-gas transition. Beyond this critical point, the system becomes a supercritical fluid. This critical point in experimental complex plasma is still an object of ongoing research [52].

When at least two distinguishable particle types are inserted into the discharge, it becomes possible to analyze the demixing processes on a single-particle level (see chapter 8).

The specific interaction between the particles and the background can give complex plasma a non-Newton nature. When only the particles are considered, Newton's third law *actio est reactio* is no longer fulfilled[2]; for example, a layer of particles can exert a force on a lower level via supersonic ions, where a counterforce does not exist (see chapter 6.2). In addition to this violation of Newton's third law, the viscosity of a complex plasma also often shows a non-Newtonian nature. This behavior allows for some remarkable studies in complex plasma, based on its non-Newtonian and non-Hamiltonian nature [53–59]. As an example for a non-Hamiltonian system simulated by a complex plasma, electrorheological fluids, which change their flow behavior in an electric field, should be mentioned [4].

---

[2]If all species are taken into account (i.e. including the ions, electrons, and neutral gas atoms), the system naturally follows Newton's laws of motion.

2 Important Terms and Effects

For a better understanding of the later observations, the most important physical information on the individual as well as collective effects of a complex plasma are introduced in this chapter.

2.1 Charging of Micro-Particles

To understand the behavior of the microparticles, it is crucial to consider their charge. Due to it, the particles interact with external electromagnetical fields, with ions and electrons of the background plasma, and with each other. In complex plasmas, the charging process is typically dominated by electron and ion fluxes onto the surface of the particle.

In a low temperature plasma, the electrons have a higher velocity than the ions, due to their lower mass and higher temperature. As a result, the electron flux I_e toward the surface of a particle excels the ion flux I_i, charging the particle negatively. Thus, the electrons are rejected, while the ions are attracted, until the fluxes balance each other, which typically occurs a few microseconds after the particles are injected. The charge of a particle Q remains constant

$$\frac{dQ}{dt} = I_i + I_e = 0. \tag{1}$$

Here, $\frac{dQ}{dt}$ is the temporal derivative of the particle charge. The most frequently applied method of describing charging by electron and ion flux is the orbital motion limited (OML) theory [60]. The OML theory is based on four assumptions - namely, (i) no barriers exist in the effective potential, (ii) the particle is isolated; in other words, the interparticle distance is high enough that other particles do not influence the trajectories of the electrons and ions in the vicinity of the particle, (iii) there are no collisions present involving electrons or ions on their way toward the particle, (iv) all electrons and ions that reach the particle stick to its surface.

The electron flux on a particle is then given by

$$I_e = r_p^2 \pi e n_e \left(\frac{8k_B T_e}{\pi m_e}\right)^{1/2} \exp\left(\frac{e\phi_S}{k_B T_e}\right) \tag{2}$$

with the radius of the particle r_p and elementary charge e. The surface potential is denoted by $\phi_S = Q/r_d < 0$. The densities of electrons and ions are n_e and n_i, respectively. The electron mass is m_e, and m_i is the ion mass. The respective thermal energies of the electrons and ions are $k_B T_e$ and $k_B T_i$.

The ion flux on a particle is given by

$$I_i = r_p^2 \pi e n_i \left(\frac{8k_B T_i}{\pi m_i}\right)^{1/2} \cdot \left(1 - \frac{e\phi_S}{k_B T_i}\right). \tag{3}$$

In equilibrium, the charge of a particle can be calculated by

$$Q \approx C \frac{4 r_p \pi \epsilon_0 k_B T_e}{e^2} \ln \left[\frac{n_i}{n_e} \left(\frac{m_e T_e}{m_i T_i} \right)^{1/2} \right]. \tag{4}$$

In a wide range of T_e/T_i for argon $C \approx 0.73$ [61], and ϵ_0 denotes the vacuum permittivity. Following (4), in a typical discharge, particles with a diameter of few micrometers carry charges of $10^4 \, e - 10^5 \, e$.

In a collision between an ion and a neutral gas atom, the ion can lose its momentum and angular momentum. If this happens in the vicinity of a particle, the slow ion has a higher probability of reaching the surface of the particle. This is why the absolute charge of the particles decreases for a high collision rate, and the OML theory is only valid for small pressures [62–67].

2.2 Coupling Parameter

The ratio of two important lengths of a complex plasma, the mean distance between the particles Δ and the Debye length λ_D, is given by the dimensionless parameter κ,

$$\kappa = \Delta/\lambda_D. \tag{5}$$

For a quasineutral plasma with a much higher electron temperature than ion temperature ($T_e \gg T_i$), the Debye length is given by

$$\lambda_D \approx \sqrt{\frac{\epsilon_0 k_B T_i}{e^2 n_i}}. \tag{6}$$

The coupling parameter Γ is defined by the ratio of screened potential energy of interacting neighboring particles, and their kinetic energy, given for an isotropic plasma by

$$\Gamma = \frac{Q^2}{4\pi\epsilon_0 \Delta k_B T_p} \exp(-\kappa). \tag{7}$$

Here, $k_B T_p$ is the thermal energy of the particles. The order of Γ defines the behavior of the particles; for $\Gamma \to 0$, the particle behavior is defined by their kinetic energy, the interaction is comparable to an ideal gas. For $\Gamma > 1$, the interaction between two particles exceeds their kinetic energy, in this case they are denoted as *strongly coupled*. At higher values of the coupling parameter, the particles arrange in periodic structures (see chapter 3.1).

2.3 Forces on a Particle

The five main forces acting on a particle in a typical experiment can be divided into two groups, namely the charge depending and the non-charge depending forces. The Lorentz force and the ion drag make up the former, the neutral gas drag, gravity, and the thermophoretic force the latter group. Note that besides these main forces, additional ones may also occur under certain conditions, such as the radiation force induced by strong lasers [68–70].

2.3.1 Electromagnetic Forces

Consider a particle with no dipole moment in an electric field $\mathbf{E}$, moving with the velocity $\mathbf{v}$ in a magnetic field $\mathbf{B}$. In this case, the Lorentz force is given by

$$\mathbf{F}_\mathrm{L} = Q\mathbf{E} + Q(\mathbf{v} \times \mathbf{B}). \tag{8}$$

Since in most applications no significant magnetic field exists, the second term is commonly neglected. Within the quasineutral bulk of the plasma, the majority of a constant external electric field is screened. This is why the highest electric fields are located within the sheath.

2.3.2 Ion Drag

The ion drag is given by the rate of momentum that ions transfer to the particle, while moving relatively to it. It plays an important role in some of the most remarkable effects in complex plasma, including the creation of dust voids [71, 72], dust vortices [73, 74], and the rotation of the particle cloud under the influence of a weak magnetic field [75, 76]. The ion drag force $\mathbf{F}_i$ can be written as

$$\mathbf{F}_i = \mathbf{F}_\mathrm{coll} + \mathbf{F}_\mathrm{coul}. \tag{9}$$

Here, $\mathbf{F}_\mathrm{coll}$ is the ion force transferred by direct collision between the positive ions and the negative charged particle. The force which the ions exert on the particles via the Coulomb interaction without reaching its surface, is $\mathbf{F}_\mathrm{coul}$. Owing to the highly non-linear interplay of the deformation of the particle screening, in addition to the role of ion-neutral collisions, the ratio of the relative particle velocity to the sound speed of the ions, the finite size of a particle, the mean free path of the ions, and the screening length, etc., a consistent and detailed description of the ion drag is still an object of ongoing research. Further information about the ion drag under certain conditions is given in references [77–80].

Due to the high ratio of ion to electron mass, an electron transfers significantly less momentum to the particle than an ion in a collision. Hence, the electron drag is mainly neglected, even in most low temperature plasmas, where the electrons have a typical kinetic energy of a few eV and the ions of roughly $0.025\ eV$.

2.3.3 Neutral Gas Drag

If a particle moves with a relative velocity $\mathbf{v}_\mathrm{rel}$ to the background gas, the neutral gas drag appears, pointing toward the opposite direction. In contrast to the ion drag, the cross section is proportional to the geometric size of the particle, since the neutral components of the gas interact only via direct collisions. Assuming that the mean free path of the neutrals from the background gas is long compared to the particle size, and the relative velocity is small compared to the thermal speed (both conditions are fulfilled in typical

low pressure complex plasma experiments), the neutral gas drag can be determined by the Epstein drag force [81] given by

$$\mathbf{F}_{\text{drag}} = -\frac{4\pi}{3}\delta m_n n_n \bar{v}_{\text{th},n} r_d^2 \mathbf{v}_{\text{rel}}. \tag{10}$$

The mass of the gas atoms (or neutral molecules) and their density are m_n and n_n, respectively. The thermal velocity of the gas is denoted by $\bar{v}_{\text{th},n}$. For elastic scattering $\delta = 1$, and for diffuse scattering $\delta \approx 1.4$; experiments indicate $\delta \approx 1.4$ [82].

2.3.4 Thermophoretic

The thermophoretic force occurs, if a temperature gradient exists; e.g., through heating and cooling of opposite parts of the setup. Neutral gas atoms from the colder side have a lower thermal velocity than gas atoms from the hotter side. In collisions, faster (hotter) atoms transfer more momentum to the particle than slower (colder) ones. In sum, a force directed toward the colder side is created, given by [83]

$$\mathbf{F}_{\text{th}} = -\frac{8}{3}\frac{r_d^2}{\bar{v}_{\text{th},n}}\kappa_n \frac{\partial T}{\partial \mathbf{x}}. \tag{11}$$

The temperature gradient is $\partial T/\partial x$, and the coefficient for thermal conductivity κ_n depending on the gas. For mono-atomic, ideal gases, the thermophoretic force can be written as [83]

$$\mathbf{F}_{\text{th}} \approx -3.33\frac{k_B r_d^2}{\sigma_{\text{gas}}}\frac{\partial T}{\partial \mathbf{x}}. \tag{12}$$

The cross section for atomic scattering for the gas is σ_{gas}. Note that the thermophoretic force in this case is independent from the absolute temperature as well as from the pressure of the gas.

2.3.5 Gravity

Like on every other object with a non-vanishing mass, gravity acts on the spherical particles, given by

$$F_g = mg = \frac{4\pi}{3}r_d^3 \varrho g. \tag{13}$$

Here, the gravitational acceleration is denoted by g. The density being $\varrho = 1.51$ g/cm^3 for melamine-formaldehyde (MF) particles and $\varrho = 1.85$ g/cm^3 for silicon dioxide (SiO$_2$) particles, respectively [84]. Since gravity is proportional to the volume of the particle ($\propto r_d^3$), it becomes the dominating force for microscopic particles in a typical ground based experiment, while for nano-sized particles it can often be neglected [85, 86]. This is why for microparticles gravity has to be compensated by other forces, such as the electrostatic force [1–3] or the thermophoretic force [87]. Another method is conducting the experiments in a so-called *reduced gravity environment*[3] such as parabola flights [4], sounding rockets [88], or in space stations (MIR [89] and later ISS (international space station) [90, 91]).

---

[3]To be exact, not the gravity is reduced, but the setup is in a *free falling* surrounding.

3 Phase Transition

Different phase transitions are presented in this chapter, with a spotlight on the crystallization of complex plasmas as well as on the physical background of demixing.

3.1 Liquid and Crystalline Phases in Complex Plasmas

In the case of a high coupling parameter (7), the particles will arrange in periodic structures. Thomas and Morfill [92] called this entity with high translational as well as orientational order a plasma crystal. In three dimensions, the structures can be identical to arrangements known from atomic structures in material science, i.e., face-centered cubic (fcc), hexagonal close packed (hcp)[4], or body-centered cubic (bcc) [94, 95]. In two dimensions, the particles arrange in a hexagonal structure.

At a lower coupling parameter, the particles overcome the caging through their distraction and move freely within the plasma. With reference to atomic behavior, this is called the liquid or even the gaseous state.

The exact physical conditions for the transition between liquid and crystalline structures in Yukawa systems are the object of various considerations [51, 96–99]. For a one component plasma (OCP), in which the charged particles interact exclusively via the Coulomb potential, the critical value for crystallization is $\Gamma_c = 172$ [100, 101]. In real physical systems, the value for the critical coupling parameter increases, due to further effects such as gravity or the electric screening of the particles in the plasma. Moreover, the normalized particle separation κ (5) represents an important parameter for the phase state of Yukawa systems [51, 97, 98, 102].

For a gas-liquid transition, the interaction has to be repulsive as well as attractive. The latter can be realized in complex plasmas by shadowing effects of an ion streaming [52].

3.2 Theory of Phase Transition

Phase transitions characterize the behavior of multiparticle systems following the change of an external parameter, such as temperature, pressure, or an external electromagnetic field. Examples for phase transitions include the transformations between the different aggregation states of matter; melting, vaporization, sublimation as well as the reverse processes freezing, condensation, and deposition. The change of a crystal structure, transition to superconductivity (and thus the disappearance of electrical resistance), transition to paramagnetism (around the Curie temperature for ferromagnetic materials and at Néel temperature for antiferromagnetic materials), or transition to superfluidity (and thus the disappearance of viscosity) are also phase transitions. Finally, mixing two distinguishable materials into a single phase system, or the transition into a electrorheological system as well as the reverse processes are also called phase transitions [103, 104].

To understand phase transitions in detail, the term *free energy* $F(T)$, defined as the

---

[4]In pure Yukawa systems, the hcp phase is a metastable state and does not exist if the system is in ground state [93].

amount of work a system can do, as a function of the temperature T, is introduced, defined by

$$F(T) = E - TS. \tag{14}$$

Here, the internal energy and the entropy are denoted by E and S, respectively. By way of classification, Ehrenfest called phase transitions, in which the n.th derivative of the free energy is discontinuous, *phase transitions of n.th order.*

Take, for example, the melting and crystallization at a constant pressure. The free energy function of the liquid phase differs from that of the solid phase. Since in solids the particles are located in an optimized distance and angular distribution to each other, the free energy function of the solid system is below the function for liquid systems at low temperatures. With rising temperature, the free energy is increasingly dominated by entropy, defined by $S = k_B \ln \Omega$ with the number of accessible states Ω. Following (14), the function of free energy decreases faster for liquids than for crystals, since in liquids more accessible states exist. At a high temperature, the free energy of the liquid systems is below the value for the solid state. In order to minimize the free energy, the system in thermodynamic equilibrium is in the solid state at low temperatures and in the liquid state at high temperatures. At the temperature at which both functions became equal, a phase transition (melting or crystallization) takes place. The combined curve of free energy is a continuous function of temperature, but its first derivative in respect to temperature is discontinuous at the melting point. This is why melting and crystallization are first-order phase transitions [103].

To illustrate these correlations, one might think of ice at normal pressure and at a temperature below zero degrees. By adding thermal energy, it is heated up, until zero degrees is reached and melting begins. Although the same amount of thermal energy is added continuously, the temperature remains constant, until all ice is melted. Only after the ice has vanished, does the temperature rise again. This is why the function of the free energy (14) is continuous, but its derivative is discontinuous at melting temperature.

The transformation of a three-dimensional complex plasma from the liquid state to solid state and the rearward process are also first-order phase transitions [93, 104–107]. For the melting of a two-dimensional complex plasma, two competing theories exist, namely, the grain-boundary [108, 109] and the KTHNY[5] theory for melting [111–115]. In the grain-boundary theory, the melting of a system is described by a single first-order phase transition, while in the KTHNY theory the melting happens via a hexatic phase through two second-order (continuous) phase transitions [39, 116].

The conversion of the crystal structure within a three-dimensional complex plasma is a second-order phase transition [104]. Furthermore, Astrakharchik, Belousov, and Lozovik [117, 118] discovered that manipulating the Debye length leads to various first- and second-order phase transitions of a cluster consisting of a few dozen particles.

---

[5]Named after its developers J. M. Kosterlitz, D. J. Thouless, B. Halpering, D. R. Nelson, and A. P. Young in the 1970's [110]

3.3 Liquid - Solid Transition in 3D

There are various distinguishable mechanisms of crystallization, depending on the specific properties of a given material as well as the external conditions. These conditions include particle mobility before and after reaching the surface of the aggregation, particle flux onto the surface as well as the interplay of latent energy, undercooling, the cooling process, and the creation of bonds between particles. Further, a possible intermediate phase between the solid state and liquid state, the structure of the crystallization front, external or internal fields, instabilities, stochastic noise, and anisotropies influence the solidification process. Since the actual crystallization mechanism has a crucial effect on the characteristics of the solid material, detailed time- and space-resolved studies on the different solidification mechanisms are of broad interest. In the following, three different growth mechanisms are presented.

In **epitaxial growth**, a compact crystallization front is created, starting from a seed. In the beginning, the crystal grows *layer-by-layer*, where one layer is completed before the layer above it is begun. No highlighted point exists in the layers [119].

In **diffusion-limited aggregation (DLA)**, the particles stop moving as soon as they touch the aggregate. In contrast to epitaxial growth, the particles here do not rearrange on the surface of the aggregation. Since the exposed ends of the aggregation screen the remaining parts, they have a higher probability of acquiring new particles. The higher growing speed of the exposed ends as opposed to the center of the aggregate leads to branched complex objects. To simulate the diffusion-limited aggregation the following model is applied. First, a single particle is located in the origin of ordinates. Then, a second particle is placed far away from the first, performing a random walk, until they touch. After the second particle hits the first, a third is added far away from the others, executing also a random walk, until it touches one of them. This method is repeated for all particles. Since only one moving particle exists at a single time, it is not affected by others on its way to the aggregate.

In **diffusion-limited cluster-cluster aggregation (DLCA)** simulation, all particles are distributed randomly in the first step. If two particles meet at any time, they irreversible stick together, becoming part of the same cluster. In each time step, a randomly selected isolated particle or cluster of particles is moved in an arbitrarily chosen direction. Since the particles becomes attached to each other when they touch, the amount of isolated particles and clusters decreases with time. The simulation is finished as soon as all particles are arranged in the same cluster.

In DLA as well as in DLCA, self-similar aggregations are generated; in other words, the whole looks the same as its parts so that zooming in or out reveals the same picture[6]. Under certain conditions, two extended clusters can stick together in DLCA, while in DLA, clusters grow one particle at a time. Hence, the aggregates generated by DLCA

---

[6]As with every physical system, this definition is only true within a certain range; e.g., depending on the finite size of the bond of two particles or the total amount of particles.

are commonly higher branched than those grown by DLA. To quantify the structure of an aggregate, the fractal dimension can be applied [120]. Given a three-dimensional embedding euclidean space, aggregates grown by DLCA have a fractal dimension of $d_f = 1.78 \pm 0.06$, and aggregates grown by DLA one of $d_f = 2.53 \pm 0.06$. Assuming that epitaxial growth is dominated by layer-by-layer stacking, the dimension of the formed aggregates then corresponds with the dimension of the embedding euclidean space [119, 121–123].

If the bonds between the particles can be destroyed, leading to their rearrangement, then the growth is reversible. Since the extended ends of a cluster have a high probability of breaking apart, reversibility provides much more compact objects. As a result, the re-arrangement of the fragments increases the fractal dimension of a cluster. Nevertheless, the fractal dimension cannot be higher than the dimension of the embedding euclidean space [124].

3.4 Demixing: From a One-Phase to Two-Phase System

Nowadays, most produced solids and liquids, like alloys, polymers, and solutions, are mixtures of at least two different particle types. Often, two distinct substances are only miscible to a limited extent. If demixing is preferred, two distinct phases are generated within the solution, either by "nucleation and growth" or by "spinodal decomposition" [125]. Taking, for example, a mixture of the two partially miscible fluids A and B. Figure 1 depicts the schematic composition - temperature phase diagram at constant pressure. Above the critical temperature T_c, all ratios of A and B, are unconditionally miscible. At a concentration of $c = 0.5$ (c being defined by the relative amount of particles[7] fluid A consists of), two distinct phases are preferred. Additionally, it has been found that, at non-vanishing temperatures, a very slight quantity of impurity through fluid A in a B-dominated liquid (and vice versa) creates stable mixtures.

The region where the mixture is stable and the region where demixing can take place are separated by the *binodal* or *coexistant* line. This line is defined by the local minimum of the free energy F plotted versus the concentration ($\frac{dF}{dc} = 0$). Below the binodal line, the spinodal line can be found, given by $\frac{d^2F}{dc^2} = 0$. Since in the region between the two lines $\frac{d^2F}{dc^2} > 0$, it is called the metastable regime. Here, phase transition into a A-rich and into a B-rich phase is possible via a *nucleation and growth* mechanism. Droplets of the minority component can be formed from the supersaturated solution via a change in composition. Below a critical size, these fluctuations in concentration are energetically unfavorable and will dissolve. Only droplets above the critical size are able to grow within the solution. The mobility of the droplets enables movement via Brownian motion in the liquid, resulting in their contact. Due to surface tension, touching droplets merge into bigger ones in order to minimize the boundary surface between the two phases.

Below the spinodal line, a region exists in which the mixture of both liquids is unstable, given by $\frac{d^2F}{dc^2} < 0$. In contrast to the metastable region, even infinitesimal variations in

---

[7]Here, "particles" denotes the interacting partners; in real materials this could also be molecules or atoms.
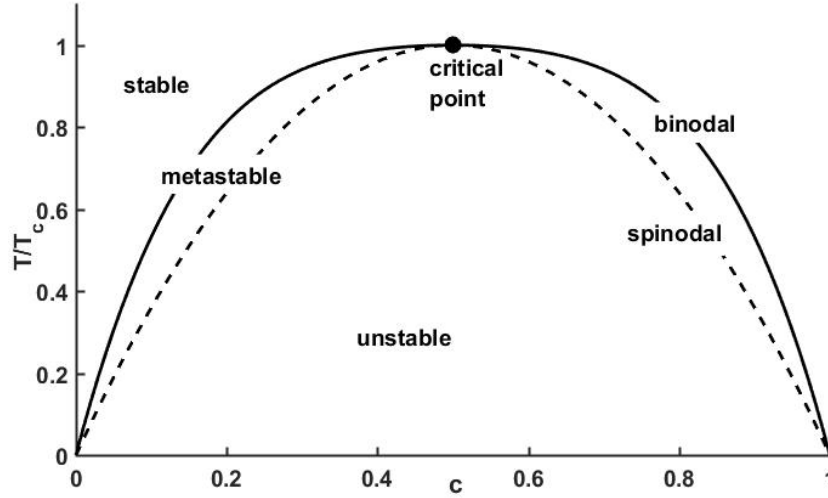
Figure 1: A schematic isobaric phase diagram for the miscibility of two materials; c is the concentration of a component in the binary mixture, T/T_c is the ratio of the temperature and the critical temperature for demixing (according to [103]).

the concentrations will lead to separation, since neither a surface energy nor a nucleation barrier are present. If an initially homogeneous single phase mixture is quenched into this regime, then phase separation occurs by spinodal decomposition. While nucleation and growth mechanism is a discontinuous phase transition (due to the sharp boundaries between the distinct phases), the spinodal decomposition is a continuous transition (due to a gradual increase and decrease of concentration) [39, 103, 126–128].

The function of free energy is continuous during demixing. Entropy and so the derivative of the free energy with respect to temperature are, however, discontinuous at the critical temperature. Due to the fact that spinodal decomposition is characterized by a gradual variation of concentration, this discontinuity is solved. As a result, nucleation and growth mechanism is a first-order phase transition, based on the presence of sharp boundaries between the different phases, while spinodal decomposition is considered as a second-order phase transition [103].

Phase separation of binary mixtures is not only, however, possible if the interaction force between the particles of the same type is attractive, and repellent between distinct particles (such as, e.g., in a mixture of water and oil). Following the Lorentz-Berthelot mixing rules [129], phase separation could also takes place if the interparticle forces between particles of the same type are repulsive, as long as the geometrical mean of there interaction is weaker than the repulsive interaction between particles of different types. In a complex plasma with particles of two different sizes, the larger ones carries a higher negative charge (4). Due to this diverging charge in a steady state, the particles can create two distinct phases [128, 130–132]. In reference [133], the spinodial line for

complex plasmas, depending on the particle size and plasma parameters, is derived. Following these calculations, spinodal decomposition occurs for mixtures of particle types, in which the bigger one is double or triple in diameter compared to the smaller [133]. This is easily realized in experimental setups [134].

Other experiments also show that for even smaller size disparities of about 5%, phase separation can be observed, which might be related to slightly different electric forces acting on the particles [135].

4 Setup and Identification of Particle Positions

In this chapter, the setup is presented, in which the experiments dealing with crystallization are performed [1–3]. Since the demixing experiments were conducted in the well-described PK-4 setup, details about this facility are given in reference [52, 136]. Additionally, the method to acquire the particle positions from a tomographic scan is given.
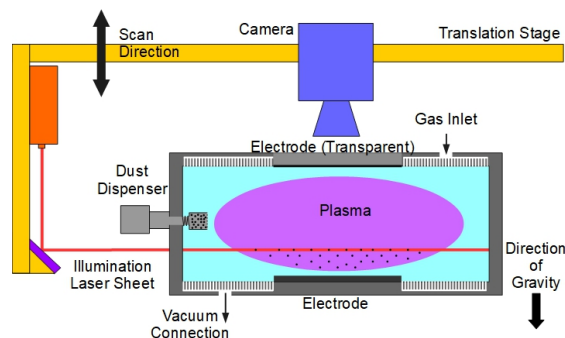

Figure 2: A schematic sketch of the setup, the guard ring for confinement (not shown) is located directly around the upper electrode [2].

4.1 Setup

Experiments dealing with crystallization [1–3] were performed in a cylindrical plasma chamber, originating from the *Max Planck Institute for Extraterrestrial Physics* [137]. The parallel-plate radiofrequency (13.56 MHz) chamber has a height of 3 cm and a diameter of 14 cm. The electrodes with a diameter of 7.5 cm are operated independently. In the experiments, the upper electrode has a peak-to-peak voltage of 35 V, and the lower one of 15 V. A dispenser mounted on the side of the chamber injects melamine-formaldehyde particles with a diameter of 2.05 ± 0.04 μm into the argon discharge. For horizontal confinement of the particles within the plasma, a guard ring is placed around the lower electrode. The intrinsic electric field in the plasma sheath compensates gravity, allowing the particles to levitate. A stream-reduced gas inlet and a separate gas outlet make it possible to refresh the gas or to manipulate the pressure in the discharge without changing the amount of particles.

To observe the particles with a complementary metal-oxide semiconductor (CMOS) camera located above the chamber, the upper electrode is made of glass coated with indium tin oxide (ITO). For particle illumination, a laser beam is expanded to a sheet (thickness about 0.1 mm) parallel to the electrodes. The camera has a resolution of 15.6 μm/px and is mounted on the same stage as the laser. For a tomographic scan of the three-dimensional particle cloud, this stage is moved in or against the direction of gravity, while taking pictures. A filter is installed in front of the camera, which only allows light

with a frequency of the laser to pass. This filter accomplishes reliable discrimination between the reflections of the laser light by the particles and the background light coming from the plasma or from external sources. Technical limitations (a low depth of focus and a limited Rayleigh length of the laser) allow for observation for only one area of the particle cloud at a time. Under gravity conditions, the particle cloud has a finite height, where in the upper regions the particle number depletes [138]. The region of interest, containing ten thousands of particles, had a size of a few hundred cubic millimeters and was located about 3 mm above the middle of the lower electrode within the plasma bulk. Figure 2 shows a sketch of the experimental setup [1–3].

4.2   Tracking of Particles

To gain the particle positions [1–3], a tracking algorithm according to J. C. Crocker and D. G. Grier [139] was applied. Thanks to a filter, which only transmits light with the same wavelength as the laser light, the particles appear as white dots on a dark background in the recorded pictures. If the brightness of the dots was above a certain threshold, it was possible to determine the position of the particles with subpixel accuracy in the single frames. The next step was to track the particles over a certain number of consecutive frames, taking the maximal horizontal movement between two frames into consideration. Only when the same particle was identified in a minimum number of frames, its positional data was saved for further analysis. The number of frames a particle had to be identified in depended on its size, on the diameter of the laser sheet, and on the number of frames recorded per millimeter. The frame rate and the scanning speed define the number of frames per millimeter.

A tomographic scan is only reasonable for static systems [1, 2] or systems changing at a slower rate than the time needed for a scan [3]. In reference [4], a highly dynamic process was considered, allowing only a slice of the three-dimensional system to be recorded. The particle positions in every frame were gained independently from the other frames. To analyze the demixing of big and small particles, they had to be distinguished by their size. This was done by the integrated brightness and the shape the particles appeared as (since the smaller ones moved significantly within the exposure time, they appeared as tracks [134]).

5 Structure Analysis

This chapter considers mathematical methods for detecting and describing the phase transitions. For the crystallization experiments [1–3], the criteria for determining if the particles are in crystalline or in the liquid state are presented. Since lanes are created during demixing, the scaling index method is derived to identify the local dimension in which the particles can be found.

5.1 Crystallization Criteria

Since a tomographic scan of the particle cloud reveals no dynamic behavior, the periodicity of the position data is the only way to identify the state of aggregation. A high periodicity indicates crystalline, a low one liquid structures.

5.1.1 Pair Correlation

Pair correlation is based on a histogram of the distances form each particle to its neighbors. For a system with N particles and a particle density ρ, it is defined by

$$g(r) = \frac{1}{\rho N} \Big\langle \sum_i^N \sum_{j \neq i}^N \delta(\mathbf{r} - \mathbf{r}_{ij}) \Big\rangle. \tag{15}$$

Here, $\mathbf{r}_{ij}$ is the connection vector of the particles i and j; $\mathbf{r}_{ij} = \mathbf{r}_i - \mathbf{r}_j$. In periodic systems such as crystals, the pair correlation has distinct minima and maxima, while in disordered systems the extrema disperse. Following the Raveché-Mountain-Streett criterion, Lennard-Jones systems are crystalline if the ratio of the first minimum divided by the first maximum is $R < 0.2 \pm 0.02$ [140];

$$R = \frac{\min_1(g(r))}{\max_1(g(r))}. \tag{16}$$

In other systems the exact value can slightly differ [141]. A disadvantage of this criterion is that it does not deal well with inhomogeneities, such as a system under stress because of gravity (see [1]).

5.1.2 Nonspherical Distribution

Another, more local, crystallization criterion is *nonspherical distribution* [142]. It is proportional to the relation of the surface A and the volume V of the Voronoi cell of the particle. For a particle i, it is defined by

$$\alpha_i = \frac{R_{c,i} \cdot A_i}{3V_i}. \tag{17}$$

The average curvature radius R_c for polyhedrons is given by

$$R_c = \frac{1}{8\pi} \sum_k^{\text{edges}} l_k \phi_k. \tag{18}$$

Here, l_k is the length of two intersection facets and ϕ_k (in units of radian) is the angle between their normal vectors, pointing outward. In highly ordered crystals, the histogram of α over all particles is peaked at low values, whereas in liquids, the distribution fades toward higher values. For crystal structures occurring in complex plasma (bcc, fcc, and hcp), the peak is at about 1.2 ($\alpha_{\text{bcc}} = 1.18$, $\alpha_{\text{fcc}} = \alpha_{\text{hcp}} = 1.22$); for liquids, the maximum is at approximately 1.31 [1, 2, 142].

5.1.3 Scalar Product of the Local Bond Order Parameter

An often applied local method to determine the state of aggregation is the *scalar product of the local bond order parameter* (SPBOP) [143–147]. For this parameter, a constant number [148], a cutoff-radius [149], or the Voronoi neighbors [150] are used to define the neighborhood. For a constant number of nearest neighbors N (e.g., twelve), the local order parameter can be written as

$$q_{6m}(i) = \frac{1}{N} \sum_{j=1}^{N} Y_{6m}(\mathbf{r}_{ij}) \tag{19}$$

with the spherical harmonics functions Y_{6m} of degree 6 ($l = 6$), since they are the most sensitive. After normalization

$$\tilde{q}_{6m}(i) = \frac{q_{6m}(i)}{\sqrt{\sum_{m=-6}^{6} |q_{6m}(i)|^2}}, \tag{20}$$

the scalar product of the local bond order parameter S_{ij} for the neighbors i and j can be calculated by

$$S_{ij} = \sum_{m=-6}^{6} \tilde{q}_{6m}(i) \cdot \tilde{q}_{6m}^*(j). \tag{21}$$

Complex conjugation is denoted by the asterisk *. If $S_{ij} > 0.75$, the two neighboring particles i and j are defined as being connected. In case of at least eight connected neighbors, a particle is identified to be in the solid state, otherwise as in the liquid state.

5.1.4 Scalar Product of the Minkowski Structure Metric

A disadvantage of the local bond order parameter is that it changes erratically, due to the shifting of the neighborhood [151]. This is why the *scalar product of the Minkowski structure metric* (SPMSM) is developed in [1], based on the ideas of reference [151].

Instead of a constant number of nearest neighbors (or applying a cutoff length, which is unsuitable for inhomogeneous systems), the Voronoi neighbors are used. Since the contribution of each neighbor is weighted by their respective Voronoi facet area $A(f)$, SPMSM is a robust method, independent from the local density.

The bond order parameter $q'_{6m}(\mathbf{r}_i)$ is then given for the particle i by

$$q'_{6m}(i) = \sum_{f \epsilon \mathcal{F}(i)} \frac{A(f)}{A} Y_{6m}(\mathbf{r}_{ij}). \tag{22}$$

Here, the sum runs over all Voronoi neighbors of the particle i. Accordingly, the total surface of the Voronoi cell A is defined by the facet areas $A(f)$; $A = \sum_{f \in \mathcal{F}(i)} A(f)$.

The scalar product of the Minkowski structure metric is defined analogous to SPBOP. For the multiplication (see (21)), the Voronoi neighbors are used. The identical thresholds (for deeming two particles connected and the minimum of connected neighbors to be identified as being in the solid state) are introduced. The local method also allows for visualization of the position of particles in the solid state and in the liquid state within the particle cloud [2, 3]. In reference [94], it was possible to show that the SPMSM is insensitive against small dislocations; e.g., because of particle oscillations.

5.2 Scaling Index Method

During demixing, the smaller particles arrange in lanes to penetrate the cloud of bigger particles. Since other approaches, such as *binary correlation*, *bond orientation functions*, and *Legendre polynoms* are not sensitive enough for lane formation, the *scaling index method* is applied [152]. The scaling index method is a well-established tool to detect the local structural characteristics of a data set. Thus far, it has been applied to analyze complex plasmas [152], bones [153], cosmic microwave background [154, 155], or as an image processing tool [156].

For a set of N points with the positions $\mathbf{r}_1$, $\mathbf{r}_2$, $\ldots \mathbf{r}_N$, the *local weighted cumulative point distribution* is given by

$$\rho(\mathbf{r}_i, R) = \sum_{j=1}^{N} K_R(d(\mathbf{r}_i, \mathbf{r}_j)). \tag{23}$$

Here, i, $j \in (1, 2, \ldots, N)$, and $K_R()$ denotes a kernel function depending on the scale R. The distance between point i and point j is given by $d(\mathbf{r}_i, \mathbf{r}_j)$, for simplification the Euclidean norm is used $d(\mathbf{r}_i, \mathbf{r}_j) := d_{ij} = ||\mathbf{r}_i - \mathbf{r}_j||_2$.

Commonly, it is assumed that for smaller scales the following approximation in dependence of the scaling index α_i is valid

$$\rho(\mathbf{r}_i, R) \propto R^{\alpha(\mathbf{r}_i)}. \tag{24}$$

As a result, α_i is given by

$$\alpha(\mathbf{r}_i, R) = \frac{\partial \log \rho(\mathbf{r}_i, R)}{\partial \log R} = \frac{R}{\rho} \frac{\partial}{\partial R} \rho(\mathbf{r}_i, R). \tag{25}$$

Page 19

Following (25), the Kernel function has to be one time differential (e.g., realized by a Gaussian shaping function), thus (23) can be rewritten as

$$\rho(\mathbf{r}_i, R) = \sum_{j=1}^{N} \exp\left(- \left(\frac{d_{ij}}{R} \right)^q \right). \tag{26}$$

The weighting of the element j according to the distance d_{ij} is governed by q ($q \in \mathbb{N}$). With a low q, even particles with a distance greater than the scale R, significantly influence $\rho(\mathbf{r}_i, R)$. A high exponent q, making the function more steplike, discriminates all particles further away than R. In the limit $q \to \infty$, the function is a Heaviside function. For the here presented work $q = 2$ is chosen, where (26) is the Gaussian exponential function (in appendix A, it is demonstrated that the choice of $q = 2$ can be justified).
Following (25) and (26) with $q = 2$, the anisotropic scaling index is given by

$$\alpha(\mathbf{r}_i, R) = \frac{\sum_{j=1}^{N} 2 \cdot (d_{ij}/R)^2 \exp(-(d_{ij}/R)^2)}{\sum_{j=1}^{N} \exp(-(d_{ij}/R)^2)}. \tag{27}$$

This provides the local dimension of the structure the particle i is located in (not to be confused with the fractal dimension, see chapter 3.3) [157, 158]. In appendix A, it is shown that R should be in the order of $15d_{nn}$ (d_{nn} being the nearest neighbor distance). For this value, the limits for $\alpha(\mathbf{r}_i, R)$ are also derived in appendix A: If $\alpha(\mathbf{r}_i, 15d_{nn}) < 0.8$, but positive, the structure around the particle i is compact or point-like (zero-dimensional). If $0.8 \leq \alpha(\mathbf{r}_i, 15d_{nn}) \geq 1.5$, the particle is in a line-like environment (one-dimensional). Finally, if $\alpha(\mathbf{r}_i, 15d_{nn}) > 1.5$, the structure around the particle is flat (two-dimensional).

5.2.1 Preferred Direction

For describing the demixing process in a complex plasma, the different behaviors of the individual components are essential. While penetrating the cloud of big particles, the small particles create lanes with a preferred direction. For the identification of this direction, the positions of the particles are stretched by the aspect ratio $\epsilon > 1$ in the direction $\mathbf{u} = [\cos\theta, \sin\theta]$, ($\theta \in [-\pi/2, \pi/2]$), before their distances are calculated. The transformed distance between the points i and j is given by

$$d'_{ij}(\epsilon, \theta) = ||\Lambda(\epsilon)\Xi(\theta)\mathbf{r}_i - \Lambda(\epsilon)\Xi(\theta)\mathbf{r}_j||_2. \tag{28}$$

Here, $\Xi(\theta) = \left(\begin{smallmatrix} \cos(\theta) & -\sin(\theta) \\ \sin(\theta) & \cos(\theta) \end{smallmatrix} \right)$ is a rotation matrix and $\Lambda(\epsilon) = \left(\begin{smallmatrix} \epsilon & 0 \\ 0 & 1 \end{smallmatrix} \right)$ a stretching matrix. Following (28), the anisotropic scaling index (27) becomes aspect ratio and angle dependent $\alpha(r_i, R, \epsilon, \theta)$. This then allows determining the angle θ_i, where the scaling index method is the most sensitive; i.e., for this angle, the difference $\alpha(r_i, R, \epsilon, \theta + \pi/2) - \alpha(r_i, R, \epsilon, \theta)$ is maximal. The preferred direction vector for the i.th particle is then given by $\mathbf{u}_i = [\cos\theta_i, \sin\theta_i]$.

In order to get a global value to quantify the degree of laning, a global tensor T is introduced, given by

$$T = \frac{2}{N} \sum_{i=1}^{N} \mathbf{u_i} \otimes \mathbf{u_i} - \mathbb{I}. \tag{29}$$

The identity matrix is symbolized by $\mathbb{I}$, and $\otimes$ is the Kronecker product. Commonly, the tensor T has two distinct eigenvalues; the larger one is called laning-order parameter S. In case of perfectly aligned particles $S = 1$, while in case of a totally random distribution $S = 0$, the lower eigenvalue of T can be negative. The global laning angle Θ is obtained by

$$\cos(\Theta) = \langle \mathbf{u} \rangle \mathbf{e}_x. \tag{30}$$

Here, the unit vector in x-direction is given by $\mathbf{e}_x = [1, 0]$. The eigenvector of the tensor T, denoted by $\langle \mathbf{u} \rangle$, belongs to the eigenvalue S. If $\Theta = 0$, the particles are arranged in a lane; if $\Theta = \pi/2$, the particles are distributed isotropicly [134, 159, 160].

6 The Variation of Neutral Gas Pressure

In this chapter, the publication [1] and its logical further development [2] are summarized. Here, the influence of neutral gas pressure on the crystallization of a three-dimensional complex under gravity conditions was considered.

6.1 Motivation

In experiments, the neutral gas pressure is an easily accessible, crucial parameter for controlling complex plasmas, since pressure manipulation has various effects on particle behavior. Owing to the fact that gas pressure is, via the gas density, proportional to the neutral drag (10), a variation in pressure can have a significant effect on the kinetic energy of the particles. Furthermore, if the pressure drops below a critical value, under certain conditions an instability occurs (see chapter 6.2). The neutral gas drag can also influence the particle confinement and, as a result, the interparticle distance (see chapter 6.3). In a broad plasma parameter range, the pressure is proportional to ion density, which is important for the Debye length (6). In addition, the probability for collisions between ions and neutrals is higher at increased pressure, decreasing the particle charge. The decreased Debye length and the decreased particle charge significantly change the coupling parameter (see chapter 6.4).

6.2 Prior Experiments under Gravity Conditions

In ground based experiments, it is necessary to counter gravity, e.g., via an electric field. Since shielding of constant electromagnetic fields is a fundamental property of a plasma, the strength of such a field is small in the bulk. Hence, levitation of microparticles is commonly realized in the plasma sheath above the lower electrode, where the electric fields are stronger. As a result, the generated particle clouds mainly extended only in two dimensions, perpendicular to the direction of gravity. In contrast to microgravity conditions, the height of the particle distribution is very limited in most conventional experiments under gravity conditions.

Experiments dealing with the transition between the solid and the liquid phase of flat complex plasmas under gravity conditions are summarized in table 1. The exact pressure regime at which melting and crystallization take place depends on the specific characteristics of the experiment, such as the plasma parameters, i.e., gas type [161], ionization degree (controlled by the rf power) [162], particle size [162], the amount of particles [162] as well as their arrangement [162–164]. In the experiments in table 1, the complex plasmas were crystalline at high pressure and melted through the decreasing of neutral gas pressure. Below a certain pressure limit, the kinetic energy of the particles increased by a factor of $10 - 200$. While kinetic energy increased, the particle oscillations got stronger, which was partly made responsible for melting [92, 162, 163, 165]. In the transition between the crystalline state and liquid state, an intermediate phase was observed. Originally, these observations were considered as an indication for the KTHNY [111–115] or grain-boundary [108, 109] theory of melting of two-dimensional systems [92, 165].

Table 1: Examples of solid-fluid phase transitions in complex plasmas under gravity conditions. Since no sharp transitions were observed, the mentioned pressure regimes are partly rough estimations. All experiments were performed with melamine-formaldehyde particles.

gas	rf power [W]	Particle diameter [μm]	Range of melting [Pa]	Arrangement	Reference
He	12	≈ 9.4	$39 - 76$	two layers	[165]
Kr	$0.8 - 2$	9.6	$23 - 42$	few layers	[92]
Ar	2	9.55	$8 - 12$	one layer (N=36) + one particle below	[163]
Ar	3	9.55	$4 - 12$	one layer (N=55) + one particle below	[162]
Ar	5	9.55	$6 - 18$	one layer (N=55) + one particle below	[162]

In the mentioned experiments, the microscopic particles arranged themselves in a few layers located in the plasma sheath region above the lower plasma wall due to gravity. Ions that streamed through the plasma sheath toward the wall were deflected by the particles. These deflections caused by an orientated ion flow were able to generate a positive space charge region, the so-called *ion-focus*. Decreasing pressure increased the mean free path of the ions between the collisions with neutrals, and the positive charge regions were more pronounced [166]. The negative charged particles of the lower layers were attracted by these positive charge regions, which were caused by deflected supersonic ions. As a result, the lower particles aligned below the upper particles, the so-called *wake effect* evolves. This chain-like arrangement was observed in the performed experiments [92, 162, 163, 165]. For the particles in the lower layers, a comparable force acting on the upper layer did not exist, so the system is non-Hamiltonian. The asymmetry of the interaction between the particles of different layers became the reason for unstable behavior. If the gas pressure was below a certain value, the neutral drag could not fade away enough kinetic energy from the particles [167, 168]. In reference [105], the vertical alignment of particles and the sudden increase of their kinetic energy below a critical pressure was called a "two stream instability". This is also the reason why a particle below the main particle layer was crucial for the creation of the instability and thus for the phase transition into the disordered state [163]. In conclusion, in the presented experiments under gravity conditions, melting was the result of a self-excited wave below a critical pressure value, originating in the sheath.

Besides complex plasmas with only few particle layers above the lower electrode, Yukawa balls should be mentioned. Typically, a dozen up to a few hundred particles are injected into a low pressure discharge under gravity conditions. The horizontal confinement is re-

alized, for example, by a square tube with a couple of centimeters in diameter placed on the lower electrode. To compensate gravity, the particles are levitated by thermophoretic force, due to a heated lower electrode (see chapter 2.3.4). In highly ordered phases, the Yukawa balls generate spherical shells with well-defined angular distribution between the particles. Provided that the particle's numbers meet the requirement to fill up the shells, the Voronoi cells of the particles are mainly hexagons[8], indicating a highly order curved surface [169–175].

Decreasing the pressure increased the ion focus below the particles, due to less frequent collisions between ions and neutrals. Analogous to flat complex plasmas, the lower particles arranged themselves below the upper ones, creating particle chains at decreased pressure. The vertical alignment of the particles led to vertical elongated Yukawa clusters, which destroyed the highly spherical order [176, 177].

6.3   Former Experiments under Reduced Gravity Conditions

Under microgravity conditions, e.g., on board the ISS, the particles are located in the bulk. In reference [90], melting and crystallization of a complex plasma under neutral gas pressure manipulation were considered. After reducing the pressure from ≈ 15 Pa to ≈ 11 Pa, it was again increased, to ≈ 21 Pa. Two separate experimental runs were performed in an argon plasma with different particle sizes and materials. In the beginning, at high pressure (≈ 15 Pa), the particles were in the liquid state; in the middle, at the lowest pressure (≈ 11 Pa), they were mainly in the solid state; finally, at high pressure (≈ 20 Pa), they were in the liquid state again. While decreasing the pressure, the mean interparticle distances decreased and vice versa. Particle charge as well as screening length remained constant during pressure manipulation. The influence of the gas pressure on the kinetic temperature of the particles was not reported, but it is expected that their temperature was in the range of the gas (room) temperature. In conclusion, the increased interparticle distances, as a result of the changed confinement because of the raised pressure, were made responsible for the observed melting. Analogous to this, the decrease of particle separation likewise caused by varied confinement, induced by lowering the neutral gas pressure, was claimed to be the reason for crystallization. Therefore, the solid state at low pressure and the liquid state at high pressure of a complex plasma were effects of the different interparticle separation, but not primarily of neutral gas pressure [90, 178].

6.4   Own Experiment

In [1, 2], the crystallization of a complex plasma in dependence of pressure under gravity conditions was considered. The examined pressure regime was between 25 Pa and 45 Pa. A guard ring around the lower electrode accomplished strong confinement, which allows the cloud of small melamine-formaldehyde particles ($2r_d = 2.05 \ \mu$m) to range up into the bulk plasma and to create many layers even under gravity conditions. The rf generator

---

[8]Following the *Euler's polyhedron formula*, other polygons, with fewer edges, are needed to create a closed surface, e.g., twelve pentagons.

provided an electric power of about 13.7 W. The actual inserted power was lower, due to the reflected power and losses, e.g., in the wires or in the matching network. In complex plasma setups, it is expected that, in sum, more than 90 % of the rf power is not fed into the plasma [179]. This marginally supplied rf power ($\sim$ 1.4 W) generated a dilute plasma, sufficient for a weak electric field to levitate the particles. The distribution of the particles (in up to thirty layers) and their number (ten thousands in total and $\approx 1.5 \cdot 10^4$ in the examined region) are in contrast to experiments dealing with spherical Yukawa balls (max. a few hundred particles) or flat complex plasmas under gravity conditions. In former experiments under gravity conditions [92, 162, 163, 165], the particles arranged periodically before neutral gas pressure was slowly decreased and the order was destroyed by an instability. In this scenario, the properties of a complex plasma were not only a function of the present conditions, but also of the prior pressure, due to a possible hysteresis [90]. On the other hand, crystallization started from the disordered state for each considered pressure value in [1, 2]. The total amount of particles as well as the interparticle distances did not change during the pressure manipulation.

Independent crystallization criteria (chapter 5.1) showed that the particles were in the solid state at low pressures and in liquid state at high pressures. This inverse behavior, compared to former ground experiments with flat complex plasmas, could be explained by decreased particle charge at high pressures. The condition for the OML theory (chapter 2.1), requiring that ions perform collision-free motions in the vicinity of particles, was no longer fulfilled at increased pressure. If an ion collides with a neutral gas atom, the ion can lose its momentum and angular momentum. Further, charge exchange collisions and electron impact ionizations generate slow ions [180]. Low energetic ions next to a particle have a higher probability of reaching the attractive surface of the negatively charged grain. While the flux of positive ions onto the microparticles is increased, their negative charges reduce (see also [165]).
Moreover, since the ion density was increased by increasing gas pressure [181, 182], the Debye screening length also changed under pressure manipulation (following (6) $\lambda_D \propto n_i^{-1/2} \propto p^{-1/2}$). The electron temperature was expected to be constant [183]. The reduced particle charge as well as the decreased Debye length were made responsible for a low coupling parameter (7) at high pressures (at constant interparticle distance). Low ordering at high pressure was then caused by the decreased coupling parameter. Additionally, due to gravity, the upper particles compressed the lower layers, causing reduced interparticle distances in the lower part of the cloud [3, 138, 184]. This could be the reason why the particles in the bottom of the examined region have a higher probability to be in the solid state than those in the upper part [1–3, 138].
A primary stage for the instability, which is made responsible for melting of flat complex plasmas, was the vertical alignment of the particles in the plasma sheath. Thanks to a low rf power, no sign was found for such an alignment in the examined pressure regime. Behavior opposite to that in former experiments under gravity conditions can be explained by two factors: Firstly, the location of the particles up in the bulk plasma, and secondly, a weak electric field for levitation.

7 Process of Crystallization

In reference [3], a crystallization process of a complex plasma was resolved temporally and spatially in three-dimensions. To draw conclusion on the dominant solidification process, the fractal dimensions of the solid clusters were calculated.

7.1 Motivation

The solidification processes of real materials are in a length scale of milli-ångström and in a timescale of picoseconds. Nowadays, some methods such as X-ray diffraction [185, 186] and ultrafast optical spectroscopy [185] allow for monitoring of some details in the crystallization process. Nevertheless, computer simulations [187] or model systems, like colloidal systems and complex plasmas [39], can give much easier access to the involved physics, space and time resolved.

7.2 Prior Experiments

Most publications about the transition between the solid state and liquid state of a complex plasma deal with the melting of a highly crystalline system triggered by variation of one or more parameters, such as pressure (see chapter 6) [107, 165, 188, 189]. The reverse transition from a low into a highly ordered system has been described more rarely. In reference [190], a two-dimensional complex plasma crystal was melted by a short electric pulse, and the recrystallization was observed. The solidification happened via the creation of highly ordered local domains and the decreasing of lattice defects. During recrystallization, the particles lost their kinetic energy until the original level was reached.
A crystallization front of a two-dimensional slice of a three-dimensional complex plasma was considered in reference [191]. The fractal dimension of the crystallization front was calculated to draw conclusions on the solidification mechanism. In the slice, the determined fractal dimension of the front line oscillated between 1.16 and 1.21. This value is between the expected fractal dimension values for epitaxial growth (here, $d = 1$) and for diffusion-limited aggregation (here, $d_f \approx 1.42$). Following reference [123], the complete front area had a fractal dimension of $d_f = 2.16 - 2.21$ in the three-dimensional embedding euclidean space.

Previous work demonstrated that colloid systems can solidify via various mechanisms, including epitaxial growth [192], diffusion-limited growth [193, 194], dendritic growth [195], and reaction-limited growth [196, 197]. In colloid systems some growth instabilities [194, 198] could be observed, as well [199].

7.3 Own Experiment

The crystallization process of an extended three-dimensional complex plasma was described in [3], time and space resolved. In contrast to prior experiments [190, 191] a

three-dimensional region was examined.

The plasma parameters and the particle charge were in steady state microseconds and milliseconds, respectively. Therefore, these values were expected to be constant during the experimental run. In a first step, solid clusters were identified at different times after the start of crystallization. Following percolation theory, the fractal dimension can be determined as soon as a cluster first breached the gap between opposite ends of the examined area. Significantly later, the fractal dimension of the cluster increases toward the dimension of the embedding euclidean space [123].

The fractal dimension d_f can be calculated via the box-counting method [123, 200], given by

$$d_f \propto \lim_{L \to 0} \frac{\log(N(L))}{\log(1/L)}.$$ (31)

Here, the minimum number of boxes with length L to cover the fractal object is $N(L)$. The fractal dimension is then given by the slope of the double logarithmic plot of $N(L)$ versus L.

The thus-determined fractal dimension of $d_f = 2.72 \pm 0.03$ was above the value for diffusion-limited growth ($d_f \approx 2.5$) and below the value for epitaxial growth ($d = 3$). These values allow the assumption that the crystallization process was governed by both processes. The diffusion-limited cluster-cluster aggregation ($d_f \approx 1.8$) could not be the main solidification mechanism, because of its low fractal dimension. Note that due to destruction of the bonds and rearrangement of the particles, the fractal dimension could also be increased. The value for the fractal dimension of the solid clusters is in accordance with former results based on two-dimensional data [191].

8 Demixing

This chapter is based on the forth publication, in which different physical processes of a complex plasma in a parabola flight were studied [4]. In this context, only the results of the demixing experiments are described.

8.1 Previous Demixing Experiments under reduced Gravity Conditions

The ubiquitous phenomenon of phase separation of two liquids is an often examined issue (see e.g., [201, 202] and references therein). The demixing of multi particle systems with Yukawa interaction has been studied extensively in different systems, ranging from complex plasmas [128], to Yukawa suspensions [203] as well as to molecular and Langevin dynamics simulations [204, 205].

In complex plasmas, phase separations of particles with disparate sizes are based on their differing magnitude of electric charge, due to a radius-dependent charging (4). Using identical material, particles of different size do not have the same mass. Under gravity conditions, the particles would be levitated by an electric field in different heights depending on their mass-to-charge ratio over the lower electrode, within the plasma sheath. As a result, under gravity conditions, the separation of particles with different sizes is not an effect of their interaction forces, but of levitation. This is why experiments dealing with phase separation in complex plasmas are done under reduced gravity conditions, like on board the ISS [128, 132]. Since demixing takes place within seconds, experiments on parabola flights are also possible [130].

On board the ISS, in PK-3 Plus [182], big particles ($2r_d = 9.2$ μm) were injected into an argon discharge at 30 Pa. The particles created a spheroidal, homogeneous cloud with a central void before smaller particles ($2r_d = 3.4$ μm) were added. A small electric field pulled these small particles toward the center of the chamber. By penetrating through the cloud of big particles, the small ones arranged themselves into lanes, while the big particles were pushed away, likewise forced to arrange in lanes. Since the lanes of small particles followed the field lines toward the center, they got closer to each other and merged into bigger lanes. As the net force grew weaker in the vicinity of the center, the small particles created a compact drop. The drop consisted only of the small particles, whereas the lager ones were squeezed out. After reaching the void, the drop dissolved viscously, and the small particles arranged around the void. A few seconds later, the big particles were distributed homogeneously again. In figure 3, small particles penetrating a cloud of big ones via lane formation are shown [128, 132, 134, 206].
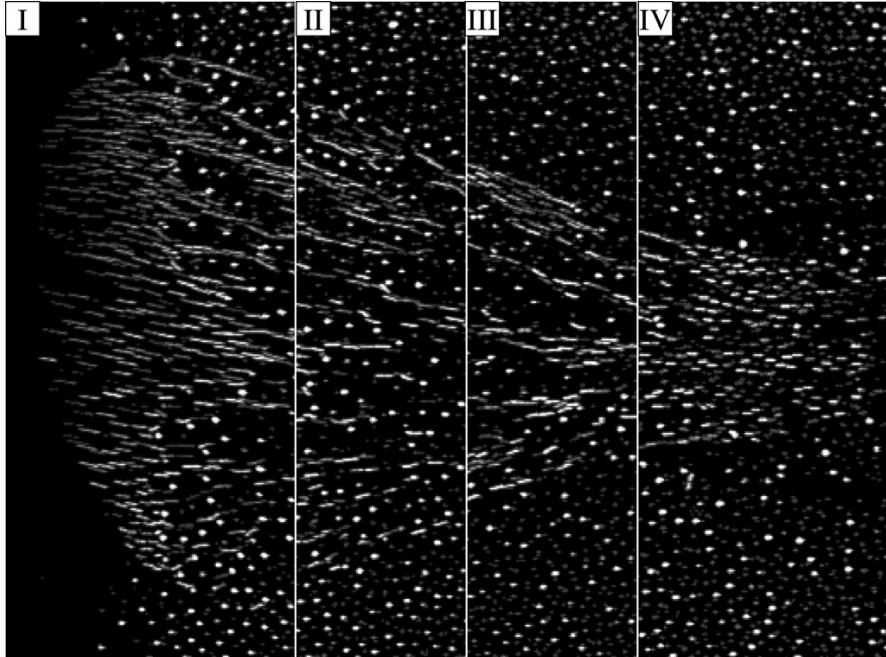
Figure 3: Small particles (coming from left) penetrate a cloud of big particles, due to an electric field pointing toward the center of the chamber (at the right side). Since the small particles move significantly during exposure time (0.04 s), they appear as streaks. The numbers show the evolution of the process at different times; I. ($t = 0$ s) small particles reach the big ones, II. ($t = 0.4$ s) small and then big particles are arranged in lanes, III. ($t = 1$ s) the lines of the small particles are merged into bigger ones, IV. ($t = 2$ s) the small particles create a drop [128].

8.2 Own Demixing Experiment under Milligravity Conditions

The experiments reported in reference [4] were performed in a parabola flight within the PK-4 setup. Here, two distinct particle types were mixed in the dispenser prior to their injection into the discharge[9]. Commonly, in phase separation experiments, particles with one size created a cloud, before particles with a different size coming from another dispenser were added and penetrated that cloud (see chapter 8.1) [128, 132, 134, 135, 160, 182]. Experiments in which one dispenser is filled with particles of different types were much more rare [130]. In reference [4], the phase separation of a mixture consisting of melamine-formaldehyde ($2r_d = 3.27$ μm) and silicon dioxide ($2r_d = 2.06$ μm) was observed. The dc discharge current was 1 mA, and the argon pressure was 100 Pa.
The anisotropic lane formation (see chapter 5.2) showed that the small particles arranged behind one another, creating lanes. The bigger ones remained mainly homogeneously

[9]On ISS, the dispensers are filled with monodisperse particles and cannot be changed by astronauts or cosmonauts.
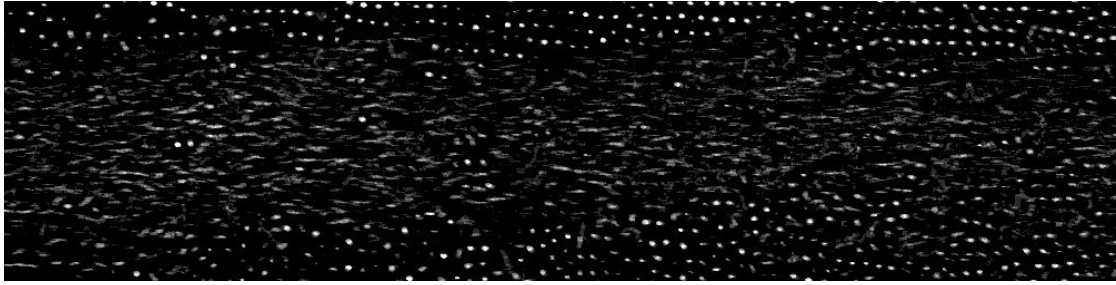
Figure 4: During demixing, small particles (SiO_2 $2r_d = 2.06$ μm) move from the left side toward the right side. The big particles (MF $2r_d = 3.27$ μm) remain in their positions. An electric field could not be excluded, which influenced the motion of the small particle analogous to [128]. For this picture, six single frames (exposure time ≈ 0.01 s) were superimposed.

distributed, without a preferred direction during the demixing process. In figure 4, the small particles moving through the cloud of unmovable big particles are shown. It could be seen that, similarly to former experiments, some big particles were surrounded by the small moving particles.

9 Conclusion and Outlook

In the presented work, it was verified that complex plasmas are ideal model systems for observing and studying dynamical processes like phase transitions on a single-particle level.

The neutral gas pressure turned out to play an ambivalent role for the crystallization of a three-dimensional complex plasma: From former work, it is known that high pressures reduce the kinetic energy of the particles and suppress instabilities or increase the particle separation via a variation of their confinement. In references [1, 2], it was shown that high pressure is also responsible for lower particle charges and a decreased Debye length, leading to the opposite effect, namely, a crystallization at low pressure.

Furthermore, the solidification process of a complex plasma was identified with the help of the fractal dimension of solid clusters, giving new insights into the crystallization process in three-dimensions. For analysis, the scalar product of the Minkowski structure metric was developed, inspired by Mickel *et al.* [151]. This crystallization criterion also became a crucial parameter in a *machine learning* algorithm [94].

The transition from a single phase mixture into a two phase system was observed in a complex plasma with two different particle types under milligravity conditions. The behavior of the different particle types in the phase transition could successfully be described by the scaling index method.

Nevertheless, some issues should be investigated in future work:

- The influence of neutral gas pressure for a complex plasma, in particular for the particles' state of aggregation, should be determined more accurately. Here, the kinetic energy of the particles, their charge, and the interparticle distance as well as the Debye length are crucial parameters. For further studies, a detailed analysis of the actual plasma parameters is essential.

- In this work, the fractal dimension of the solid clusters created during crystallization was used to draw conclusion about the solidification mechanism. It would be interesting to clarify if the exact solidification mechanism depends on external (or internal) conditions, or whether it is an intrinsic property of complex plasmas. Besides, the particle flux toward a solid cluster and the mobility of particles touching its surface are important factors for understanding the solidification mechanism. Further, the role of reversibility should be considered via a higher temporal resolution of the particle positions.

- In subsequent experiments, the difference between the two demixing processes, i.e., spinodal decomposition and nucleation and growth within a complex plasma would be of special interest. Moreover, a direct measurement of the free energy of the particles in the different phases would help to determine the order of phase transition experimentally. A detailed analysis of the evolution of the free energy during solidification could also provide a deeper understanding of the involved physics.

- In the demixing experiments of reference [4], a weak electric field acting on the particles could not be excluded. Since the smaller particles carry a lower charge than the bigger ones, they experience a different electric force. If the electric field is too strong, the demixing is a reaction of the external force acting on the particles, rather than of the intrinsic properties of the particles themselves. This is why in future work, it should be guaranteed that no external forces depending on the particle properties occurs.

- In the publication [4], while demixing of different liquids, particle pressure was not considered, since its influence was expected to be low [103]. Nevertheless, particle pressure can be a new parameter for manipulating the system in continuing experiments.

A Determination of the Anisotropic Scaling Index Constants
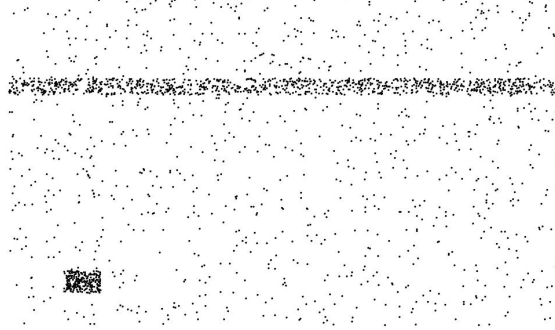
Figure 5: Artificially generated distribution consisting of a background with 1000 homogeneously distributed elements, 1000 elements distributed in a strip, and 250 elements in a square (according to [206]).

To determine the factor R for the anisotropic scaling index (ASI) α (see chapter 5.2), an artificial distribution of elements is generated, as demonstrated in figure 5. The distribution is given by a point-like as well as line-like accumulations added to a homogeneous background. The background should be identified by the anisotropic scaling index as being two-dimensional, the stripe as being one-dimensional, and the small square as being zero-dimensional. If the scale R is too small, the finite width of the stripe and also of the square is sufficient for all structures to be identified as being two-dimensional. If R is too large, even the background is identified as zero-dimensional.

In figure 6, each plot depicts a histogram in a log scale of the calculated α (27) for the distribution given in figure 5. The different plots demonstrate the variation of R shifted upward for better visibility. For a low R, every particle has a different value for α, but no accumulation values are shown. Three distinguishable regions in the distribution are necessary to define limits for assigning the values of the ASI with the local dimensions. At very high scales, each particle has a low value for α, but the different structures of the distribution are also not represented. Only at moderate scales (about 15 nearest neighbor distances d_{nn}), three distinct peaks could be identified in the plot. The left maximum represents the zero-dimensional, the middle one the one-dimensional structure, and the right one the two-dimensional structures. Vertical lines distinguish the three regions. If the anisotropic scaling index is below 0.8 for a specific particle, then its local environment is identified as being point-like; if it is above 1.5, it is identified as localized in a two-dimensional surrounding - or in a line-like surrounding, if not.

The results of the anisotropic scaling index with $R = 15d_{nn}$ are shown in figure 7. The stripe with high element density is identified as a one-dimensional structure, the square as a zero-dimensional structure, and the background as two-dimensional. In the transi-
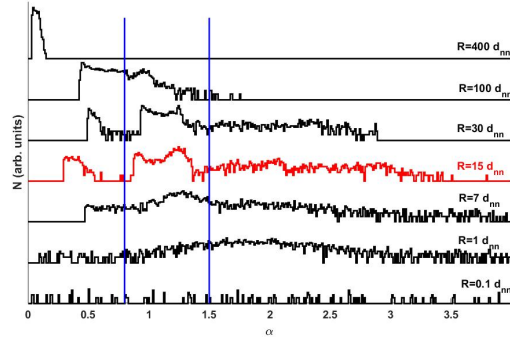
Figure 6: Histograms of the anisotropic scaling index α (27), as a function of the scaling R, for the distribution given in figure 5. In order to be scale invariant, R is defined as a function of the nearest neighbor distance d_{nn}. The applied value $R = 15d_{nn}$ is highlighted. The vertical lines at 0.8 and 1.5 divide the histogram in three regions; particles on the left are defined as being located in a zero-dimensional, those in the middle as in a one-dimensional, and those on the right as in a two-dimensional surrounding (according to [206]).

tion region between the point-like accumulation and the homogeneous background, some particles are wrongly identified as belonging to a one-dimensional structure.

In the derivation of the anisotropic scaling index (chapter 5.2) an exponent q is introduced. It defines the influence of particles on the local dimension, located further away than the scale R. Elements with a higher distance to the considered position than R are ignored for $q \to \infty$. If $q = 0$, all particles would have the same influence on the local dimension. Figure 8 shows the log scale histograms of the anisotropic scaling index (analogous to figure 6) for the distribution given in figure 5 with $R = 15d_{nn}$. For the applied exponent $q = 2$, the histogram shows three distinguishable regions, which is essential for the correlation with the local dimension [206].
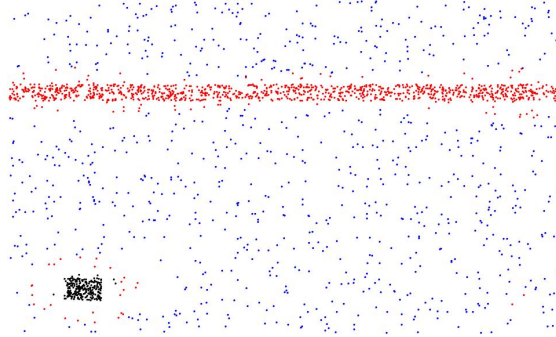
Figure 7: The elements given in figure 5, colored according to the local dimension they are located in with $R = 15d_{nn}$. Elements in a point-like surrounding are black, those in a line-like surrounding red, and those in a two-dimensional surrounding are blue (according to [206]).
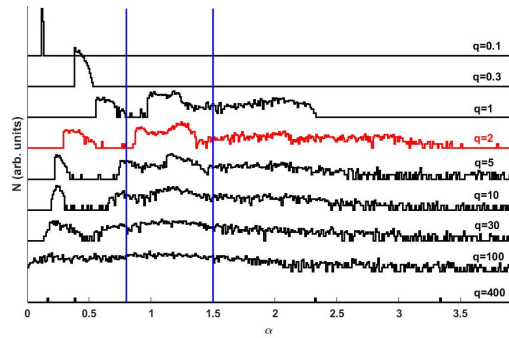

Figure 8: The influence of the exponent q on the anisotropic scaling index ((26) and (27)) with $R = 15d_{nn}$. For better visibility the log scale histograms are shifted. The distribution is shown in figure 5; further explanation is given in figure 6.

Abbreviations and Symbols

A	5.1	Voronoi surface
$A(f)$	5.1.4	Voronoi facet area
ASI	5.2	ansiotropic scaling index
α_i	5.1.2	nonspherical distribution for particle i
$\alpha(\mathbf{r}_i, R)$	5.2	scaling index
$\mathbf{B}$	2.3.1	magnetic field
bcc		body-centered cubic
CMOS	4.1	complementary metal-oxide semiconductor
c	3.4	concentration
DLA	3.3	diffusion-limited aggregation
DLCA	3.3	diffusion-limited cluster-cluster aggregation
d_{ij}		distance between the point i and j
d_f	7.3	fractal dimension
Δ	2.2	mean distance between the particles
δ	2.3.3	dimensionless parameter for gas drag
$\mathbf{E}$	2.3.1	electric field
E	3.2	internal energy
e		elementary charge
$\mathbf{e}_x$	5.2.1	unit vector in x-direction
ϵ	5.2.1	aspect ratio for stretching
ϵ_0	2.1	vacuum permittivity
$\mathbf{F}_{\text{drag}}$	2.3.3	neutral gas drag
$\mathbf{F}_{\text{coll}}$	2.3.2	ion drag force via direct collisions
$\mathbf{F}_{\text{coul}}$	2.3.2	ion drag force via Coulomb interaction
F_g	2.3.5	gravity
$\mathbf{F}_{\text{i}}$	2.3.2	sum of ion drag forces
$\mathbf{F}_{\text{L}}$	2.3.1	Lorentz force
$\mathbf{F}_{\text{th}}$	2.3.3	neutral gas drag
$F(T)$	3.2	function of free energy
fcc		face-centered cubic
ϕ_k	5.1.2	angle between the normal vectors of two intersection facets
ϕ_S	2.1	surface potential
g	2.3.5	gravitational acceleration
$g(r)$	5.1.1	pair correlation function
Γ	2.2	coupling parameter

Page 39

Danksagung

Am Ende dieser Arbeit möchte ich allen danken, dich mich in den letzten Jahren bei meiner wissenschaftlichen Tätigkeit unterstützt haben.

Zuerst möchte ich meinen Betreuer Prof. Dr. Markus H. Thoma für sein persönliches Engagement und die Möglichkeiten, die er mir bot, vor allem jedoch für seine stets freundschaftliche Art danken. Mein Dank gilt auch Dr. Michael Kretschmer für die langen Gespräche und für seinen Rat, seine Tür war nicht nur im wörtlichen Sinne stets offen. Bei Christopher Dietz möchte ich mich für die fruchtbaren Diskussionen bedanken. Ebenso geht mein Dank an alle weiteren Mitglieder und Gäste der Arbeitsgruppe "Plasmaphysik" für das angenehme Arbeitsklima sowie die zahllosen anregenden Gespräche.
Auch wenn unsere gemeinsame Arbeit hier keinen Niederschlag gefunden hat, so möchte ich mich bei Prof. Dr. Slobodan Mitìc für eine gute wissenschaftliche Zusammenarbeit bedanken.

Ohne technische Unterstützung wäre diese Arbeit für mich nicht vorstellbar gewesen. Aus diesem Grund möchte ich mich besonders bei Thomas Nimmerfroh, Christian Schinz und Leon Kleinschmidt bedanken, unsere gemeinsame Parabelflugkampagne bleibt unvergessen.

Mein Dank geht im besonderen Maße auch an Julian Kaupe für seine Hilfe bei der kritischen Bewertung der Ergebnisse, die gewinnbringenden Diskussionen zwischen Mensa und Büro haben mir sehr geholfen. Für unsere kurzweiligen gemeinsamen Mittagspausen gilt mein Dank auch Philipp Riedl.

Für das Korrekturlesen dieser Arbeit geht mein Dank auch an Dorothea Seibert und Monika Lemke.

Für willkommene Ablenkung nach und von der Arbeit möchte ich mich bei Jonas, Monique, Susanna und Mathilde bedanken.

Mein größter Dank geht an meine Familie, für die mir entgegengebrachte Unterstützung. Meinen Brüdern sowie meinen Neffen und Nichten gilt ebenfalls mein Dank, ohne euch wären meine Wochenenden eintöniger. Zuletzt möchte ich mich bei Kayou für sein Verständnis und seine Geduld bedanken.

References

[1] B. Steinmüller, C. Dietz, M. Kretschmer, and M. H. Thoma. Crystallization of a three-dimensional complex plasma under laboratory conditions. *Physics of Plasmas*, 24(3):033705, 2017.

[2] B. Steinmüller, C. Dietz, M. Kretschmer, and M. H. Thoma. Crystallization of a complex plasma under gravity conditions in dependence of pressure. *IEEE Transactions on Plasma Science*, 46(4):694–697, 2017.

[3] B. Steinmüller, C. Dietz, M. Kretschmer, and M. H. Thoma. Crystallization process of a three-dimensional complex plasma. *Physical Review E*, 97:053202, 2018.

[4] C. Dietz, M. Kretschmer, B. Steinmüller, and M. H. Thoma. Recent microgravity experiments with complex direct current plasmas. *Contributions to Plasma Physics*, 58(1):21–29, 2017.

[5] V. I. Molotkov, A. P. Nefedov, M. Y. Pustyl'Nik, V. M. Torchinsky, V. E. Fortov, A. G. Khrapak, and K. Yoshino. Liquid plasma crystal: Coulomb crystallization of cylindrical macroscopic grains in a gas-discharge plasma. *Journal of Experimental and Theoretical Physics Letters*, 71(3):102–105, 2000.

[6] B. M. Annaratone, A. G. Khrapak, A. V. Ivlev, G. Söllner, P. Bryant, R. Sütterlin, U. Konopka, K. Yoshino, M. Zuzic, H. M. Thomas, et al. Levitation of cylindrical particles in the sheath of an rf plasma. *Physical Review E*, 63(3):036406, 2001.

[7] H. Kobayashi, K. Maeda, and M. Izawa. Behavior of particles reflected by turbo molecular pump in plasma etching apparatus. *IEEE Transactions on Semiconductor Manufacturing*, 22(4):462–467, 2009.

[8] H. S. Jun. Diffusive plasma dechucking method for wafers to reduce falling dust particles. *Japanese Journal of Applied Physics*, 52(6R):066203, 2013.

[9] M. Ishiguro, K. Ikenaga, T. Tamura, S. Shirayone, M. Nawata, and M. Sumiya. Particle transport in etching chamber influenced by coulomb force. *IEEE Transactions on Semiconductor Manufacturing*, 28(3):247–252, 2015.

[10] J. Winter. Dust in fusion devices-experimental evidence, possible sources and consequences. *Plasma physics and controlled fusion*, 40(6):1201, 1998.

[11] R. Neu. *Tungsten as a plasma facing material in fusion devices*. habilitation, Universität Tübingen, 2003.

[12] J. P. Sharpe, D. A. Petti, and H. W. Bartels. A review of dust in fusion devices: Implications for safety and operational performance. *Fusion Engineering and Design*, 63:153–163, 2002.

[13] J. Winter and G. Gebauer. Dust in magnetic confinement fusion devices and its impact on plasma operation. *Journal of nuclear materials*, 266:228–233, 1999.

[14] F. Vivet, A. Bouchoule, and L. Boufendi. Synthesis and characterization of sic: H ultrafine powder generated in an argon–silane–methane low-pressure radio-frequency discharge. *Journal of applied physics*, 83(12):7474–7481, 1998.

[15] T. Nagai, Z. Feng, A. Kono, and F. Shoji. Growth mechanism for spherical carbon particles in a dc methane plasma. *Physics of Plasmas*, 15(5):050702, 2008.

[16] L. Wörner, E. Kovacevic, J. Berndt, H. M. Thomas, M. H. Thoma, L. Boufendi, and G. E. Morfill. The formation and transport phenomena of nanometre-sized particles in a dc plasma. *New Journal of Physics*, 14(2):023024, 2012.

[17] T. Ishigaki, T. Sato, Y. Moriyoshi, and M. I. Boulos. Influence of plasma modification of titanium carbide powder on its sintering properties. *Journal of materials science letters*, 14(23):1694–1697, 1995.

[18] H. Kersten, H. Deutsch, E. Stoffels, W. W. Stoffels, G. M. W. Kroesen, and R. Hippler. Micro-disperse particles in plasmas: From disturbing side effects to new applications. *Contributions to Plasma Physics*, 41(6):598–609, 2001.

[19] O. Havnes, T. Aslaksen, T. W. Hartquist, F. Li, F. Melandsø, G. E. Morfill, and T. Nitter. Probing the properties of planetary ring dust by the observation of mach cones. *Journal of Geophysical Research: Space Physics*, 100(A2):1731–1734, 1995.

[20] O. Havnes, F. Li, F. Melandso/, T. Aslaksen, T. W. Hartquist, G. E. Morfill, T. Nitter, and V. Tsytovich. Diagnostic of dusty plasma conditions by the observation of mach cones caused by dust acoustic waves. *Journal of Vacuum Science & Technology A: Vacuum, Surfaces, and Films*, 14(2):525–528, 1996.

[21] C. K. Goertz. Dusty plasmas in the solar system. *Reviews of Geophysics*, 27(2):271–292, 1989.

[22] T. G. Northrop. Dusty plasmas. *Physica Scripta*, 45(5):475, 1992.

[23] V. N. Tsytovich. Dust plasma crystals, drops, and clouds. *Physics-Uspekhi*, 40(1):53, 1997.

[24] T. A. Ellis and J. S. Neff. Numerical simulation of the emission and motion of neutral and charged dust from p/halley. *Icarus*, 91(2):280–296, 1991.

[25] M. Horanyi and D. A. Mendis. Trajectories of charged dust grains in the cometary environment. *The Astrophysical Journal*, 294:357–368, 1985.

[26] B. P. Pandey, V. Krishan, and M. Roy. Effect of radiative cooling on collapsing charged grains. *Pramana*, 56(1):95–105, 2001.

[27] G. E. Morfill, A. V. Ivlev, and H. M. Thomas. Complex (dusty) plasmas—kinetic studies of strong coupling phenomena a. *Physics of Plasmas*, 19(5):055402, 2012.

[28] N. S. Schulz. *From dust to stars: studies of the formation and early evolution of stars.* Springer Science & Business Media, Cambridge, Massachusetts, USA, 2007.

[29] C. J. Mitchell, M. Horányi, O. Havnes, and C. C. Porco. Saturn's spokes: Lost and found. *Science*, 311(5767):1587–1589, 2006.

[30] O. Ishihara. Complex plasma: dusts in plasma. *Journal of Physics D: Applied Physics*, 40(8):R121, 2007.

[31] C. K. Goertz and G. Morfill. A model for the formation of spokes in saturn's ring. *Icarus*, 53(2):219–229, 1983.

[32] C. A. McGhee, R. G. French, L. Dones, Jeffrey N. C., H. J. Salo, and R. Danos. Hst observations of spokes in saturn's b ring. *Icarus*, 173(2):508–521, 2005.

[33] L. R. Doyle and E. Grün. Radiative transfer modeling constraints on the size of the spoke particles in saturn's rings. *Icarus*, 85(1):168–190, 1990.

[34] P. Grego. *Blazing a Ghostly Trail.* Springer, St Dennis, Cornwall, UK, 2014.

[35] F. Balsiger, E. Kopp, M. Friedrich, K. M. Torkar, U. Wälchli, and G. Witt. Positive ion depletion in a noctilucent cloud. *Geophysical research letters*, 23(1):93–96, 1996.

[36] O. Havnes, J. Trøim, T. Blix, W. Mortensen, L. I. Næsheim, E. Thrane, and T. Tønnesen. First detection of charged dust particles in the earth's mesosphere. *Journal of Geophysical Research: Space Physics*, 101(A5):10839–10847, 1996.

[37] J. Y. N. Cho and M. C. Kelley. Polar mesosphere summer radar echoes: Observations and current theories. *Reviews of Geophysics*, 31(3):243–265, 1993.

[38] M. Kollmann. Single-file diffusion of atomic and colloidal systems: asymptotic laws. *Physical review letters*, 90(18):180602, 2003.

[39] A. Ivlev, L. Hartmut, G. E. Morfill, and C. P. Royall. *Complex plasmas and colloidal dispersions: particle-resolved studies of classical liquids and solids*, volume 5. World Scientific Publishing Co Inc, Singapore, 2012.

[40] B. M. Annaratone, T. Antonova, D. D. Goldbeck, H. M. Thomas, and G. E. Morfill. Complex-plasma manipulation by radiofrequency biasing. *Plasma physics and controlled fusion*, 46(12B):B495, 2004.

[41] Dirk D. G. *Analyse dynamischer Volumenprozesse in komplexen Plasmen.* PhD thesis, Ludwig-Maximilians-Universität München, 2003.

[42] T. Palberg. Crystallization kinetics of repulsive colloidal spheres. *Journal of Physics: Condensed Matter*, 11(28):R323, 1999.

[43] E. Thomas Jr and J. Williams. Applications of stereoscopic particle image velocimetry: Dust acoustic waves and velocity space distribution functions. *Physics of plasmas*, 13(5):055702, 2006.

[44] M. Chaudhuri, V. Nosenko, and H. M. Thomas. Dust interferometers in plasmas. *Physical Review E*, 93(3):031201, 2016.

[45] V. Nosenko, S. Zhdanov, and G. Morfill. Supersonic dislocations observed in a plasma crystal. *Physical review letters*, 99(2):025002, 2007.

[46] V. Nosenko, G. E. Morfill, and P. Rosakis. Direct experimental measurement of the speed-stress relation for dislocations in a plasma crystal. *Physical review letters*, 106(15):155002, 2011.

[47] S. Khrapak, D. Samsonov, G. Morfill, H. Thomas, V. Yaroshenko, H. Rothermel, T. Hagl, V. Fortov, A. Nefedov, V. Molotkov, et al. Compressional waves in complex (dusty) plasmas under microgravity conditions. *Physics of Plasmas*, 10(1):1–4, 2003.

[48] S. Nunomura, S. Zhdanov, D. Samsonov, and G. Morfill. Wave spectra in solid and liquid complex (dusty) plasmas. *Physical review letters*, 94(4):045001, 2005.

[49] S. Nunomura, D. Samsonov, S. Zhdanov, and G. Morfill. Heat transfer in a two-dimensional crystalline complex (dusty) plasma. *Physical review letters*, 95(2):025003, 2005.

[50] V. Nosenko, S. Zhdanov, A. V. Ivlev, G. Morfill, J. Goree, and A. Piel. Heat transport in a two-dimensional complex (dusty) plasma at melting conditions. *Physical review letters*, 100(2):025003, 2008.

[51] S. Hamaguchi, R. T. Farouki, and D. H. E. Dubin. Triple point of yukawa systems. *Physical Review E*, 56(4):4671, 1997.

[52] M. H. Thoma, Martin A. Fink, H. Hofner, M. Kretschmer, S. A. Khrapak, S. V. Ratynskaia, V. V. Yaroshenko, G. E. Morfill, O. F. Petrov, A. D. Usachev, et al. Pk-4: Complex plasmas in space—the next generation. *IEEE transactions on plasma science*, 35(2):255–259, 2007.

[53] D. Banerjee, S. Garai, M. S. Janaki, and N. Chakrabarti. Kelvin-helmholtz instability in non-newtonian complex plasma. *Physics of Plasmas*, 20(7):073702, 2013.

[54] S. Garai, D. Banerjee, M. S. Janaki, and N. Chakrabarti. Stabilization of rayleigh-taylor instability in a non-newtonian incompressible complex plasma. *Physics of Plasmas*, 22(3):033702, 2015.

[55] V. Nosenko, A. V. Ivlev, and G. E. Morfill. Anisotropic shear melting and recrystallization of a two-dimensional complex plasma. *Physical Review E*, 87(4):043115, 2013.

Page 48

[56] A. V. Ivlev, V. Steinberg, R. Kompaneets, H. Höfner, I. Sidorenko, and G. E. Morfill. Non-newtonian viscosity of complex-plasma fluids. *Physical review letters*, 98(14):145003, 2007.

[57] S. K. Zhdanov, A. V. Ivlev, and G. E. Morfill. Non-hamiltonian dynamics of grains with spatially varying charges. *Physics of plasmas*, 12(7):072312, 2005.

[58] M. Chaudhuri, A. V. Ivlev, S. A. Khrapak, H. M. Thomas, and G. E. Morfill. Complex plasma—the plasma state of soft matter. *Soft Matter*, 7(4):1287–1298, 2011.

[59] Jörg G. B. *Statistical mechanics where Newton's third law is broken*. PhD thesis, Heinrich-Heine-Universität Düsseldorf, 2015.

[60] J. E. Allen. Probe theory-the orbital motion approach. *Physica Scripta*, 45(5):497, 1992.

[61] T. Matsoukas and M. Russell. Particle charging in low-pressure plasmas. *Journal of Applied Physics*, 77(9):4285–4292, 1995.

[62] A. V. Zobnin, A. P. Nefedov, V. A. Sinel'Shchikov, and V. E. Fortov. On the charge of dust particles in a low-pressure gas discharge plasma. *Journal of Experimental and Theoretical Physics*, 91(3):483–487, 2000.

[63] M. Lampe, R. Goswami, Z. Sternovsky, S. Robertson, V. Gavrishchaka, G. Ganguli, and G. Joyce. Trapped ion effect on shielding, current flow, and charging of a small object in a plasma. *Physics of Plasmas*, 10(5):1500–1513, 2003.

[64] I. H. Hutchinson and L. Patacchini. Computation of the effect of neutral collisions on ion current to a floating sphere in a stationary plasma. *Physics of Plasmas*, 14(1):013505, 2007.

[65] A. V. Zobnin, A. D. Usachev, O. F. Petrov, and V. E. Fortov. Ion current on a small spherical attractive probe in a weakly ionized plasma with ion-neutral collisions (kinetic approach). *Physics of plasmas*, 15(4):043705, 2008.

[66] S. A. Khrapak, S. V. Ratynskaia, A. V. Zobnin, A. D. Usachev, V. V. Yaroshenko, M. H. Thoma, M. Kretschmer, H. Höfner, G. E. Morfill, O. F. Petrov, et al. Particle charge in the bulk of gas discharges. *Physical Review E*, 72(1):016406, 2005.

[67] S. Khrapak and G. Morfill. Basic processes in complex (dusty) plasmas: Charging, interactions, and ion drag force. *Contributions to Plasma Physics*, 49(3):148–168, 2009.

[68] A. Ashkin. Acceleration and trapping of particles by radiation pressure. *Physical review letters*, 24(4):156, 1970.

[69] M. Wolter and A. Melzer. Laser heating of particles in dusty plasmas. *Physical Review E*, 71(3):036414, 2005.

[70] V. Nosenko, A. V. Ivlev, and G. E. Morfill. Microstructure of a liquid two-dimensional dusty plasma under shear. *Physical review letters*, 108(13):135005, 2012.

[71] J. Goree, G. E. Morfill, V. N. Tsytovich, and S. V. Vladimirov. Theory of dust voids in plasmas. *Physical Review E*, 59(6):7055, 1999.

[72] V. N. Tsytovich, S. V. Vladimirov, G. E. Morfill, and J. Goree. Theory of collision-dominated dust voids in plasmas. *Physical Review E*, 63(5):056609, 2001.

[73] M. R. Akdim and W. J. Goedheer. Modeling of self-excited dust vortices in complex plasmas under microgravity. *Physical Review E*, 67(5):056405, 2003.

[74] T. Bockwoldt, O. Arp, K. O. Menzel, and A. Piel. On the origin of dust vortices in complex plasmas under microgravity conditions. *Physics of Plasmas*, 21(10):103703, 2014.

[75] L. J. Hou, Y. N. Wang, and Z. L. Mišković. Formation and rotation of two-dimensional coulomb crystals in magnetized complex plasma. *Physics of plasmas*, 12(4):042104, 2005.

[76] U. Konopka, D. Samsonov, A. V. Ivlev, J. Goree, V. Steinberg, and G. E. Morfill. Rigid and differential plasma crystal rotation induced by magnetic fields. *Physical Review E*, 61(2):1890, 2000.

[77] L. Patacchini and I. H. Hutchinson. Fully self-consistent ion-drag-force calculations for dust in collisional plasmas with an external electric field. *Physical review letters*, 101(2):025001, 2008.

[78] I. H. Hutchinson. Collisionless ion drag force on a spherical grain. *Plasma physics and controlled fusion*, 48(2):185, 2006.

[79] M. S. Barnes, J. H. Keller, J. C. Forster, J. A. O'Neill, and D. K. Coultas. Transport of dust particles in glow-discharge plasmas. *Physical review letters*, 68(3):313, 1992.

[80] S. A. Khrapak, A. V. Ivlev, G. E. Morfill, and H. M. Thomas. Ion drag force in complex plasmas. *Physical review E*, 66(4):046414, 2002.

[81] P. S. Epstein. On the resistance experienced by spheres in their motion through gases. *Physical Review*, 23(6):710, 1924.

[82] B. Liu, J. Goree, V. Nosenko, and L. Boufendi. Radiation pressure and gas drag forces on a melamine-formaldehyde microsphere in a dusty plasma. *Physics of Plasmas*, 10(1):9–20, 2003.

[83] H. Rothermel, T. Hagl, G. E. Morfill, M. H. Thoma, and H. M. Thomas. Gravity compensation in complex plasmas by application of a temperature gradient. *Physical review letters*, 89(17):175001, 2002.

[84] www.microparticles.de. Microparticles gmbh, 2018.

[85] B. Tadsen, F. Greiner, and A. Piel. Preparation of magnetized nanodusty plasmas in a radio frequency-driven parallel-plate reactor. *Physics of Plasmas*, 21(10):103704, 2014.

[86] S. Mitic, M. Y. Pustylnik, and G. E. Morfill. Spectroscopic evaluation of the effect of the microparticles on radiofrequency argon plasma. *New Journal of Physics*, 11(8):083020, 2009.

[87] S. Mitic, R. Sütterlin, A. V. Ivlev H. Höfner, M. H. Thoma, S. Zhdanov, and G. E. Morfill. Convective dust clouds driven by thermal creep in a complex plasma. *Physical review letters*, 101(23):235001, 2008.

[88] G. E. Morfill, H. M. Thomas, U. Konopka, H. Rothermel, M. Zuzic, A. Ivlev, and J. Goree. Condensed plasmas under microgravity. *Physical review letters*, 83(8):1598, 1999.

[89] V. E. Fortov, A. P. Nefedov, O. S. Vaulina, A. M. Lipaev, V. I. Molotkov, A. A. Samaryan, V. P. Nikitskii, A. I. Ivanov, S. F. Savin, A. V. Kalmykov, et al. Dusty plasma induced by solar radiation under microgravitational conditions: an experiment on board the mir orbiting space station. *Journal of Experimental and Theoretical Physics*, 87(6):1087–1097, 1998.

[90] S. A. Khrapak, B. A. Klumov, P. Huber, V. I. Molotkov, A. M. Lipaev, V. N. Naumkin, A. V. Ivlev, H. M. Thomas, M. Schwabe, G. E. Morfill, et al. Fluid-solid phase transitions in three-dimensional complex plasmas under microgravity conditions. *Physical Review E*, 85(6):066407, 2012.

[91] V. E. Fortov, O. S. Vaulina, O. F. Petrov, V. I. Molotkov, A. V. Chernyshev, A.M. Lipaev, G. Morfill, H. Thomas, H. Rotermell, S. A. Khrapak, et al. Dynamics of macroparticles in a dusty plasma under microgravity conditions (first experiments on board the iss). *Journal of Experimental and Theoretical Physics*, 96(4):704–718, 2003.

[92] H. M. Thomas and G. E. Morfill. Melting dynamics of a plasma crystal. *Nature*, 379(806), 1996.

[93] V. E. Fortov, A. V. Ivlev, S. A. Khrapak, A. G. Khrapak, and G. E. Morfill. Complex (dusty) plasmas: Current status, open issues, perspectives. *Physics reports*, 421(1):1–103, 2005.

[94] C. Dietz, T. Kretz, and M. H. Thoma. Machine-learning approach for local classification of crystalline structures in multiphase systems. *Physical Review E*, 96(1):011301, 2017.

[95] C. Dietz and M. H. Thoma. Investigation and improvement of three-dimensional plasma crystal analysis. *Physical Review E*, 94(3):033207, 2016.

[96] M. O. Robbins, K. Kremer, and G. S. Grest. Phase diagram and dynamics of yukawa systems. *The Journal of chemical physics*, 88(5):3286–3312, 1988.

[97] M. J. Stevens and M. O. Robbins. Melting of yukawa systems: a test of phenomenological melting criteria. *The Journal of chemical physics*, 98(3):2319–2324, 1993.

[98] E. J. Meijer and D. Frenkel. Melting line of yukawa system by computer simulation. *The Journal of chemical physics*, 94(3):2269–2271, 1991.

[99] S. A. Khrapak, A. V. Ivlev, and G. E. Morfill. Momentum transfer in complex plasmas. *Physical Review E*, 70(5):056405, 2004.

[100] S. Ichimaru. Strongly coupled plasmas: high-density classical plasmas and degenerate electron liquids. *Reviews of Modern Physics*, 54(4):1017, 1982.

[101] D. H. E. Dubin. First-order anharmonic correction to the free energy of a coulomb crystal in periodic boundary conditions. *Physical Review A*, 42(8):4972, 1990.

[102] O. S. Vaulina and S. A. Khrapak. Scaling law for the fluid-solid phase transition in yukawa systems (dusty plasmas). *Journal of Experimental and Theoretical Physics*, 90(2):287–289, 2000.

[103] B. Fultz. *Phase Transitions in Materials*. Cambridge University Press, Cambridge, UK, 2014.

[104] H. C. Lee, D. Y. Chen, and B. Rosenstein. Phase diagram of crystals of dusty plasma. *Physical Review E*, 56(4):4596, 1997.

[105] G. Joyce, M. Lampe, and G. Ganguli. Instability-triggered phase transition to a dusty-plasma condensate. *Physical review letters*, 88(9):095006, 2002.

[106] I. A. Martynova and I. L. Iosilevskiy. Features of phase transitions in models of complex plasma. *Contributions to Plasma Physics*, 56(5):432–441, 2016.

[107] V. Nosenko, S. K. Zhdanov, A. V. Ivlev, C. A. Knapek, and G. E. Morfill. 2d melting of plasma crystals: equilibrium and nonequilibrium regimes. *Physical review letters*, 103(1):015001, 2009.

[108] S. T. Chui. Grain-boundary theory of melting in two dimensions. *Physical Review B*, 28(1):178, 1983.

[109] S. T. Chui. Grain-boundary theory of melting in two dimensions. *Physical Review Letters*, 48(14):933, 1982.

[110] J. M. Kosterlitz. Kosterlitz–thouless physics: a review of key issues. *Reports on Progress in Physics*, 79(2):026001, 2016.

[111] J. M. Kosterlitz and D. J. Thouless. Ordering, metastability and phase transitions in two-dimensional systems. *Journal of Physics C: Solid State Physics*, 6(7):1181, 1973.

[112] D. R. Nelson and B. I. Halperin. Dislocation-mediated melting in two dimensions. *Physical Review B*, 19(5):2457, 1979.

[113] A. P. Young. Melting and the vector coulomb gas in two dimensions. *Physical Review B*, 19(4):1855, 1979.

[114] D. R. Nelson. *Defects and geometry in condensed matter physics*. Cambridge University Press, Cambridge, UK, 2002.

[115] B. I. Halperin and D. R. Nelson. Theory of two-dimensional melting. *Physical Review Letters*, 41(2):121, 1978.

[116] R. A. Quinn, C. Cui, J. Goree, J. B. Pieper, H. Thomas, and G. E. Morfill. Structural analysis of a coulomb lattice in a dusty plasma. *Physical Review E*, 53(3):R2049, 1996.

[117] G. E. Astrakharchik, A. I. Belousov, and Y. E. Lozovik. Two-dimensional mesoscopic dusty plasma clusters: Structure and phase transitions. *Journal of Experimental and Theoretical Physics*, 89(4):696–703, 1999.

[118] G. E. Astrakharchik, A. I. Belousov, and Y. E. Lozovik. Properties of two-dimensional dusty plasma clusters. *Physics Letters A*, 258(2):123–130, 1999.

[119] A. C. Levi and M. Kotrla. Theory and simulation of crystal growth. *Journal of Physics: Condensed Matter*, 9(2):299, 1997.

[120] T. Terao and T. Nakayama. Sol-gel transition of reversible cluster-cluster aggregations. *Physical Review E*, 58(3):3490, 1998.

[121] J. C. Gimel, D. Durand, and T. Nicolai. Transition between flocculation and percolation of a diffusion-limited cluster-cluster aggregation process using three-dimensional monte carlo simulation. *Physical Review B*, 51(17):11348, 1995.

[122] T. Vicsek. *Fractal Growth Phenomena*. World Scientific, Singapore, second edition, 1992.

[123] A. Aharony and D. Stauffer. *Introduction to percolation theory*. Taylor & Francis, London, second edition, 2003.

[124] S. D. Orrite, S. Stoll, and P. Schurtenberger. Off-lattice monte carlo simulations of irreversible and reversible aggregation processes. *Soft Matter*, 1(5):364–371, 2005.

[125] T. Ma and S. Wang. *Phase transition dynamics*. Springer, Cambridge, UK, 2014.

[126] S. Puri. Kinetics of phase transitions. *Phase Transitions*, 77(5-7):407–431, 2004.

[127] J. W. Cahn. Phase separation by spinodal decomposition in isotropic systems. *The Journal of Chemical Physics*, 42(1):93–99, 1965.

[128] K. R. Sütterlin, A. Wysocki, C. Räth, A. V. Ivlev, H. M. Thomas, S. Khrapak, S. Zhdanov, M. Rubin-Zuzic, W. J. Goedheer, V. E. Fortov, et al. Non-equilibrium phase transitions in complex plasma. *Plasma Physics and Controlled Fusion*, 52(12):124042, 2010.

[129] G. C. Maitland, M. Rigby, E. B. Smith, and W. A. Wakeham. Intermolecular forces clarendon, 1981.

[130] G. E. Morfill, U. Konopka, M. Kretschmer, M. Rubin-Zuzic, H. M. Thomas, S. K. Zhdanov, and V. Tsytovich. The 'classical tunnelling effect'—observations and theory. *New Journal of Physics*, 8(1):7, 2006.

[131] M. Mikikian, L. Boufendi, A. Bouchoule, H. M. Thomas, G. E. Morfill, A. P. Nefedov, V. E. Fortov, et al. Formation and behaviour of dust particle clouds in a radio-frequency discharge: results in the laboratory and under microgravity conditions. *New Journal of Physics*, 5(1):19, 2003.

[132] A. Wysocki, C. Räth, A. V Ivlev, K. R. Sütterlin, H. M. Thomas, S. Khrapak, S. Zhdanov, V. E. Fortov, A. M. Lipaev, V. I. Molotkov, et al. Kinetics of fluid demixing in complex plasmas: role of two-scale interactions. *Physical review letters*, 105(4):045001, 2010.

[133] A. V. Ivlev, S. K. Zhdanov, H. M. Thomas, and G. E. Morfill. Fluid phase separation in binary complex plasmas. *EPL (Europhysics Letters)*, 85(4):45001, 2009.

[134] K. R. Sütterlin, A. Wysocki, A. V. Ivlev, C. Räth, H. M. Thomas, M. Rubin-Zuzic, W. J. Goedheer, V. E. Fortov, A. M. Lipaev, V. I. Molotkov, et al. Dynamics of lane formation in driven binary complex plasmas. *Physical review letters*, 102(8):085003, 2009.

[135] C. Killer, T. Bockwoldt, S. Schütt, M. Himpel, A. Melzer, and A. Piel. Phase separation of binary charged particle systems with small size disparities using a dusty plasma. *Physical review letters*, 116(11):115002, 2016.

[136] M. Y. Pustylnik, M. A. Fink, V. Nosenko, T. Antonova, T. Hagl, H. M. Thomas, A. V. Zobnin, A. M. Lipaev, A. D. Usachev, V. I. Molotkov, et al. Plasmakristall-4: New complex (dusty) plasma laboratory on board the international space station. *Review of Scientific Instruments*, 87(9):093505, 2016.

[137] M. Schwabe, U. Konopka, P. Bandyopadhyay, and G. E. Morfill. Pattern formation in a complex plasma in high magnetic fields. *Physical review letters*, 106(21):215004, 2011.

[138] M. Zuzic, A. V. Ivlev, J. Goree, G. E. Morfill, H. M. Thomas, H. Rothermel, U. Konopka, R. Sütterlin, and D. D. Goldbeck. Three-dimensional strongly coupled plasma crystal under gravity conditions. *Physical review letters*, 85(19):4064, 2000.

[139] J. C. Crocker and D. G. Grier. Methods of digital video microscopy for colloidal studies. *Journal of colloid and interface science*, 179(1):298–310, 1996.

[140] H. J. Raveche, R. D. Mountain, and W. B. Streett. Freezing and melting properties of the lennard-jones system. *The Journal of Chemical Physics*, 61(5):1970–1984, 1974.

[141] R. Agrawal and D. A. Kofke. Thermodynamic and structural properties of model systems at solid-fluid coexistence: I. fcc and bcc soft spheres. *Molecular physics*, 85(1):23–42, 1995.

[142] J. C. G. Montoro and J. L. F. Abascal. The voronoi polyhedra as tools for structure determination in simple disordered systems. *The Journal of Physical Chemistry*, 97(16):4211–4215, 1993.

[143] W. Lechner and C. Dellago. Accurate determination of crystal structures based on averaged local bond order parameters. *The Journal of chemical physics*, 129(11):114707, 2008.

[144] A. S. Keys and S. C. Glotzer. How do quasicrystals grow? *Physical review letters*, 99(23):235503, 2007.

[145] S. Auer and D. Frenkel. Numerical prediction of absolute crystallization rates in hard-sphere colloids. *The Journal of chemical physics*, 120(6):3015–3029, 2004.

[146] P. Rein ten Wolde, M. J. Ruiz-Montero, and D. Frenkel. Numerical calculation of the rate of crystal nucleation in a lennard-jones system at moderate undercooling. *The Journal of chemical physics*, 104(24):9932–9947, 1996.

[147] P. R. Ten Wolde, M. J. Ruiz-Montero, and D. Frenkel. Numerical evidence for bcc ordering at the surface of a critical fcc nucleus. *Physical review letters*, 75(14):2714, 1995.

[148] A. B. de Oliveira, P. A. Netz, T. Colla, and M. C. Barbosa. Structural anomalies for a three dimensional isotropic core-softened potential. *The Journal of chemical physics*, 125(12):124503, 2006.

[149] F. Ziese, G. Maret, and U. Gasser. Heterogeneous nucleation and crystal growth on curved surfaces observed by real-space imaging. *Journal of Physics: Condensed Matter*, 25(37):375105, 2013.

[150] V. Senthil Kumar and V. Kumaran. Bond-orientational analysis of hard-disk and hard-sphere structures. *The Journal of chemical physics*, 124(20):204508, 2006.

[151] W. Mickel, S. C. Kapfer, G. E. Schröder-Turk, and K. Mecke. Shortcomings of the bond orientational order parameters for the analysis of disordered particulate matter. *The Journal of chemical physics*, 138(4):044501, 2013.

[152] A. V. Ivlev, G. E. Morfill, H. M. Thomas, C. Räth, G. Joyce, P. Huber, R. Kompaneets, V. E. Fortov, A. M. Lipaev, V. I. Molotkov, et al. First observation of electrorheological plasmas. *Physical review letters*, 100(9):095003, 2008.

[153] D. Mueller, T. M. Link, R. Monetti, J. Bauer, H. Boehm, V. Seifert-Klauss, E. J. Rummeny, G. E. Morfill, and C. Raeth. The 3d-based scaling index algorithm: a new structure measure to analyze trabecular bone architecture in high-resolution mr images in vivo. *Osteoporosis international*, 17(10):1483–1493, 2006.

[154] C. Räth, P. Schuecker, and A. J. Banday. A scaling index analysis of the wilkinson microwave anisotropy probe three-year data: signatures of non-gaussianities and asymmetries in the cosmic microwave background. *Monthly Notices of the Royal Astronomical Society*, 380(2):466–478, 2007.

[155] G. Rossmanith, H. Modest, C. Räth, A. J. Banday, K. M. Górski, and G. Morfill. Search for non-gaussianities in the wmap data with the scaling index method. *Advances in Astronomy*, 2011, 2011.

[156] F. Jamitzky, R. W. Stark, W. Bunk, S. Thalhammer, C. Räth, T. Aschenbrenner, G. E. Morfill, and W. M. Heckl. Scaling-index method as an image processing tool in scanning-probe microscopy. *Ultramicroscopy*, 86(1):241–246, 2001.

[157] C. Räth, R. Monetti, J. Bauer, I. Sidorenko, D. Müller, M. Matsuura, E. M. Lochmüller, P. Zysset, and F. Eckstein. Strength through structure: visualization and local assessment of the trabecular bone structure. *New Journal of Physics*, 10(12):125010, 2008.

[158] R. A. Monetti, W. Bunk, F. Jamitzky, C. Raeth, and G. Morfill. Detecting nonlinearities in data sets. characterization of fourier phase maps using the weighted scaling indices. *arXiv preprint physics/0405130*, 2004.

[159] K. Jiang, C. R. Du, K. R. Sütterlin, A. V. Ivlev, and G. E. Morfill. Lane formation in binary complex plasmas: Role of non-additive interactions and initial configurations. *EPL (Europhysics Letters)*, 92(6):65002, 2010.

[160] K. R. Sutterlin, H. M. Thomas, A. V. Ivlev, G. E. Morfill, V. E. Fortov, A. M. Lipaev, V. I. Molotkov, O. F. Petrov, A. Wysocki, and H. Lowen. Lane formation in driven binary complex plasmas on the international space station. *IEEE Transactions on Plasma Science*, 38(4):861–868, 2010.

[161] E. S Dzlieva, M. A. Ermolenko, V. Y. Karasev, S. I. Pavlov, L. A. Novikov, and S. A. Mayorov. Control of ion drag in a dusty plasma. *Pis' ma v Zhurnal Èksperimental'noi i Teoreticheskoi Fiziki*, 100(11):801–806, 2014.

[162] Y. Ivanov and A. Melzer. Melting dynamics of finite clusters in dusty plasmas. *Physics of plasmas*, 12(7):072110, 2005.

[163] R. Ichiki, Y. Ivanov, M. Wolter, Y. Kawai, and A. Melzer. Melting and heating of two-dimensional coulomb clusters in dusty plasmas. *Physical Review E*, 70(6):066404, 2004.

[164] A. Melzer, V. A. Schweigert, I. V. Schweigert, A. Homann, S. Peters, and A. Piel. Structure and stability of the plasma crystal. *Physical Review E*, 54(1):R46, 1996.

[165] A. Melzer, A. Homann, and A. Piel. Experimental investigation of the melting transition of the plasma crystal. *Physical Review E*, 53(3):2757, 1996.

[166] L.-J. Hou, Y.-N. Wang, and Z. L. Mišković. Induced potential of a dust particle in a collisional radio-frequency sheath. *Physical Review E*, 68(1):016410, 2003.

[167] V. A. Schweigert, I. V. Schweigert, A. Melzer, A. Homann, and A. Piel. Plasma crystal melting: a nonequilibrium phase transition. *Physical review letters*, 80(24):5345, 1998.

[168] V. A. Schweigert, I. V. Schweigert, A. Melzer, A. Homann, and A. Piel. Alignment and instability of dust crystals in plasmas. *Physical Review E*, 54(4):4155, 1996.

[169] D. Block, M. Kroll, O. Arp, A. Piel, S. Käding, Y. Ivanov, A. Melzer, C. Henning, H. Baumgartner, P. Ludwig, et al. Structural and dynamical properties of yukawa balls. *Plasma Physics and Controlled Fusion*, 49(12B):B109, 2007.

[170] O. Arp, D. Block, A. Piel, and A. Melzer. Dust coulomb balls: three-dimensional plasma crystals. *Physical review letters*, 93(16):165004, 2004.

[171] H. Thomsen and M. Bonitz. Resolving structural transitions in spherical dust clusters. *Physical Review E*, 91(4):043104, 2015.

[172] H. Baumgartner, H. Kählert, V. Golobnychiy, C. Henning, S. Käding, A. Melzer, and M. Bonitz. Shell structure of yukawa balls. *Contributions to Plasma Physics*, 47(4-5):281–290, 2007.

[173] A. Piel. Plasma crystals-structure and dynamics. *Plasma and Fusion Research*, 4:013–013, 2009.

[174] A. Schella, T. Miksch, A. Melzer, J. Schablinski, D. Block, A. Piel, H. Thomsen, P. Ludwig, and M. Bonitz. Melting scenarios for three-dimensional dusty plasma clusters. *Physical Review E*, 84(5):056402, 2011.

[175] O. Arp, D. Block, M. Klindworth, and A. Piel. Confinement of coulomb balls. *Physics of plasmas*, 12(12):122102, 2005.

[176] M. Kroll, J. Schablinski, D. Block, and A. Piel. On the influence of wakefields on three-dimensional particle arrangements. *Physics of Plasmas*, 17(1):013702, 2010.

Page 57

[177] C. Killer, A. Schella, T. Miksch, and A. Melzer. Vertically elongated three-dimensional yukawa clusters in dusty plasmas. *Physical Review B*, 84(5):054104, 2011.

[178] V. Molotkov, H. Thomas, A. Lipaev, V. Naumkin, A. Ivlev, and S. Khrapak. Complex (dusty) plasma research under microgravity conditions: Pk-3 plus laboratory on the international space station. *International Journal of Microgravity Science and Application*, 35:320302, 2015.

[179] H. Thomas, G. E. Morfill, V. Demmel, J. Goree, B. Feuerbacher, and D. Möhlmann. Plasma crystal: Coulomb crystallization in a dusty plasma. *Physical Review Letters*, 73(5):652, 1994.

[180] S. A. Khrapak and G. E. Morfill. Ionization enhanced ion collection by a small floating grain in plasmas. *Physics of Plasmas*, 19(2):024510, 2012.

[181] M. Klindworth, O. Arp, and A. Piel. Langmuir probe diagnostics in the impf device and comparison with simulations and tracer particle experiments. *Journal of Physics D: Applied Physics*, 39(6):1095, 2006.

[182] H. M. Thomas, G. E. Morfill, V. E. Fortov, A. V. Ivlev, V. I. Molotkov, A. M. Lipaev, T. Hagl, H. Rothermel, S. A. Khrapak, R. K. Suetterlin, et al. Complex plasma laboratory pk-3 plus on the international space station. *New journal of physics*, 10(3):033036, 2008.

[183] C. Dietz, R. Bergert, B. Steinmüller, M. Kretschmer, S. Mitic, and M. H. Thoma. fcc-bcc phase transition in plasma crystals using time-resolved measurements. *Physical Review E*, 97(4):043203, 2018.

[184] P. Huber. *Untersuchung von 3-D Plasmakristallen*. PhD thesis, München, 2011.

[185] C. Rose-Petruck, R. Jimenez, T. Guo, A. Cavalleri, C. W. Siders, F. Rksi, J. A. Squier, B. C. Walker, K. R. Wilson, and C. PJ. Barty. Picosecond–milliångström lattice dynamics measured by ultrafast x-ray diffraction. *Nature*, 398(6725):310–312, 1999.

[186] C. W. Siders, A. Cavalleri, K. Sokolowski-Tinten, C. Toth, T. Guo, M. Kammler, M. H. Von Hoegen, K. R. Wilson, D. von der Linde, and C. PJ Barty. Detection of nonthermal melting by ultrafast x-ray diffraction. *Science*, 286(5443):1340–1342, 1999.

[187] J. Anwar and D. Zahn. Uncovering molecular processes in crystal nucleation and growth by using molecular simulation. *Angewandte Chemie International Edition*, 50(9):1996–2013, 2011.

[188] T. E. Sheridan. Melting transition in a two-dimensional complex plasma heated by driven acoustic instability. *Physics of Plasmas*, 15(10):103702, 2008.

[189] V. Nosenko, J. Goree, and A. Piel. Laser method of heating monolayer dusty plasmas. *Physics of plasmas*, 13(3):032106, 2006.

[190] C. A. Knapek, D. Samsonov, S. Zhdanov, U. Konopka, and G. E. Morfill. Recrystallization of a 2d plasma crystal. *Physical review letters*, 98(1):015004, 2007.

[191] M. Rubin-Zuzic, G. E. Morfill, A. V. Ivlev, R. Pompl, B. A. Klumov, W. Bunk, H. M. Thomas, H. Rothermel, O. Havnes, and A. Fouquet. Kinetic development of crystallization fronts in complex plasmas. *Nature Physics*, 2(3), 2006.

[192] J. P. Hoogenboom, A. Yethiraj, A. K. van Langen-Suurling, J. Romijn, and A. Van Blaaderen. Epitaxial crystal growth of charged colloids. *Physical review letters*, 89(25):256104, 2002.

[193] B. J. Ackerson and K. Schätzel. Classical growth of hard-sphere colloidal crystals. *Physical Review E*, 52(6):6448, 1995.

[194] A. P. Gast and Y. Monovoukas. A new growth instability in colloidal crystallization. *Nature*, 351(6327):553–555, 1991.

[195] W. B. Russel, P. M. Chaikin, J. Zhu, W. V. Meyer, and R. Rogers. Dendritic growth of hard sphere crystals. *Langmuir*, 13(14):3871–3881, 1997.

[196] M. Würth, J. Schwarz, F. Culis, P. Leiderer, and T. Palberg. Growth kinetics of body centered cubic colloidal crystals. *Physical Review E*, 52(6):6415, 1995.

[197] M. Kolb and R. Jullien. Chemically limited versus diffusion limited aggregation. *Journal de Physique Lettres*, 45(20):977–981, 1984.

[198] Y. He, B. Olivier, and B. J. Ackerson. Morphology of crystals made of hard spheres. *Langmuir*, 13(6):1408–1412, 1997.

[199] T. Palberg. Colloidal crystallization dynamics. *Current opinion in colloid & interface science*, 2(6):607–614, 1997.

[200] S. Buczkowski, S. Kyriacos, F. Nekka, and L. Cartilier. The modified box-counting method: analysis of some characteristic parameters. *Pattern Recognition*, 31(4):411–418, 1998.

[201] J. S. Rowlinson and F. L. Swinton. *Liquids and liquid mixtures: Butterworths monographs in chemistry*. Butterworth-Heinemann, Oxford, UK, 2013.

[202] L. D. Gelb, K. E. Gubbins, R. Radhakrishnan, and M. Sliwinska-Bartkowiak. Phase separation in confined systems. *Reports on Progress in Physics*, 62(12):1573, 1999.

[203] M. Majka and P. F. Góra. Analytical theory of effective interactions in binary colloidal systems of soft particles. *Physical Review E*, 90(3):032303, 2014.

[204] A. Böbel and C. Räth. Kinetics of fluid demixing in complex plasmas: Domain growth analysis using minkowski tensors. *Physical Review E*, 94(1):013201, 2016.

[205] K. Jiang, L. J. Hou, A. V. Ivlev, Y. F. Li, C. R. Du, H. M. Thomas, G. E. Morfill, and K. R. Sütterlin. Initial stages in phase separation of binary complex plasmas: Numerical experiments. *EPL (Europhysics Letters)*, 93(5):55001, 2011.

[206] Robert S. *Physics of Complex Plasmas: Some fundamental problems.* PhD thesis, Ludwig–Maximilians–University Munich, June 2010.

Publications

Oral and Poster Presentations at Conferences, Workshops and Seminars

A selection of further scientific contributions in various circumstances:

- B. Steinmüller and M. H. Thoma, "Komplexe Plasmen" (talk)
  Internal Seminar of the JLU-Giessen 2014

- B. Steinmüller, C. Dietz, M. Kretschmer and M. H. Thoma, "Druckabhängigkeit der Kristallisation eines komplexen Plasmas unter Laborbedingungen" (talk)
  DPG Spring Meeting, Bochum 2015

- B. Steinmüller, C. Dietz, M. Kretschmer and M. H. Thoma, "Pressure dependence for crystallization of an complex plasma under laboratory conditions" (poster)
  4th International Workshop on Diagnostic and Simulation of Dusty Plasmas, 2015

- B. Steinmüller, C. Dietz, M. Kretschmer and M. H. Thoma, "Pressure dependence for crystallization of a complex plasma under laboratory conditions" (poster)
  DPG Spring Meeting, Hannover 2016

- B. Steinmüller, C. Dietz, M. Kretschmer and M. Thoma, "Pressure dependence for crystallization of an complex plasma under laboratory conditions" (poster)
  DPG Spring Meeting, Bremen 2017

- B. Steinmüller, C. Dietz, L. Kleinschmidt, M. Kretschmer, T. Nimmerfroh, C. Schinz and M. H. Thoma, "Results of the 2016 parabolic flight Campaign in Bordeaux, France" (talk)
  Internal Seminar of the JLU-Giessen 2017

- B. Steinmüller, C. Dietz, M. Kretschmer and M. H. Thoma, "Crystallization of a three-dimensional complex plasma under laboratory conditions" (talk)
  8th International Conference on the Physics of Dusty Plasmas (8icpdp), Prague, Czech Republic, 2017

Publication List

The publications of the author are summarized here

- B. Steinmüller, C. Dietz, M. Kretschmer and M. H. Thoma, "Crystallization of a three-dimensional complex plasma under laboratory conditions" *Physics of Plasmas*, vol. 24, no. 3, p. 033705, 2017
  BS, CD and MK built up the experimental setup, recording of the data was done by BS. BS and CD were responsible for data analyzing (BS: pair correlation, non-spherical distribution, scalar product of the local bond order parameter, (also developing of) scalar product of the Minkowski structure metric; CD: bcc sensitive Minkowski structure metric). Data interpretation by all authors. BS wrote the manuscript, co-edited by all authors. MHT supervisor of the work.

- B. Steinmüller, C. Dietz, M. Kretschmer and M. H. Thoma, "Crystallization of a complex plasma under gravity conditions in dependence of pressure" *IEEE Transactions on Plasma Science*, 2017
  BS, CD and MK built up the experimental setup, recording of the data was done by BS. BS was responsible for data analyzing. Data interpretation by all authors. BS wrote the manuscript, co-edited by all authors. MHT supervisor of the work.

- B. Steinmüller, C. Dietz, M. Kretschmer and M. H. Thoma, "Crystallization process of a three-dimensional complex plasma", *Physical Review E* vol. 97 no. 5, p. 053202, 2018
  BS, CD and MK built up the experimental setup, recording of the data was done by BS. BS was responsible for data analyzing. Data interpretation mainly by BS. BS wrote the manuscript, co-edited by all authors. CD provided data with higher scanning speed for crosschecking (see footnote therein). MHT supervisor of the work.

- C. Dietz, M. Kretschmer, B. Steinmüller and M. H. Thoma, "Recent microgravity experiments with complex direct current plasmas", *Contribution to Plasma Physics* vol. 58, no. 1, p. 21-29, 2017
  BS, CD and MK responsible for the experimental setup, recording of the data was done by all authors. CD and BS were responsible for data analyzing (CD: electrorheology; BS: demixing). Data interpretation by all authors. All authors write the manuscript. MHT supervisor of the work.

- C. Dietz, R. Bergert, B. Steinmüller, M. Kretschmer, S. Mitic and M. H. Thoma, "Fcc-Bcc Phase Transition in Plasma Crystals using Time-Resolved Measurements" *Physical Review E* vol. 97, no 4, p. 043203, 2018
  CD, RB, BS and MK built up the experimental setup, recording of the data was done by CD and RB. CD and RB were responsible for data analyzing. CD wrote the manuscript, co-edited by all authors. MHT and SM supervisors of the work.

Copyright Notices

Crystallization of a three-dimensional complex plasma under laboratory conditions

B. Steinmüller, C. Dietz, M. Kretschmer, and M. H. Thoma

Crystallization of a three-dimensional complex plasma under laboratory conditions

B. Steinmüller,[a] C. Dietz, M. Kretschmer, and M. H. Thoma
Institute of Experimental Physics I, Justus Liebig University Giessen, Heinrich-Buff-Ring 16, 35392 Giessen, Germany

The influence of neutral gas pressure for crystallization of cylindrical complex plasmas under laboratory conditions is investigated. For the analysis of the complex plasma structure, different methods are adopted: First, the pair correlation and a criterion based on the shape of the Voronoi cells are applied. Besides this, a new implementation, which connects the Minkowski structure metric with the benefits from the scalar product of the local bond order parameter, is presented. In addition, the bcc sensitive Minkowski structure metric is used to identify the crystalline structures. All criteria display the same behavior: Decreasing the neutral pressure leads to crystallization. This is the opposite behavior to that observed in former ground based experiments. *Published by AIP Publishing.* [http://dx.doi.org/10.1063/1.4977902]

I. INTRODUCTION

By injecting solid particles with a typical size of a few micrometers into a low-temperature discharge plasma, the so-called complex plasma is created. Since electrons have a higher temperature than ions, the thermal electron flux on a non-charged particle is much greater than the ion flux. While a particle is charging more and more negatively, electrons are repulsed and ions are attracted. As soon as the ion flux and the electron flux balance each other out, the charge is in equilibrium.[1] Due to the screening of the plasma, the interaction of the particles with each other can be described by a Yukawa potential. Depending on the interaction strength between each other and their kinetic energy, the particles arrange in a solid-like or liquid-like structure.[2] Different phenomena are observed in a complex plasma like wave propagation,[3] particle growth,[4,5] formation of mach cones,[6] and many more. Fluid-solid phase transitions are of particular interest since the characteristic time and size range of the particle system allow to study melting and freezing at an individual particle level.[7]

A solid system (plasma crystal) is formed if the coupling parameter, i.e., the ratio of the interaction energy to the thermal energy of the particles

$$\Gamma = \frac{Q^2}{4\pi\epsilon_0\Delta k_B T_d}\exp(-\Delta/\lambda_D), \qquad (1)$$

becomes sufficiently large. Here, Q is the charge of particles, Δ the interparticle distance, and $k_B T_d$ the thermal energy of the particles. The Debye screening length in the bulk plasma, where the electron temperature T_e is much higher than the ion temperature T_i, is given by

$$\lambda_D \approx \sqrt{\frac{\epsilon_0 k_B T_i}{e^2 n_i}} \qquad (2)$$

with the ion density n_i being proportional to the gas pressure p. The critical value is estimated as $\Gamma = 172$ in the case of a one-component plasma with a pure Coulomb interaction.[8]

According to (1), melting can be induced by decreasing the particle charge Q, increasing the particle temperature T_d, increasing interparticle distance Δ, or decreasing the screening length λ_D. These quantities depend on the experiment control parameters, namely, gas pressure and type, electric power, particle size, and density in various ways. Most of the plasma crystal experiments have been done in compact capacitively coupled radio-frequency (RF) discharge chambers such as PK-3 Plus.[9]

Under microgravity on board the International Space Station (ISS), the influence of neutral gas pressure on the solid-fluid phase transition of a three dimensional complex plasma was investigated.[2,9] In these experiments, an increase in the neutral gas pressure led to larger interparticle distances (smaller particle density). At the same time, it was shown that the particle charge and screening length were approximately independent of the pressure. Although no statement on the pressure dependence of the particle temperature T_d was given, it was concluded that the increase in Δ with increasing pressure was the main responsible factor for melting.[2]

Under gravity, an electric field is necessary to suspend the particles. Since the electric field in the quasineutral bulk plasma is small, the levitation can be realized only in the plasma sheath, leading usually to plasma crystals with a limited extension in the vertical direction. This is in contrast to microgravity experiments where extended 3D systems can be studied. In experiments on ground, it is often observed that melting of a plasma crystal in the plasma sheath is caused by reducing the gas pressure, leading to a self-excited wave within the particle cloud.[10] This wave occurs below a certain pressure value where the mean free path and consequently also the velocity of the ions streaming to the plasma chamber walls become large enough to trigger a two-stream instability.[11,12] Therefore, in contrast to microgravity experiments,

---

[a]Electronic mail: Benjamin.Steinmueller@physik.uni-giessen.de

TABLE I. Examples of solid-fluid phase transitions in complex plasmas under gravity conditions.

Gas	RF power (W)	Particle size (μm)	Start of melting (Pa)	Completely disordered (Pa)
He[14]	12	$\approx$9.4	76	39
Kr[15]	0.8–2	9.6	$\approx$42	$\approx$23

plasma crystals under gravity conditions have been observed so far only at higher pressures. Another possibility of melting with decreasing pressure could be a lowering of friction of the particles in the background gas, resulting in a higher kinetic temperature T_d of the particles.[13] Two examples of solid-fluid phase transitions in complex plasmas on ground are given in Table I.

Spherical Yukawa clusters under gravity conditions have been studied in Refs. 16–20. Using a thermophoretic force, these clusters are levitated within the bulk plasma above the plasma sheath similar to our microparticle system. However, in contrast to the experiments discussed here, the number of particles in the cluster is much smaller, typically a few hundred, because of the horizontal confinement, e.g., by a glass box inserted into the chamber. Also, due to this spatial restriction, the structures differ from an extended 3d plasma crystal showing the arrangement of the microparticles in shell structures. At decreased pressure, the shell structure dissipates into a chainlike structure, forming an elongated cluster.[21]

In this paper, the crystallization of extensive three dimensional complex plasmas under gravity conditions depending on the neutral gas pressure is investigated. Here, plasmas with more than 10^4 particles and up to 30 layers perpendicular to the gravitation direction are analyzed. This is different from former studies of complex plasmas under gravity conditions, which consist of a single or only a few layers.[14,15,22–30] To eliminate other effects having an influence on the phase transition, the average distance and the particle density are kept constant while the pressure is manipulated. This is in distinction to the three dimensional complex plasmas investigated under microgravity conditions.[2,9]

The crystallization is examined by several criteria like the pair correlation and the nonspherical distribution.[31] To overcome some shortcomings of the local bond order parameter, Mickel *et al.*[32] recommended an implementation called the Minkowski structure metric (MSM). For this reason, we adopt the scalar product of the Minkowski structure metric (SPMSM), which is analogous to the known scalar product of the local bond order parameter (SPBOP).[33] The results of both implementations are compared. Furthermore, the bcc sensitive Minkowski structure metric (BSSMSM),[34] which gives an overview of the occurrence of different crystalline structures, is used.

II. EXPERIMENTAL SETUP AND PROCEDURES

The experiments are performed in a parallel-plate radio-frequency (RF) chamber with an electrode diameter of about 7.5 cm and a distance of 3 cm. This chamber was originally developed and used at the Max Planck Institute for Extraterrestrial Physics for investigating complex plasmas in

strong magnetic fields.[35] The discharges are operated in argon at pressures between 25 Pa and 45 Pa. A complex plasma is created by injecting monodisperse spherical particles made of Melamine - Formaldehyde (mass density, 1.51 g/cm^3) with a diameter of $d = 2.05\,\mu$m. The dispenser is localized at the side of the chamber. The electric field of the plasma sheath compensates gravity, allowing the small particles to levitate. The horizontal confinement of the microparticle cloud is caused by the finite horizontal extension of the plasma restricted to the volume between the electrodes due to the use of a guard ring in the rf discharge chamber.

For particle observation, a horizontal expanded sheet of a laser diode is used. The scattered light from the particles is recorded by a CMOS camera with a resolution of 15.6 μm/pixel. It is mounted perpendicular to the laser sheet. The upper electrode consisting of glass coated with indium tin oxide (ITO) allows the camera to be mounted on top of the chamber. The amplitude of the voltage of the electrodes is set independently from each other. In order to determine the three dimensional positions of the particles, the laser and the camera are moved perpendicular to the field of view, recording images every 10 μm. A volume of about $6 \times 6 \times 6$ mm^3 is analyzed. This volume is located about 4.5 mm above the center of the lower electrode outside the plasma sheath. Figure 1 shows a sketch of the experimental setup.

To keep the particle number between two scans at different pressures approximately constant ($\approx 15 \times 10^3$ particles within the observed volume), the pressure is varied by only small gas flows. The small gas fluxes allow to maintain the structure of the particle arrangement. To observe the phase changes, the crystallization at every new pressure level should be unaffected from the former conditions. For this reason, the particle arrangement has to be disturbed for a short duration, which could be realized, e.g., by lasers[28] or by a strong increase in RF power.[14] Here, the RF power at 13.56 MHz is increased for a few seconds to a high level, before it returns
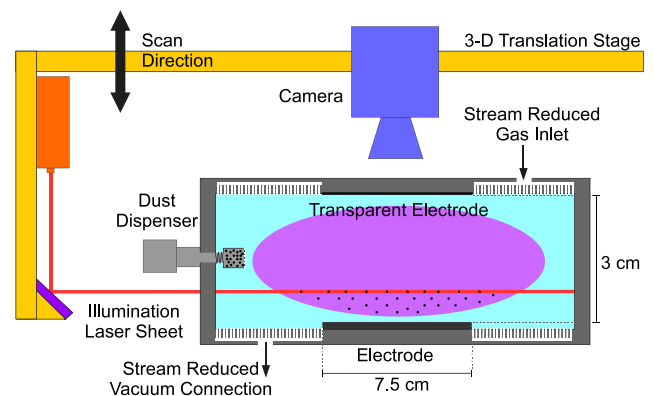

FIG. 1. Sketch of the experimental setup.

back to a low level, where the measurements are taken. At high power, the peak-to-peak voltage is 52 V at the lower electrode and 92 V at the upper electrode. Increasing the RF power to that high level results in an entire disorder of the particle system. At low power, the peak-to-peak voltage is 15 V at the lower and 35 V at the upper electrode. In both cases, the phase difference between both electrodes is π so that the maximum electric field is generated.

To refresh the gas, a flux of about 0.15 sccm for 5 min is applied. In the next 5 min before scanning, the flow is switched off, so that the particles are undisturbed. In order to get statistical results, five independent measurement series are performed. Therefore, between two measurements, the chamber is evacuated, and then fresh gas is used to ignite the plasma and new particles are injected. This means that the particle number changes between the series of measurements; however, the amount of particles in a series remains constant.

In contrast to former ground experiments, a rather large homogeneous particle cloud consisting of small particles and extending into the bulk plasma could be created at low RF power, reducing the formation of a two-stream instability at low pressures. Besides this, in the plasma sheath where the ions are accelerated by the electric field, the ion-focus effect causes a wake potential between the microparticles, leading to the formation of vertical strings.[21] In the bulk plasma, however, the ion-focus effect can be neglected, as it can be seen in microgravity experiments.[2,9] In addition, keeping the particle number constant at different pressures within one experiment series allowed to observe changes in the phase structure under controlled conditions.

III. CRITERIA OF PHASE TRANSITIONS

To investigate the phase transition between liquid and solid states, various criteria have been developed. To determine the phase transition in a complex plasma in this work, some of the well-known and newly developed criteria are described and applied.

A. Pair correlation

For the pair correlation, the distances to the nearest neighbors of particles are plotted in a histogram. For a system with N particles and a particle density ρ, the pair correlation function is given by

$$g(r) = \frac{1}{\rho N} \left\langle \sum_{i}^{N} \sum_{j \neq i}^{N} \delta(\mathbf{r} - \mathbf{r}_{ij}) \right\rangle. \qquad (3)$$

The connecting vector of particles i and j is given by $\mathbf{r}_{ij}$. In a crystal, where the positions of the particles are arranged periodically and symmetrically, the pair correlation function has distinct maxima and minima. In short-range systems like liquids, the peaks disperse.[36,37]

The ratio of the first nonvanishing minimum and the first maximum of the pair correlation function

$$R = \frac{\min(g(r))}{\max(g(r))} \qquad (4)$$

has been proposed by Raveché, Mountain, and Streett as a crystallization criterion. Lennard-Jones systems are in the solid state if $R < 0.2 \pm 0.02$.[38] The exact value of this ratio at phase transition may depend on the specific shape of the interacting potential.[39] Nevertheless, the Raveché-Mountain-Streett criterion is a good indicator for qualitative comparison of crystallization in all kinds of particle clouds, independent of their interaction potential.

A disadvantage of this method is that it does not perform well with inhomogeneous structures, e.g., if the interparticle distances vary over the observed region. In such a case, the fraction R increases, even if the system is highly ordered. To demonstrate the effect of inhomogeneity, a face centered cubic (fcc) crystal structure consisting of 62,500 particles with lattice constant a of one is artificially generated. With respect to gravity, the z-axis is distorted by an exponential term, while the x- and y- coordinates of the particles remain unchanged. The distortion factor is given by $\exp(-1 + z/h)$, z is the primary z-coordinate of the particle, while h corresponds to the z-dimension of the crystal, which is 24.5. This means that a particle whose origin position is $[24, 24, 24]$ is shifted to $[24, 24, 24 \cdot \exp(24/24.5 - 1)] \approx [24, 24, 23.5]$. The advantage of this distortion is that the borders of the crystal keep unaltered. In addition, for considering Brownian motion, the original coordinates and the distorted ones are overlain by a normal distribution with a standard deviation of $0.05\,a$ (a is the lattice constant). Figure 2 shows the pair correlations of the undistorted and the distorted coordinates. R is increased from 0.11 (undistorted fcc) to 0.39 (distorted fcc), following the Raveché-Mountain-Streett criterion a phase transition takes place due to the distortion.

B. Nonspherical distribution

Voronoi cells are frequently used to investigate the regions of solid and liquid phases in two dimensional complex plasmas.[14,29,40] If the number of Voronoi neighbors diverges from six in such a system, the lattice is disturbed. Based on the occurrence of the perturbations, the particle cloud can be determined as being in the liquid or (if only few perturbations exist) as being in the solid state.
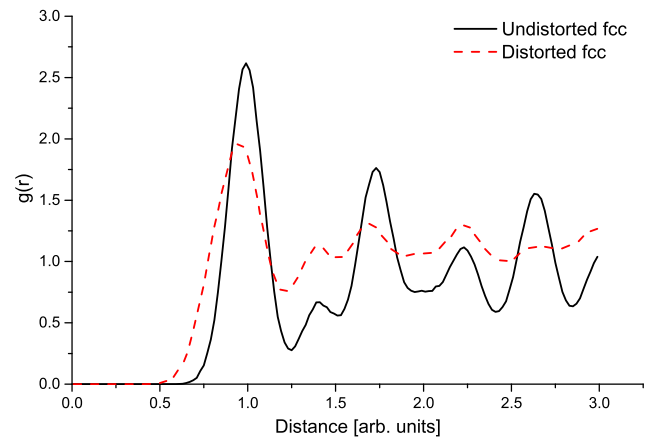

FIG. 2. The pair correlation of fcc clusters, undistorted (solid line) and distorted (dotted line), by a factor of $\exp(z/\text{height} - 1)$, each superimposed by a Gaussian noise of $0.05\,a$ (a is the lattice constant).

Since already small displacements of the particle positions vary the number of the polyhedron facets, the absolute number of Voronoi neighbors in fcc and hcp (hexagonal closed packed) crystals fluctuates strongly.[41] This is why in three dimensions, the amount of facets cannot be used as a criterion for phase transition. Therefore, Montoro and Abascal introduced the nonsphericity, anisotropy factor α, which describes the geometric characteristics of Voronoi cells or, in other words, how close the Voronoi cell is to a perfect sphere.[31] This method was never used before to analyze a complex plasma. The nonsphericity factor is proportional to the product of the average curvature radius R_c for a Voronoi cell, and its surface S divided by its volume V

$$\alpha = \frac{R_c S}{3V}. \tag{5}$$

Obviously, α is unity ($\alpha = 1$) for spheres and increases for nonspherical convex shapes. The length of two intersecting facets is l_i and the angle between their normal vectors, which are oriented towards the outside, is described by ϕ_i (in units of radian). For polyhedrons, the average curvature radius is given by

$$R_c = \frac{1}{8\pi} \sum_i^{edges} l_i \phi_i. \tag{6}$$

To use the anisotropic factor to determine the phase state, α is calculated for each particle and plotted in a histogram. Since the positions of the Voronoi neighbors are highly symmetric in a non-disturbed crystalline structure, the distribution of the anisotropic factor is very narrow. Table II shows the values for α in different structures. In crystalline structures, except for simple cubic (sc), the anisotropic factor α is below 1.25. At melting, the Voronoi cells become more irregular, which has two effects: The distribution of the anisotropic factor disperses and the polyhedra are in general less spherical-like, which increases the value for α.

C. Scalar product of the local bond order parameter

The pair correlation and the Voronoi anisotropic factor are global criteria for phase transitions. To get a local insight into the structure, the scalar product of the local bond order parameter (SPBOP) is used to identify if each individual particle is in the solid or in the liquid state. The bond order parameter q_{lm} with N neighbors can be written as[42]

$$q_{lm}(\mathbf{r}_i) = \frac{1}{N} \sum_{j=1}^{N} Y_{lm}\big(\theta(\mathbf{r}_{ij}), \phi(\mathbf{r}_{ij})\big). \tag{7}$$

TABLE II. Values of the anisotropic factor α for different structures.[31]

	α_{bcc}	α_{fcc}	α_{hcp}	α_{liq}	α_{gas}	α_{sc}
Value	1.18	1.22	1.22	$\approx$1.31	1.42	1.50

$\theta(\mathbf{r}_{ij})$ and $\phi(\mathbf{r}_{ij})$ are the respective angles of spherical coordinates, from which the spherical harmonics Y_{lm} are calculated (for details about the spherical harmonics, see appendix). An algorithm is used to find the twelve nearest neighbors. With $l = 6$, the bond order parameter is sensitive to distinguish between crystalline and liquid structures. q_{6m} is normalized by

$$\tilde{q}_{6m}(i) = \frac{q_{6m}}{\left(\sum_{m=-6}^{6} |q_{6m}(i)|^2\right)^{1/2}}. \tag{8}$$

Since crystals are arranged periodically, the bond order parameter adds up coherently in crystals and incoherently in liquids[33]

$$S_{ij} = \sum_{m=-6}^{6} \tilde{q}_{6m}(i) \cdot \tilde{q}_{6m}^*(j). \tag{9}$$

The asterisks denote complex conjugation. Due to the normalization to unity, the bond order parameter S_{ij} is 1 in a perfect crystal, where the connection vectors of the particles are symmetric. In the slightly disturbed position data of real particles (e.g., stressed by gravity), this value decreases. For this reason, a specific threshold is introduced. If the product of the bond order parameter exceeds this threshold, two particles are defined as connected. Often, a value of 0.5 is applied.[33,43,44] To make the criterion more sensitive in this work, 0.75 is used.

However, two particles can still be connected in a system that is in the liquid state even using this higher threshold. Therefore, a particle is only identified as being in the solid state if it is connected to at least eight of its twelve nearest neighbors. In the case of few connections to its neighbors, a particle is defined as being in the liquid state.[33,43,44]

D. Scalar product of the Minkowski structure metric

Recent investigation of local bond order parameters from Mickel *et al.*[32] has shown problematic behavior of the bond-orientational order parameter q_6. The parameter is not robust because it tends to change erratically. This is due to the fact that the bond order parameters are not a continuous function of the neighborhood. Also, the definition of a neighborhood is ambiguous, and there are many different ways to calculate the neighbors (e.g., Voronoi neighbors,[45] cutoff-radius,[42] or k-nearest neighbor search[46]). Thus, Mickel *et al.* proposed a new definition of local structure metric parameters, which is called the Minkowski structure metric, defined by

$$q_l'(i) = \sqrt{\frac{4\pi}{2l+1} \sum_{m=-l}^{l} \left| \sum_{f \in \mathcal{F}(i)} \frac{A(f)}{A} Y_{lm}(\theta_f, \phi_f) \right|^2}. \tag{10}$$

The new parameter q_l' is now weighted by the facet areas of the respective Voronoi facet $A(f)$, with

$$A = \sum_{f \in \mathcal{F}(i)} A(f). \tag{11}$$

Also, the spherical angles are now determined with respect to the normal vectors of facet f. $\mathcal{F}(i)$ is the Voronoi cell boundary around particle i. With this slight modification, the Minkowski structure metric is a more robust and continuous structure parameter. The problem of different definitions of neighborhood has also been solved.

We propose to use the scalar product of the Minkowski structure metric (SPMSM) to apply the advantages of the continuous Minkowski structure parameter to the SPBOP. Now, the order parameters are defined with respect to the Minkowski structure metric

$$q'_{lm}(i) = \sum_{f \epsilon \mathcal{F}(i)} \frac{A(f)}{A} Y_{lm}(\theta_f, \phi_f). \tag{12}$$

This metric has the same characteristics as the local bond order parameters. For $l = 6$, it sums up coherently in crystals and incoherently in liquids. After normalization (see (8)), a criterion for a scalar product is developed.

$$S'_{ij} = \sum_{m=-6}^{6} \tilde{q}'_{6m}(i) \cdot \tilde{q}'^{*}_{6m}(j). \tag{13}$$

If the product exceeds 0.75, a pair of Voronoi neighboring particles is defined as connected. Particles with eight or more connected neighbors are identified as being in the solid, otherwise as being in the liquid state.

E. BCC sensitive Minkowski structure metric

To get a deeper insight into the individual crystal structures, a modified version of the bond order parameter with the improved Minkowski structure metric (MSM)[32] is used. The main feature of the method is that it allows to distinguish between fcc, hcp, and bcc (body centered cubic) crystal structures in data with mixed crystalline phases. Accordingly, this method is called the "bcc sensitive Minkowski structure metric" or short BCCMSM.[34] Since the parameters q_4 and q_6 (see Equation (10)), which are calculated for every particle i, have unique values for certain crystal structures, it is possible to assign different crystal structures (see Table III).

In the case of bcc, it is useful to calculate a ratio between the first and second shell facet areas using the mean areas A_{1st} and A_{2nd}

TABLE III. Values of the bcc sensitive Minkowski structure metric q_l for the most relevant crystal structures: the values are calculated for perfect lattices.[32]

	fcc	hcp	bcc
$\tilde{q}_2$	0	0	0
$\tilde{q}_3$	0	0.076	0
$\tilde{q}_4$	0.190	0.097	0.509
$\tilde{q}_5$	0	0.252	0
$\tilde{q}_6$	0.575	0.484	0.629

$$z = \frac{A_{1st}}{A_{2nd}} = \frac{3}{4} \frac{\sum_{i=1}^{8} A_{fi}}{\sum_{j=9}^{14} A_{fj}}. \tag{14}$$

For a descending sorted list of facet areas $\tilde{A} = (A_{f1}, A_{f2}, \ldots, A_{fN})$, it is possible to calculate z_{bcc} using the first eight entries as first shell neighbors and the next six entries as second shell neighbors, which results in $z_{bcc} = \frac{3}{2}\sqrt{3}$. Calculating z for fcc and hcp will result in $z_{fcc} = z_{hcp} = 1$. Now, a weighting function $h[A(f)]$ can be defined as

$$h[A(f)] = \left\{ \exp\left[-3A \frac{(A(f) - \bar{A})}{\bar{A}^2} g(z) \right] + 1 \right\}^{-1}, \tag{15}$$

$$g(z) = \exp\left[-\frac{9}{2}(z - z_{bcc})^2 \right] \tag{16}$$

with A given in (11) and $\bar{A} = \langle A \rangle$. This weighting function will suppress any second shell neighbors in the case of bcc to allow a better distinction between fcc and hcp. The result for fcc or hcp-like structures remains untouched. The new parameter is now defined as follows:

$$\tilde{q}_l(i) = \sqrt{\frac{4\pi}{2l+1} \sum_{m=-l}^{l} \left| \sum_{f \in \mathcal{F}(i)} \frac{h[A(f)]}{H} Y_{lm}(\theta_f, \phi_f) \right|^2}. \tag{17}$$

The divisor H is the sum over all possible $h[A(f)]$.[34]

IV. RESULTS

A. Pair correlation

To determine the phase state of the system, the pair correlation function is applied. Figure 3 shows the ratio of its first minimum to its first maximum (4). At low pressures, the ratio is low, indicating a highly ordered complex plasma. Increasing
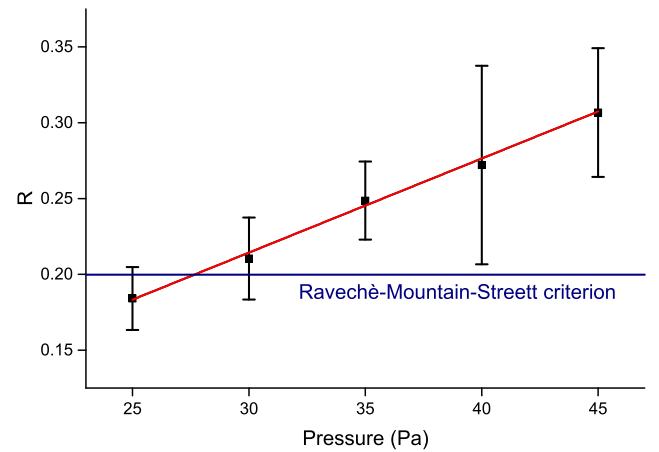

FIG. 3. The ratio R of the first minimum to the first maximum of the pair correlation. The standard deviation of the five independent measurements is given by the errorbars.

the pressure leads to an increased value, which means that, following the Raveché-Mountain-Streett criterion, the particles are in the liquid state. Even in the crystalline state, the arrangement of the particles is not very homogeneous. Owing to gravity, the interparticle distances are smaller in the lower part of a complex plasma than in the upper part. It is shown that the global pair correlation of a system with varying interparticle distances has dispersed minima and maxima (see Figure 2). Since this heterogeneous structure occurs in a complex plasma, the ratio R (4) is high. Nevertheless, the Raveché-Mountain-Streett criterion, which is valid for Lennard-Jones systems, indicates that the phase transition takes place at about 28 Pa. However, as discussed in Section III A, the actual value for the pressure of the phase transition could be higher since distortions of the lattice might increase R.

B. Nonspherical distribution

For $p > 28$ Pa, it is not clear whether the particle systems are completely disordered or the high value of R is caused by the unequal interparticle distances. To get a deeper insight into the phase transitions, a more local criterion is used. For the nonspehrical distribution, the value α (5) for each particle is plotted in a histogram. To make sure that each measurement is weighted equally (independent of the particle number), the distribution is area normalized. Figure 4 shows the average of the measurements at identical pressure.

At 25 Pa, the maximum of the distribution is at $\alpha = 1.22$, indicating that all particles are in the solid state (see Table II). At increased pressure, the distribution disperses, indicating a superposition of particles in the solid and in the liquid state. At 45 Pa, no distinguished peak is recognizable at the predicted value for solid phases. Besides this, the distribution is broadened, also indicting that the particles are in the liquid phase. The reason why the maximum is not localized where it is proposed to be for liquids ($\alpha \approx 1.3$, Table II) is still to be investigated.

C. SPMSM and SPBOP

In Figure 5, the results of the SPBOP and of the SPMSM are given. Here, the normalized fraction of particles that are connected to at least eight neighbors (i.e., being in
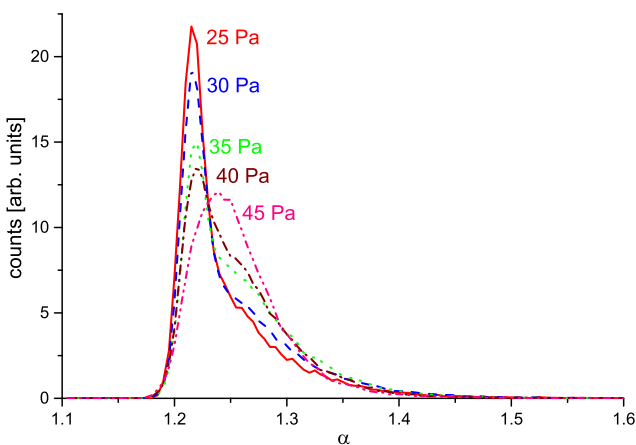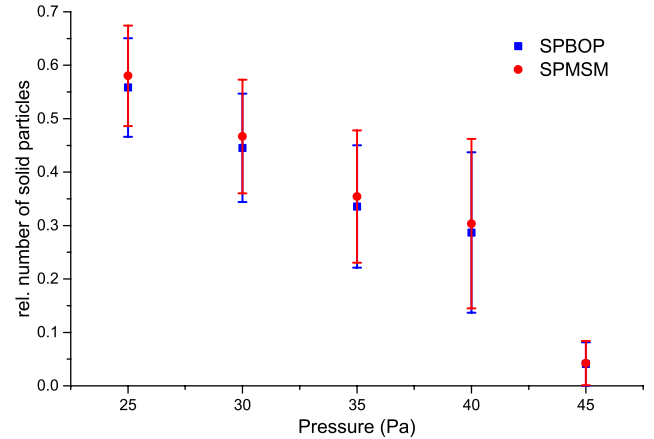

FIG. 5. The relative number of particles being in the solid state (particles which are connected with at least eight neighbors, whereas two particles are defined as connected if $S_{ij} > 0.75$ or $S'_{ij} > 0.75$) based on the scalar product of the local bond order parameter *SPBOP* and of the Minkowski structure metric *SPMSM*. The error bars indicate the standard deviation.

the solid state) is shown. At high pressure, the fraction is lower than at low pressure. This indicates melting of the dust cloud at decreased pressure. It can be seen that the fraction of particles being in the solid state is higher for SPMSM than for SPBOB. This may be due to the improved definition of neighborhood. Nevertheless, the differences between both scalar products are small. Between domains of highly ordered particles being in the solid state, a region with no or only small order exists. Particles in this transition region are connected to less than eight neighbors and are accordingly classified as being in the fluid state.

At increased neutral gas pressure, the crystallization starts at the bottom of the analyzed volume but does not proceed to the upper part. This is in accordance with Zuzic *et al.*,[40] who already reported, that complex plasmas under gravity conditions are highly ordered at bottom, while upper layers are more disordered.

D. BCCMSM

Since the already applied criteria distinguish only between solid and liquid states, the BCCMSM is used to retrieve information about the structural composition. It was possible to find fcc, hcp, and bcc structures using the $\tilde{q}_4$ and $\tilde{q}_6$ (Figure 6). At 25 Pa, the diagram shows high density in the upper half, which confirms that the whole particle clouds are in the solid state (Table III). The dominant part of particles in the solid state forms fcc and bcc structures. At increased pressure, the amount of particles being in the solid state decreases, while the amount of particles being in the liquid state increases.

E. Overview and particle number

From Table IV, it can be seen that the results of all applied criteria are in good agreement with each other. A continuous phase transition between 25 Pa, where nearly all particles are in the solid state, and 45 Pa, where all particles are in the liquid state (see also Figure 3), is observed.
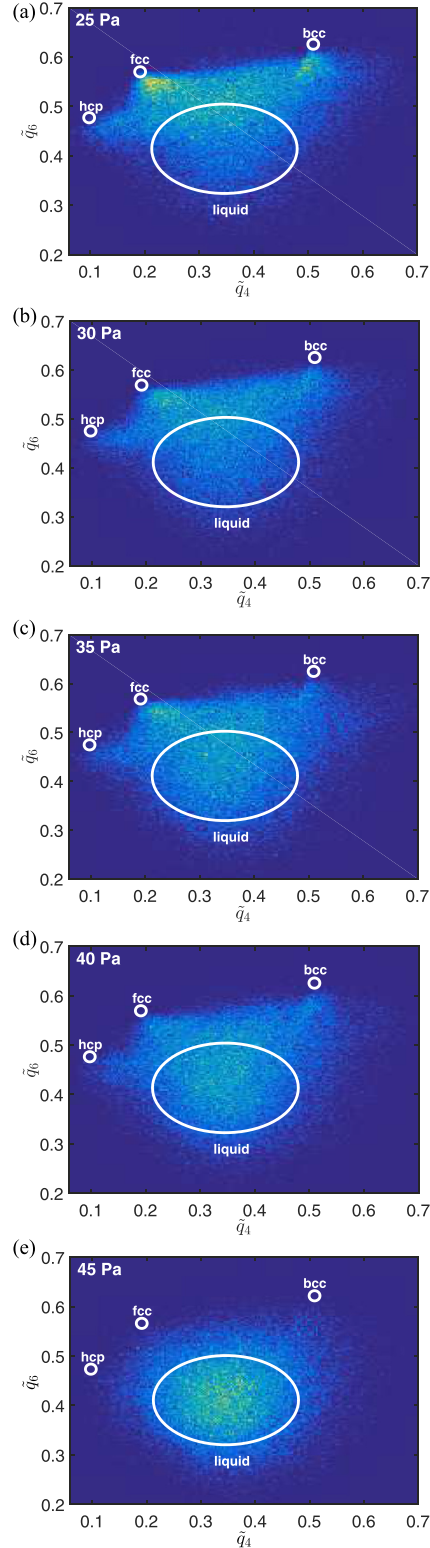

FIG. 4. The nonspherical distribution α (area normalized).

FIG. 6. Two dimensional histogram showing $\tilde{q}_4$ and $\tilde{q}_6$ at different pressures. The diagram is accumulated over all measurements according to the pressure. Yellow (light) areas mark high particle density, while blue (dark) regions have low density.

TABLE IV. Estimation of the melting behavior of the complex plasma based on different criteria.

	Melting (Pa)
Pair correlation[a]	∼28
Nonspherical distribution	25–45
SPBOP[b]	25–45
SPMSM[c]	25–45
BCCMSM[d]	25–45

[a]Following the Raveché-Mountain-Streett criterion; $R = 0.2$ (Ref. [38]) (made for Lennard-Jones systems).
[b]Scalar product of the local bond order parameter.
[c]Scalar product of the Minkowski structure metric.
[d]bcc sensitive Minkowski structure metric.

particles were exchanged. Figure 7 shows the density and average interparticle distances. Since it is not possible in this setup to inject the same amount of particles into the discharge, the error bars of the density and the nearest neighbor distance are large.

V. DISCUSSION

In the present experiments, crystallization at low pressures was observed with a gradual melting with increasing pressure (see Table IV). Former ground based experiments showed the opposite behavior where the particles were in the solid state at higher pressure and in the liquid state at lower pressure[14,15,22] (see Table I).

To explain this different behavior, the changing of the coupling parameter (1) under neutral gas pressure manipulation is considered. Increasing the number density of neutral gas atoms by increasing the pressure raises the probability of collisions between the plasma particles. Collisions of ions with neutrals transfer energy and angular momentum, especially when charge is exchanged. A positive ion that lost its kinetic energy in the vicinity of a negatively charged particle has a lower probability to escape its attractive potential. Therefore, at increased pressure, the higher ion flow to the particle reduces its negative charge.[47] The orbit motion limited (OML) theory is often used to describe the charging of particles in a complex plasma.[1] This theory is derived by energy and angular momentum conservation of the ions in the vicinity of a particle and neglects the ion-neutral collisions. If the Debye length is much smaller than the mean free path of neutrals and ions, the OML is a good approximation. But even at low pressures ($\lesssim$25 Pa), it overestimates the charge of a particle significantly.[48]

An effect that should also be taken into account is the smaller Debye length at increased pressure ($\lambda_D \propto n_i^{-0.5} \propto p^{-0.5}$).

The decreased particle charge and the increased Debye length (while the interparticle distance was held constant) decrease the coupling parameter (1). This reduced coupling parameter explains the observed melting of the particle cloud at low pressure, assuming a constant dust temperature T_d and interparticle distance Δ. The latter is realized in our experiments (see Figure 7).
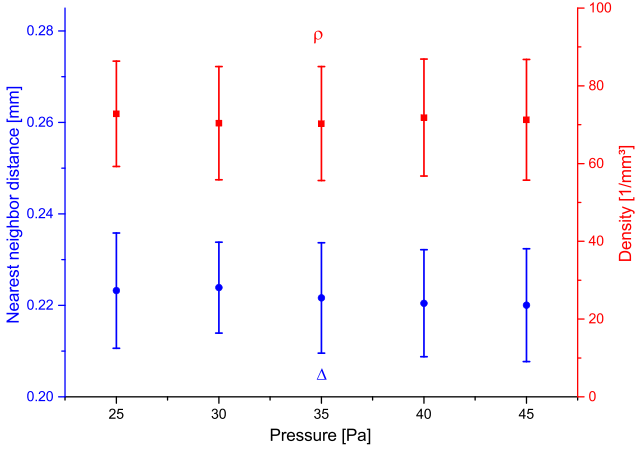
To verify that the crystallization is only an effect of varying the neutral gas pressure, the particle number has been kept constant during pressure manipulation. Between the five independent measurement series, the gas and the

FIG. 7. Density ρ and nearest neighbor distances Δ of the particles. The standard deviation is given by the errorbars.

The opposite observations in former ground experiments may originate from different positions of the dust cloud in the plasma. Under gravity conditions, the crystalline state in a complex plasma was examined mainly in systems, where the particles were arranged in one or in only a few layers.[14,15,22] Due to gravity, all particles in former experiments were located in or close to the plasma sheath. In the present work, the complex plasma consists of up to thirty layers of small particles with about $15 \cdot 10^3$ particles in the examined region, which is clearly above the plasma sheath in the bulk plasma. Besides this, the upper layers exert pressure on the lower ones, which compresses them. So, the inner pressure of dust particles explains the smaller interparticle distances in the lower part of the complex plasma. The high vertical extension of the particle cloud increases the coupling parameter (1) of the lower layers. Furthermore, a small RF power leading to a weak electric field in the sheath[49] is sufficient to levitate the small particles and reduces the formation of a two-steam instability at low pressures, which leads to melting.[2,11,12]

Our observation is similar to microgravity experiments onboard the ISS,[2] where the solid state was observed at lower pressures and the liquid state at higher pressures. However, the reason is different: In the microgravity experiments, the melting is caused by an increase in the interparticle distance with increasing pressure at constant particle charge and screening length, whereas in our experiments, the interparticle distance was kept constant, the but particle charge and screening length decreased.

VI. CONCLUSIONS

The neutral gas pressure of complex plasmas under gravity conditions is varied in a range of $25\,\text{Pa}$–$45\,\text{Pa}$. Different crystallization criteria are applied: the pair correlation and the nonspherical distribution. The scalar product of the local bond order parameter is improved to the scalar product of the Minkowski structure metric. Both methods are successfully applied and compared. The composition of different crystalline structures is analyzed by the bcc sensitive Minkowski structure metric. All deployed criteria are in

agreement: Under laboratory conditions, the three dimensional particle cloud is in the solid state at low pressure and in the liquid state at high pressure. There is no hint for a sharp transition between these two states. The particle density and the interparticle distances are kept constant during pressure manipulation. So, the phase state of the system is dominated by neutral pressure. This behavior is explained by the decreasing coupling parameter. This is due to the reduced charge of the microparticles based on collisions of ions in their vicinity and an increased Debye length.

In comparison with former experiments under gravity and under microgravity conditions, we find two factors that might be important for the behavior of complex plasmas as investigated here: the extension of the particle cloud and the strength of the electric fields that levitates the particles.

APPENDIX: SPHERICAL HARMONICS

The spherical harmonics are defined as

$$Y_{lm}(\theta, \phi) = \frac{1}{\sqrt{2\pi}} N_{lm} P_{lm}(\cos\theta) e^{im\phi} \qquad \text{(A1)}$$

with

$$P_{lm}(x) = \frac{(-1)^m}{2^l l!} (1 - x^2)^{m/2} \frac{d^{l+m}}{dx^{l+m}} (x^2 - 1)^l \qquad \text{(A2)}$$

and

$$N_{lm} = \sqrt{(l + 0.5) \cdot \frac{(l - m)!}{(l + m)!}} \qquad \text{(A3)}$$

Here, θ is the polar angle and ϕ the azimuthal angle of the connection vector between two neighboring points, see Figure 8. $r = (x, y, z)$ is the vector from the particle to its neighbor, and both the angles are given by (analog to the spherical coordinate system) $\phi = \text{atan2}(y, x)$ and $\theta = \arccos\left(z/\sqrt{x^2 + y^2 + z^2}\right)$.
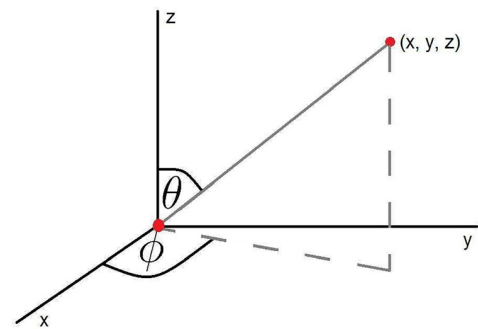

FIG. 8. The polar angle θ and the azimuthal angle ϕ for the connection between two particles.

[1] J. E. Allen, "Probe theory-the orbital motion approach," Phys. Scr. **45**, 497 (1992).

[2] S. A. Khrapak, B. A. Klumov, P. Huber, V. I. Molotkov, A. M. Lipaev, V. N. Naumkin, A. V. Ivlev, H. M. Thomas, M. Schwabe, G. E. Morfill, V. E. Petrov, V. E. Fortov, Y. Malentschenko, and S. Volkov, "Fluid-solid phase transitions in three-dimensional complex plasmas under microgravity conditions," Phys. Rev. E **85**, 066407 (2012).

[3] R. L. Merlino, "Dust-acoustic waves driven by an ion-dust streaming instability in laboratory discharge dusty plasma experiments," Physics of Plasmas (1994–present) **16**, 124501 (2009).

[4] B. Tadsen, F. Greiner, and A. Piel, "Preparation of magnetized nanodusty plasmas in a radio frequency-driven parallel-plate reactor," Phys. Plasmas (1994–present) **21**, 103704 (2014).

[5] L. Wörner, E. Kovacevic, J. Berndt, H. M. Thomas, M. H. Thoma, L. Boufendi, and G. E. Morfill, "The formation and transport phenomena of nanometre-sized particles in a dc plasma," New J. Phys. **14**, 023024 (2012).

[6] M. Schwabe, K. Jiang, S. Zhdanov, T. Hagl, P. Huber, A. V. Ivlev, A. M. Lipaev, V. I. Molotkov, V. N. Naumkin, K. R. Sütterlin, H. M. Thomas, V. E. Fortov, G. E. Morfill, A. Skvortsov, and S. Volkov, "Direct measurement of the speed of sound in a complex plasma under microgravity conditions," Europhys. Lett. **96**, 55001 (2011).

[7] V. E. Fortov, A. V. Ivlev, S. A. Khrapak, A. G. Khrapak, and G. E. Morfill, "Complex (dusty) plasmas: Current status, open issues, perspectives," Phys. Rep. **421**, 1–103 (2005).

[8] S. Ichimaru, "Strongly coupled plasmas: high-density classical plasmas and degenerate electron liquids," Rev. Mod. Phys. **54**, 1017 (1982).

[9] V. I. Molotkov, H. M. Thomas, A. M. Lipaev, V. N. Naumkin, A. V. Ivlev, and S. A. Khrapak, "Complex (dusty) plasma research under microgravity conditions: Pk-3 plus laboratory on the international space station," Int. J. Microgravity Sci. Appl. **35**, 320302 (2015).

[10] M. H. Thoma, M. Kretschmer, H. Rothermel, H. M. Thomas, and G. E. Morfill, "The plasma crystal," Am. J. Phys. **73**, 420–424 (2005).

[11] G. Ganguli, G. Joyce, and M. Lampe, "Phase transition in dusty plasmas: A microphysical description," AIP Conf. Proc. **649**, 157–161 (2002).

[12] G. Joyce, M. Lampe, and G. Ganguli, "Instability-triggered phase transition to a dusty-plasma condensate," Phys. Rev. Lett. **88**, 095006 (2002).

[13] V. A. Schweigert, I. V. Schweigert, A. Melzer, A. Homann, and A. Piel, "Alignment and instability of dust crystals in plasmas," Phys. Rev. E **54**, 4155 (1996).

[14] A. Melzer, A. Homann, and A. Piel, "Experimental investigation of the melting transition of the plasma crystal," Phys. Rev. E **53**, 2757 (1996).

[15] H. M. Thomas and G. E. Morfill, "Melting dynamics of a plasma crystal," Nature **379**(6568), 806 (1996).

[16] A. Piel, "Plasma crystals-structure and dynamics," Plasma Fusion Res. **4**, 013 (2009).

[17] H. Thomsen and M. Bonitz, "Resolving structural transitions in spherical dust clusters," Phys. Rev. E **91**, 043104 (2015).

[18] H. Baumgartner, H. Kählert, V. Golobnychiy, C. Henning, S. Käding, A. Melzer, and M. Bonitz, "Shell structure of yukawa balls," Contrib. Plasma Phys. **47**, 281–290 (2007).

[19] D. Block, M. Kroll, O. Arp, A. Piel, S. Käding, Y. Ivanov, A. Melzer, C. Henning, H. Baumgartner, P. Ludwig, and M. Bonitz, "Structural and dynamical properties of yukawa balls," Plasma Phys. Controlled Fusion **49**, B109 (2007).

[20] A. Schella, T. Miksch, A. Melzer, J. Schablinski, D. Block, A. Piel, H. Thomsen, P. Ludwig, and M. Bonitz, "Melting scenarios for three-dimensional dusty plasma clusters," Phys. Rev. E **84**, 056402 (2011).

[21] C. Killer, A. Schella, T. Miksch, and A. Melzer, "Vertically elongated three-dimensional yukawa clusters in dusty plasmas," Phys. Rev. B **84**, 054104 (2011).

[22] Y. Ivanov and A. Melzer, "Melting dynamics of finite clusters in dusty plasmas," Phys. Plasmas (1994–present) **12**, 072110 (2005).

[23] C. A. Knapek, A. V. Ivlev, B. A. Klumov, G. E. Morfill, and D. Samsonov, "Kinetic characterization of strongly coupled systems," Phys. Rev. Lett. **98**, 015001 (2007).

[24] S. Nunomura, S. Zhdanov, D. Samsonov, and G. Morfill, "Wave spectra in solid and liquid complex (dusty) plasmas," Phys. Rev. Lett. **94**, 045001 (2005).

[25] S. Nunomura, D. Samsonov, S. Zhdanov, and G. Morfill, "Self-diffusion in a liquid complex plasma," Phys. Rev. Lett. **96**, 015003 (2006).

[26] V. Nosenko, J. Goree, Z. W. Ma, and A. Piel, "Observation of shear-wave mach cones in a 2d dusty-plasma crystal," Phys. Rev. Lett. **88**, 135001 (2002).

[27] V. Nosenko, S. Zhdanov, A. Ivlev, G. Morfill, J. Goree, and A. Piel, "Heat transport in a two-dimensional complex (dusty) plasma at melting conditions," Phys. Rev. Lett. **100**, 025003 (2008).

[28] V. Nosenko, J. Goree, and A. Piel, "Laser method of heating monolayer dusty plasmas," Phys. Plasmas (1994–present) **13**, 032106 (2006).

[29] V. Nosenko, S. K. Zhdanov, A. V. Ivlev, C. A. Knapek, and G. E. Morfill, "2d melting of plasma crystals: Equilibrium and nonequilibrium regimes," Phys. Rev. Lett. **103**, 015001 (2009).

[30] S. Ratynskaia, K. Rypdal, C. Knapek, S. Khrapak, A. V. Milovanov, A. Ivlev, J. J. Rasmussen, and G. Morfill, "Superdiffusion and viscoelastic vortex flows in a two-dimensional complex plasma," Phys. Rev. Lett. **96**, 105010 (2006).

[31] J. C. G. Montoro and J. L. F. Abascal, "The voronoi polyhedra as tools for structure determination in simple disordered systems," J. Phys. Chem. **97**, 4211–4215 (1993).

[32] W. Mickel, S. C. Kapfer, G. E. Schröder-Turk, and K. Mecke, "Shortcomings of the bond orientational order parameters for the analysis of disordered particulate matter," J. Chem. Phys. **138**, 044501 (2013).

[33] P. R. ten Wolde, M. J. Ruiz-Montero, and D. Frenkel, "Numerical calculation of the rate of crystal nucleation in a lennard-jones system at moderate undercooling," J. Chem. Phys. **104**, 9932–9947 (1996).

[34] C. Dietz and M. H. Thoma, "Investigation and improvement of three-dimensional plasma crystal analysis," Phys. Rev. E **94**, 033207 (2016).

[35] M. Schwabe, U. Konopka, P. Bandyopadhyay, and G. E. Morfill, "Pattern formation in a complex plasma in high magnetic fields," Phys. Rev. Lett. **106**, 215004 (2011).

[36] B. A. Klumov, "On melting criteria for complex plasma," Phys.-Usp. **53**, 1053 (2010).

[37] E. M. Apfelbaum, B. A. Klumov, A. G. Khrapak, and G. E. Morfill, "On the determination of the particle interaction potential in a dusty plasma from a pair correlation function," JETP Lett. **90**, 332–335 (2009).

[38] H. J. Raveche, R. D. Mountain, and W. B. Streett, "Freezing and melting properties of the lennard-jones system," J. Chem. Phys. **61**, 1970–1984 (1974).

[39] R. Agrawal and D. A. Kofke, "Thermodynamic and structural properties of model systems at solid-fluid coexistence: I. fcc and bcc soft spheres," Mol. Phys. **85**, 23–42 (1995).

[40] M. Zuzic, A. V. Ivlev, J. Goree, G. E. Morfill, H. M. Thomas, H. Rothermel, U. Konopka, R. Sütterlin, and D. D. Goldbeck, "Three-dimensional strongly coupled plasma crystal under gravity conditions," Phys. Rev. Lett. **85**, 4064 (2000).

[41] J. P. Troadec, A. Gervois, and L. Oger, "Statistics of voronoi cells of slightly perturbed face-centered cubic and hexagonal close-packed lattices," Europhys. Lett. **42**, 167 (1998).

[42] P. J. Steinhardt, D. R. Nelson, and M. Ronchetti, "Bond-orientational order in liquids and glasses," Phys. Rev. B **28**, 784 (1983).

[43] W. Lechner and C. Dellago, "Accurate determination of crystal structures based on averaged local bond order parameters," J. Chem. Phys. **129**, 114707 (2008).

[44] P. R. Ten Wolde, M. J. Ruiz-Montero, and D. Frenkel, "Numerical evidence for bcc ordering at the surface of a critical fcc nucleus," Phys. Rev. Lett. **75**, 2714 (1995).

[45] V. S. Kumar and V. Kumaran, "Bond-orientational analysis of hard-disk and hard-sphere structures," J. Chem. Phys. **124**, 204508 (2006).

[46] A. B. de Oliveira, P. A. Netz, T. Colla, and M. C. Barbosa, "Structural anomalies for a three dimensional isotropic core-softened potential," J. Chem. Phys. **125**, 124503 (2006).

[47] S. A. Khrapak and G. E. Morfill, "Ionization enhanced ion collection by a small floating grain in plasmas," Phys. Plasmas (1994–present) **19**, 024510 (2012).

[48] S. A. Khrapak, S. V. Ratynskaia, A. V. Zobnin, A. D. Usachev, V. V. Yaroshenko, M. H. Thoma, M. Kretschmer, H. Höfner, G. E. Morfill, O. F. Petrov *et al.*, "Particle charge in the bulk of gas discharges," Phys. Rev. E **72**, 016406 (2005).

[49] M. Klindworth, O. Arp, and A. Piel, "Langmuir probe diagnostics in the impf device and comparison with simulations and tracer particle experiments," J. Phys. D: Appl. Phys. **39**, 1095 (2006).

Crystallization of a Complex Plasma Under Gravity Conditions in Dependence of Pressure

Benjamin Steinmüller, Christopher Dietz, Michael Kretschmer and Markus H. Thoma
Institute of Experimental Physics I
Justus Liebig University Giessen
35392 Giessen
Germany
Email: Benjamin.Steinmueller@physik.uni-giessen.de
Index Terms—**complex plasma, dusty plasma, crystallization, phase transition**

Abstract—**The crystallization of a three dimensional complex plasma under gravity conditions at different gas pressures is investigated. Three different methods are applied to determine the phase state of the complex plasma; the pair correlation, the nonspherical distribution (which uses the geometric properties of the Voronoi cells of each particle) and an improvement of the scalar product of the local bond order parameter. All criteria are in accordance that the complex plasma is in solid at low and in liquid state at high pressure.**

I. INTRODUCTION

A complex plasma consists of electrons, ions, neutral gas atoms and micro- or submicro-particles. Since electrons have a higher temperature than ions in laboratory plasmas, the immersed particles get negatively charged. Due to the screening of the plasma the interaction of the particles can be described by a Yukawa potential. The interacting strength is the reason for a liquid- or solid-like behavior of the complex plasma. If the coupling parameter

$$\Gamma = \frac{Q^2}{4\pi\epsilon_0 \Delta k_B T_d} \exp\left(-\Delta/\lambda_D\right). \tag{1}$$

exceeds a specific threshold [1] highly ordered structures are created which are called solid or crystalline, while low ordered structures are defined as liquid [2], [3]. The distance of the particles is Δ, their thermal energy $k_B T_d$ and their charge Q. If the electron temperature is much higher than the ion temperature, the Debye screening length can be written as

$$\lambda_D \approx \sqrt{\frac{\epsilon_0 k_B T_i}{e^2 n_i}}. \tag{2}$$

Here the ion density n_i is proportional to the gas pressure p.

II. EXPERIMENT SETUP AND PROCEDURES

A weakly ionized Ar plasma is generated by capacitively coupled RF electrodes with a diameter of 7.5 cm and distance of 3 cm. Melamine - Formaldehyde particles (diameter $d = 2.05$ μm) are injected by a dispenser mounted on the side of the chamber. A horizontal laser sheet illuminates the particles. The plasma as well as the particle cloud are horizontal confined by a guard ring around the electrode. A peak to peak voltage of 15 V at the lower and 35 V at the
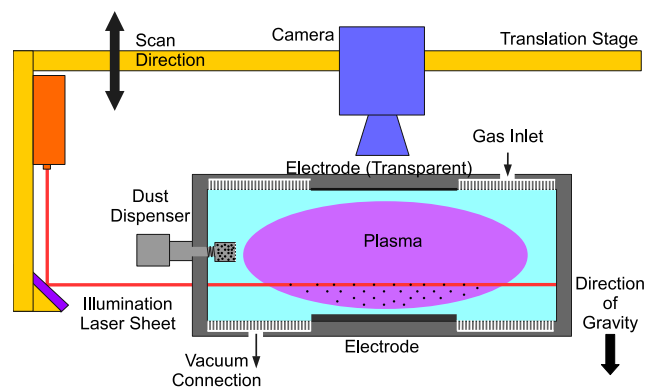

Fig. 1: The setup. The gas inlet as well as the vacuum connection is gas flow reduced, to guarantee that the confinement of the particles is sufficient while pressure manipulation (see [4]).

upper electrode, which is made of glass coated with indium tin oxide (ITO), is applied. Since this electrode is transparent the particles can be recorded by a CMOS camera (resolution 15.6 μm/pixel) on top of the chamber. To determine the three dimensional positions of the particles the laser and the camera are mounted on a stage moving parallel to the direction of gravity (see fig. 1). Every 10 μm a picture is recorded. A cube with a side length of 6 mm around 4.5 mm above the middle of the electrode is chosen to be analyzed, where $1.5 \cdot 10^4$ particles in up to 30 layers are located. Since the observed volume is located above the sheath, it cannot excluded that the shape of the particle cloud in the peripheral area of the complex plasma changes while pressure manipulation.

To ensure that the structure (solid or liquid) of the complex plasma is only an effect of pressure manipulation, the particle density as well as the interparticle distances are kept constant. This is realized by a fixed number of particles.
After injecting the particles the pressure is adjusted slowly. Some structures in the complex plasma are maintained during the slow change of pressure. To ensure that the observed structures at each pressure are independent from previous

conditions, the particles have to be heated up, which is realized by a short increase of the RF power [5]. After lowering the RF power to the former level, the gas is refreshed by a low gas flux. Before recording, the gas flux is switched off, so the particles can arrange without any external disturbance. Then the next pressure is adjusted and the steps are repeated until all desired pressures are realized. To estimate the error all measurements are repeated five times. Between two series the chamber is evacuated to base pressure, before fresh gas and new particles are applied. As a result the number of particles keeps constant in a series, but varies between them.

III. CRITERIA OF PHASE TRANSITIONS

In the pair correlation $g(r)$ the distances to the neighbors are plotted in a histogram calculated by

$$g(r) = \frac{1}{\rho N} \Big\langle \sum_i^N \sum_{j \neq i}^N \delta(\mathbf{r} - \mathbf{r}_{ij}) \Big\rangle. \tag{3}$$

N is the number of particles, ρ their density and $\mathbf{r}_{ij}$ the connecting vector of particle i and j. In periodical systems the pair correlation has distinct maxima and minima [3], [6]. The ratio of the first minimum and the first maximum

$$R = \frac{\min_1(g(r))}{\max_1(g(r))} \tag{4}$$

could be used as an order parameter [7].

The idea behind the nonspherical distribution is that in highly ordered crystals the Voronoi cells are identical and have a small surface S to volume V ratio [8]. The nonsphericity factor is defined as

$$\alpha = \frac{R_c S}{3V}, \tag{5}$$

with the average curvature radius R_c for polyhedrons

$$R_c = \frac{1}{8\pi} \sum_i^{edges} l_i \phi_i. \tag{6}$$

The length of intersecting facet is l_i and the corresponding angle is ϕ_i (in units of radian). For hcp (hexagonal close-packed) and fcc (face-centered cubic) crystals the histogram of the nonspherical distribution is sharply peaked around 1.22, for less ordered systems it disperses to higher values.

The scalar product of the local bond order parameter (SPBOP) determines, whether each individual particle is in liquid or in solid state. For the twelve nearest neighbors N the bond order parameter $q_{lm}(\mathbf{r}_i)$ is given by

$$q_{lm}(\mathbf{r}_i) = \frac{1}{N} \sum_{j=1}^N Y_{6m}(\theta(\mathbf{r}_{ij}), \phi(\mathbf{r}_{ij})). \tag{7}$$

The spherical harmonics functions Y_{6m} are of degree 6 ($l = 6$), because they are the most sensitive for this utilization, the respective angles are $\theta(\mathbf{r}_{ij})$ and $\phi(\mathbf{r}_{ij})$. After normalization

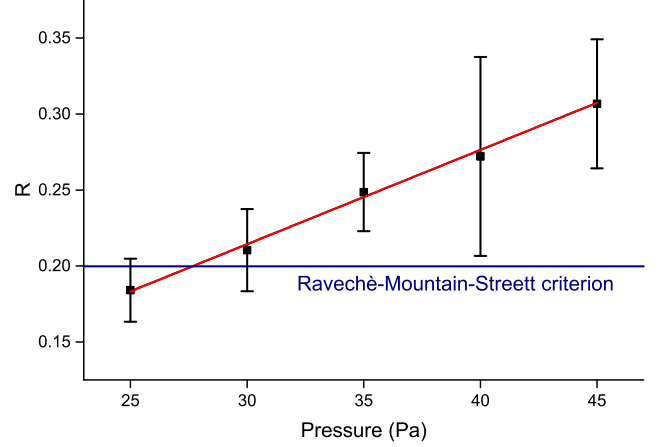$$\tilde{q}_{6m}(i) = \frac{q_{6m}}{\left(\sum_{m=-6}^6 |q_{6m}(i)|^2 \right)^{1/2}} \tag{8}$$

Fig. 2: Ratio R (4), following the criteria by Raveché, Mountain and Streett [7]. A system is in solid state if $R < 0.2$. The errorbars show the standard deviation [4].

the scalar product for two neighboring particles

$$S_{ij} = \sum_{m=-6}^6 \tilde{q}_{6m}(i) \cdot \tilde{q}_{6m}^*(j) \tag{9}$$

is calculated (* symbolizes complex conjugation). Due to the high symmetry in the particle arrangement the scalar product adds up coherently in crystals. In undisturbed data the product is for all neighboring particles unity. Since every slight disorder decreases this value, for real data a threshold of 0.75 is adopted. To increase the reliability of this criterion, a specific particle is only identified to be in solid state, if the scalar product (9) with at least eight of its twelve neighbors exceeds this threshold. Otherwise it is considered to be in liquid state. Both thresholds for determining a specific particle to be in the solid state (the minimum value of the product and the number of neighbors which has to exceed this value) can be used as more or less strict criteria for crystallization [9], [10], [11].

However, even small displacements of the particles positions can change the neighborhood completely, which makes the SPBOP unstable [12]. To solve this issue the scalar product of the Minkowski structure metric (SPMSM) was proposed [4]. Instead of a fixed number of nearest neighbors, the Voronoi neighbors are used and weighted by their respective Voronoi facet area $A(f)$. So (7) is changed to

$$q'_{6m}(i) = \sum_{f \epsilon \mathcal{F}(i)} \frac{A(f)}{A} Y_{6m}(\theta_f, \phi_f). \tag{10}$$

The surface A of the Voronoi cell is given by

$$A = \sum_{f \in \mathcal{F}(i)} A(f). \tag{11}$$

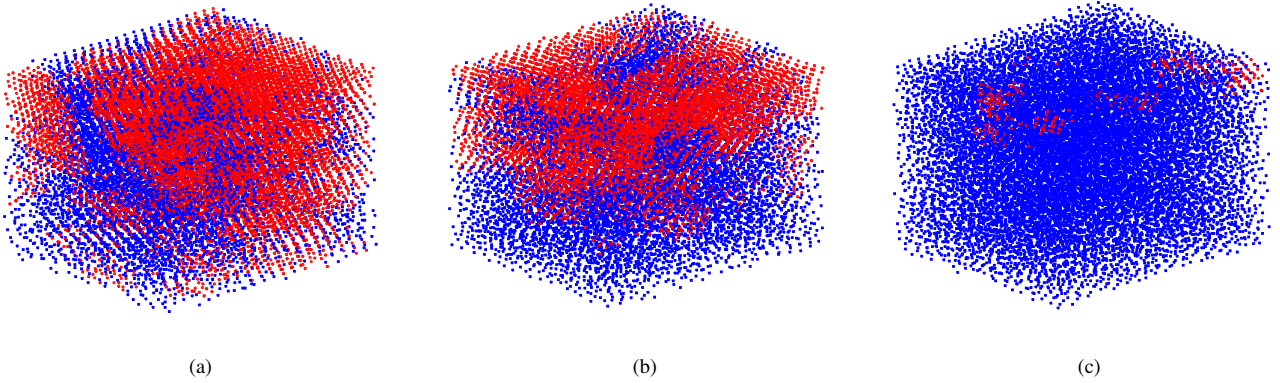After normalization (see eq. 8), the scalar product of two

Fig. 4: (Color online) Position of particles being in solid state ● and in liquid state ■ at a) 25 Pa, b) 35 Pa and c) 45 Pa according to SPMSM. Here a particle is identified as being in solid state if S'_{ij} (12) exceeds 0.75 for at least eight of its Voronoi neighbors. All other particles are determined as being in liquid state. For better visibility the figures are shown upside down.
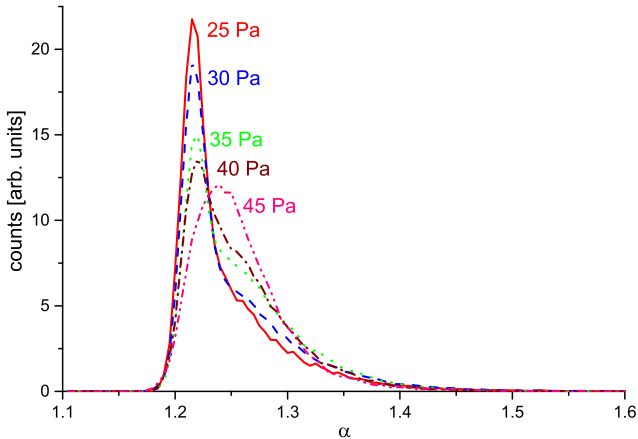

Fig. 3: The nonspherical distribution α (area normalized) [4].

Voronoi neighboring particles

$$S'_{ij} = \sum_{m=-6}^{6} \tilde{q}'_{6m}(i) \cdot \tilde{q}'^{*}_{6m}(j) \tag{12}$$

shows similar properties like the SPBOP. So analogous thresholds could be applied: if the scalar product exceeds 0.75 for at least eight of its Voronoi neighbors a particle is defined as being in solid state, else as being in liquid state [4].

IV. RESULTS

The pair correlation is used to determine the state of aggregation of a complex plasma. At low pressures the distribution shows distinct maxima and minima. At increased pressure the distribution disperses. Figure 2 shows the ratio of the first minimum to the first maximum (4). The pair correlation does not deal well with heterogeneous structures. So the high values could also originate from inhomogeneous structures, like variations of interparticle distances based on gravity or different crystal structures [13], [14]. To get a deeper insight into the details a more local criterion is used.

In figure 3 the results of the nonspherical distribution are plotted in a histogram. It is shown, that at 25 Pa the distribution is peaked at around 1.22, which is in accordance with the predicted value for a hcp and fcc crystal. The distribution disperses to higher values at increased pressure, which also indicate less ordered structures.

In order to localize the particles, which are in liquid or in solid state, the SPMSM is used. Figure 4 shows the positions of the particles being in solid and in liquid state. The particles which are located in the lower layers (shown on top) have the highest probability to be in solid state, while in the upper area the particles are rather in liquid state. Finding more ordered structures in lower layers and less ordered structures in higher layers under gravity conditions is in agreement with Zuzic et al. [13]. Beside this, particles being in solid state are creating clusters, which are embedded by particles being in liquid state.

Figure 5 summarizes the results of the SPBOP and SPMSM at different pressures. Both criteria are in great accordance with each other, while the SPMSM identifies slightly more particles being in solid state. At high pressure the particles are in liquid state, while at decreased pressure most of them are in solid state.

The results of all applied criteria are in good agreement with each other. A continuous phase transition between 25 Pa, where nearly all particles are in the solid state, and 45 Pa, where all particles are in the liquid state, is observed.
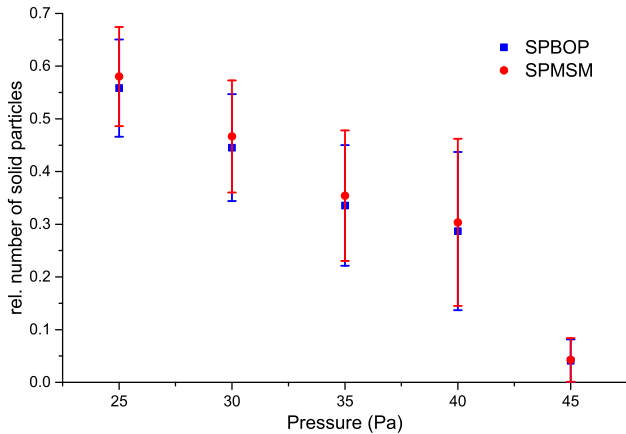
Fig. 5: The relative number of particles being in the solid state based on the scalar product of the local bond order parameter *SPBOP* ■ and of the Minkowski structure metric *SPMSM* ●. The same criteria as in fig 4 are used. The errorbars indicate the standard deviation [4].

V. Discussion

Increasing the neutral gas pressure at constant temperature increases the number density of the gas atoms which makes collisions of ions with neutrals more likely. An ion, which lost its energy and angular momentum by such a collision in the vicinity of a particle, has a smaller chance to escape from the attractive potential of this particle. The resulting higher ion flow to the particle surface reduces the negative charge Q [15]. Beside this the Debye length was decreased by increasing neutral gas pressure (2). Due to the constant particle number while pressure manipulation, the mean interparticle distance (roughly 0.22 mm) does not change significantly.

The lower Debye length and the lower charge of the particles lead to a decreased coupling parameter (1), while the pressure is increased (supposing a constant particle temperature). The diminished coupling parameter could explain the crystallization at low pressure, observed here.

In former ground based experiments particles were in liquid state at low pressure and in solid state at high pressure [2], [5], [16]. One possible explanation of this behavior could be the formation of a two-stream instability [17]. Owing to gravity, in these experiments the particles, which create only few particle layers, are located close to the plasma sheath. In the present work the analyzed particles extend into the bulk plasma. As a result the particle layers in the lower part become compressed by the upper layers. This "pressure" compresses the interparticle distances and increases the coupling parameter (1) (see [13], [14]). Beside this the light particles allowed us to use only a small RF power. The exerted pressure on the lower particles as well as the low power were the reasons, why no formation of such an instability was observed at the examined pressure regime.

VI. Conclusions

The influence of neutral gas pressure of a three dimensional complex plasma under gravity conditions is considered. All applied criteria show the same picture: at low pressure the particles are in solid state, while at increased pressure the particles are in liquid state. The position of the extended particle cloud as well as the low RF-power could be the reason for this behavior in contrast to former experiments under gravity conditions.

References

[1] S. Ichimaru, "Strongly coupled plasmas: high-density classical plasmas and degenerate electron liquids," *Reviews of Modern Physics*, vol. 54, no. 4, p. 1017, 1982.

[2] H. M. Thomas and G. E. Morfill, "Melting dynamics of a plasma crystal," 1996.

[3] B. A. Klumov, "On melting criteria for complex plasma," *Physics-Uspekhi*, vol. 53, no. 10, p. 1053, 2010.

[4] B. Steinmüller, C. Dietz, M. Kretschmer, and M. Thoma, "Crystallization of a three-dimensional complex plasma under laboratory conditions," *Physics of Plasmas*, vol. 24, no. 3, p. 033705, 2017.

[5] A. Melzer, A. Homann, and A. Piel, "Experimental investigation of the melting transition of the plasma crystal," *Physical Review E*, vol. 53, no. 3, p. 2757, 1996.

[6] E. M. Apfelbaum, B. A. Klumov, A. G. Khrapak, and G. E. Morfill, "On the determination of the particle interaction potential in a dusty plasma from a pair correlation function," *JETP letters*, vol. 90, no. 5, pp. 332–335, 2009.

[7] H. J. Raveche, R. D. Mountain, and W. B. Streett, "Freezing and melting properties of the lennard-jones system," *The Journal of Chemical Physics*, vol. 61, no. 5, pp. 1970–1984, 1974.

[8] J. C. G. Montoro and J. L. F. Abascal, "The voronoi polyhedra as tools for structure determination in simple disordered systems," *The Journal of Physical Chemistry*, vol. 97, no. 16, pp. 4211–4215, 1993.

[9] W. Lechner and C. Dellago, "Accurate determination of crystal structures based on averaged local bond order parameters," *The Journal of chemical physics*, vol. 129, no. 11, p. 114707, 2008.

[10] P. R. Ten Wolde, M. J. Ruiz-Montero, and D. Frenkel, "Numerical evidence for bcc ordering at the surface of a critical fcc nucleus," *Physical review letters*, vol. 75, no. 14, p. 2714, 1995.

[11] P. R. ten Wolde, M. J. Ruiz-Montero, and D. Frenkel, "Numerical calculation of the rate of crystal nucleation in a lennard-jones system at moderate undercooling," *The Journal of chemical physics*, vol. 104, no. 24, pp. 9932–9947, 1996.

[12] W. Mickel, S. C. Kapfer, G. E. Schröder-Turk, and K. Mecke, "Shortcomings of the bond orientational order parameters for the analysis of disordered particulate matter," *The Journal of chemical physics*, vol. 138, no. 4, p. 044501, 2013.

[13] M. Zuzic, A. V. Ivlev, J. Goree, G. E. Morfill, H. M. Thomas, H. Rothermel, U. Konopka, R. Sütterlin, and D. D. Goldbeck, "Three-dimensional strongly coupled plasma crystal under gravity conditions," *Physical review letters*, vol. 85, no. 19, p. 4064, 2000.

[14] P. Huber, "Untersuchung von 3-d plasmakristallen," Ph.D. dissertation, München, 2011.

[15] S. A. Khrapak and G. E. Morfill, "Ionization enhanced ion collection by a small floating grain in plasmas," *Physics of Plasmas (1994-present)*, vol. 19, no. 2, p. 024510, 2012.

[16] Y. Ivanov and A. Melzer, "Melting dynamics of finite clusters in dusty plasmas," *Physics of Plasmas (1994-present)*, vol. 12, no. 7, p. 072110, 2005.

[17] G. Joyce, M. Lampe, and G. Ganguli, "Instability-triggered phase transition to a dusty-plasma condensate," *Physical review letters*, vol. 88, no. 9, p. 095006, 2002.

Crystallization process of a three-dimensional complex plasma

Benjamin Steinmüller,[*] Christopher Dietz, Michael Kretschmer, and Markus H. Thoma

Institute of Experimental Physics I, Justus Liebig University Giessen, Heinrich-Buff-Ring 16, 35392 Giessen, Germany

Characteristic timescales and length scales for phase transitions of real materials are in ranges where a direct visualization is unfeasible. Therefore, model systems can be useful. Here, the crystallization process of a three-dimensional complex plasma under gravity conditions is considered where the system ranges up to a large extent into the bulk plasma. Time-resolved measurements exhibit the process down to a single-particle level. Primary clusters, consisting of particles in the solid state, grow vertically and, secondarily, horizontally. The box-counting method shows a fractal dimension of $d_f \approx 2.72$ for the clusters. This value gives a hint that the formation process is a combination of local epitaxial and diffusion-limited growth. The particle density and the interparticle distance to the nearest neighbor remain constant within the clusters during crystallization. All results are in good agreement with former observations of a single-particle layer.

I. INTRODUCTION

The crystallization process of various materials are of great interest in solid state physics. In actual materials, the specific timescales and size scales make a detailed study of the involved processes unattainable. Computer simulations [1] or model systems such as colloidal systems [2] and complex plasmas [3] may help to overcome these limitations. In complex plasmas the length scales and timescales are in the range of minutes and millimeters. The positions of each individual particle, as well as collective effects in the aggregation process, can be recorded [4]. The timescales in colloidal systems range from seconds to days and the length scales are in the range of the wavelength of visible light [5].

A complex plasma consists of micron-sized particles embedded in a low-temperature plasma. These particles charge up negatively due to the high electron velocity and interact via the Yukawa potential. Depending on the ratio of the interacting energy to the thermal energy, the particles may arrange in solid or liquid configurations [3]. Under laboratory conditions, the particles have to be levitated to counter gravity, e.g., by an electric field. Owing to the screening of electric fields in the plasma, the particles are often arranged in a single layer or in a few layers located in the sheath [6]. Since all particles can be observed simultaneously in a single layer, the melting [7–9] and crystallization [10] of flat complex plasmas are well understood. Under certain conditions (small particles and a strong confinement), it is possible that the particle cloud ranges up into the presheath and bulk plasma even in ground-based experiments [11,12]. Also, computer simulations were performed to study the phase transition of three-dimensional complex plasmas [13,14].

A widespread method to analyze the process of aggregation in detail is the determination of the fractal dimension [15–17]. In epitaxial growth (at least at the beginning), one layer after another settles on the surface, creating compact objects with the same dimension as of the embedding Euclidean space [18]. A different picture is shown by diffusion-limited growth, where the exposed ends of a structure screen their own center. As a result, the ends grow faster than the remaining parts and branched complex objects are created [19,20]. In three-dimensional embedding Euclidean space, the fractal dimension for irreversible diffusion-limited cluster-cluster aggregation (DLCA) [21] is $d_f = 1.78 \pm 0.06$, and for irreversible diffusion-limited aggregation (DLA) [22] it is $d_f = 2.53 \pm 0.06$ [19]. If the growth is reversible, the bonds can be destroyed and the particles can rearrange, creating much more compact objects. For this reason, reversibility increases the fractal dimension of the grown structures towards the value for the embedding Euclidean dimension [17].

Rubin-Zuzici *et al.* [13] have examined a contour in a two-dimensional slice of a three-dimensional complex plasma during the phase transition. It is shown that the fractal dimension d'_f of the crystallization front line oscillates between 1.16 and 1.21. This is higher than for epitaxially grown structures (in this context, $d = 1$) and lower for diffusion-limited growth (in this context, $d_f = 1.42$) [13]. For a two-dimensional slice, the overall fractal dimension of the crystallization front is decreased by 1 [23]. This means that in the originally embedding three-dimensional Euclidean space, the front area has a fractal dimension of $d_f = 2.16$–2.21.

Previously, only colloidal systems were used as model systems to observe the aggregation process in three dimensions. Based on the high fluid density of the surrounding fluid, the colloidal systems are overdamped. Due to the low damping rate, complex plasmas may provide new insights into the phase transition process in general [24].

In the presented work, the crystallization process of a liquidlike three-dimensional complex plasma under gravity conditions is studied. The measurements are time and space resolved. A local criterion shows individual particles in the solid state at particular time steps, from which the fractal dimension of the clusters can be derived.

[*]Benjamin.Steinmueller@physik.uni-giessen.de

II. EXPERIMENTAL SETUP AND PROCEDURE

A capacitively coupled radio-frequency chamber with a frequency of 13.56 MHz (peak-to-peak voltage of 15 V at the lower and 35 V at the upper electrode) is used for the experiments. The electrodes have a diameter of 7.5 cm and are 3 cm apart from each other, and the diameter of the chamber is 14 cm. Glass coated with indium tin oxide (ITO) is used as the upper electrode. Due to the transparency of this electrode, it is possible to mount the camera directly above it. The melamine-formaldehyde particles inside the complex plasma have a diameter of $d = 2.05 \pm 0.04$ μm and are injected by a dispenser mounted on the side of the chamber. Due to the small particle mass, a weak electric field in the bulk plasma is sufficient for levitation. Besides the electric field and the gravity, no significant forces act on the particle. A guard ring around the lower electrode is responsible for the horizontal confinement of the particle cloud. The experiments described here are performed in argon at a pressure of 40 Pa. To illuminate the particles, a laser beam (width $\approx$0.1 mm) is spread into a sheet parallel to the electrodes. The laser light, which is scattered by the particles, is recorded by a camera perpendicular to the laser sheet. Further information about the experimental setup is given in Ref. [11].

To observe its phase transition from a liquid- to crystal-like system, the complex plasma has to be fully disordered in the beginning. This is achieved by a temporal increase of rf power to a peak-to-peak voltage of 52 V at the lower and 92 V at the upper electrode, in which the particles gain a high kinetic energy [9]. When the power is reduced again, crystallization starts. Three-dimensional positions of the particles are acquired by moving the laser diode, as well as the camera, in a vertical direction perpendicular to the electrodes. Several scans are taken at different times, in order to get time-resolved measurements. A scan with a speed of 0.1 mm/s starts at the upper part of the complex plasma and ends in the lower part [25]. The next scan goes from the lower to the upper part, with each scan taking about 33 s. This scan velocity is of the same order as used in other plasma crystal experiments [12,26–29]. To reconstruct the position of the particles, first, the particles are identified in each single frame with subpixel accuracy and then they are tracked over consecutive frames [30]. The z coordinate of the particles is calculated by the position of the laser sheet above the electrode. Particles in the solid state oscillate around their equilibrium positions [31], with an amplitude of about 23 μm in the x and y directions. Due to the low scanning speed, with this method it is possible to gain the exact equilibrium positions of the particles in the horizontal plane by averaging over time since the particles are identified in several frames. Due to the fact that this is not possible for the scan direction, the z coordinate has an uncertainty in the range of the oscillation amplitude. Assuming a typical thermal energy ($\sim$0.025 eV), particles in the liquid state have a higher kinetic velocity than the scanning speed. This is a widespread issue in three-dimensional complex plasmas [12,26–29] or even in two dimensions, where a particle can move between two frames further than the mean interparticle distance [13]. As a result, only the positions of particles in the solid state are determined with high accuracy, while the positions of particles in the liquid state have large uncertainties.

The drawback of the scanning method is that not all particles are recorded simultaneously. The scans are done 0, 33, 66, 99, 178, 211, and 244 s after reducing the rf power. In the following, the particle positions are named after the starting time of the corresponding scan. The complementary metal-oxide semiconductor (CMOS) camera has a resolution of 15.6 μm/pixel and a frame rate of 40 fps. The region of interest of about $10 \times 10 \times 4$ mm^3 contains over 36 000 particles. The examined region is chosen from the homogeneous center of the particle cloud, 3.5 mm above the lower electrode, which is above the sheath region with a maximal extension of about 1 mm [32] (Debye length $\sim$100 μm). Taking an even distribution of particles within the confinement into account, the whole cloud consists of about 1.6×10^6 particles. Since no gas flux is present, the particles do not move collectively, nevertheless, some particles can diffuse inside and outside of the examined region.

III. FRACTAL SCALE ANALYSIS

In a complex plasma, three different crystalline structures can occur: hexagonal closed packed (hcp), face-centered cubic (fcc), and body-centered cubic (bcc). In this investigation, the exact crystal structure is not important, but a reliable identification of whether a single particle is in the liquid or in the solid state is important. This is why the scalar product of the Minkowski structure metric (SPMSM) is applied. This method is robust against uncertainties up to 14% of the nearest-neighbor distance in the particle positions, e.g., because of oscillation in the scan direction. This is why the x and y coordinates of the particles have to be determined with high accuracy, otherwise the sum of the errors in each direction would be too high for a reliable identification via the SPMSM [11,33–35].

For a particle i, the order parameters

$$q_{6m}(i) = \sum_{f \epsilon \mathcal{F}(i)} \frac{A(f)}{A} Y_{6m}(\mathbf{r}_{ij}) \qquad (1)$$

are calculated. Here, Y_{6m} are the spherical harmonics with $l = 6$, and the sum runs over all Voronoi neighbors. The connecting vector of the two neighboring particles i and j is $\mathbf{r}_{ij}$. The surface of the Voronoi cell A is defined by the sum over the corresponding facet areas $A(f)$ $[A = \sum_{f \in \mathcal{F}(i)} A(f)]$. Then, the complex vector is normalized over all possible orders m given by

$$\tilde{q}_{6m}(i) = \frac{q_{6m}(i)}{\sqrt{\sum_{m=-6}^{6} |q_{6m}(i)|^2}}. \qquad (2)$$

If, for neighboring particles i and j, the product

$$S_{ij} = \sum_{m=-6}^{6} \tilde{q}_{6m}(i) \cdot \tilde{q}_{6m}^*(j) \qquad (3)$$

is above 0.75, they are deemed to be connected (the asterisk $*$ stands for complex conjugation). With eight or more connections to its neighbors, a particle is defined to be in the solid state, and with less connections, to be in the liquid state [11].

Fractal objects are self-similar or scale invariant, which means, in a mathematical sense, that changing the scale produces similar structures. In contrast to the embedding Euclidean space, fractals have noninteger dimensions. One of the most commonly used procedures to determine the fractal dimension is the box-counting method [36]. Here, the minimum number of boxes $N(L)$ with the length L, which are needed to cover the fractal, are counted. The fractal dimension d_f is then given by [19]

$$d_f \propto \lim_{L \to 0} \frac{\log[N(L)]}{\log(1/L)}. \tag{4}$$

The probability for a specific particle to be in the solid state is called p. In percolation theory, the lowest probability for which the size of the largest cluster [37] reaches the same order as the size of the examined region is called the critical probability p_c. Following Ref. [23], the fractal dimension of a cluster with $p < p_c$ is zero. If p is clearly above p_c, the largest cluster is no longer fractal, so its dimension is given by the embedding Euclidean space. Only for $p = p_c$ (or slightly above) does the largest cluster have a fractal nature [23].

IV. RESULTS

Figure 1 shows the crystallization process of the complex plasma under gravity conditions. Directly after decreasing the rf power (at 0 s), hardly any particles are found in the solid state, indicating that due to the temporally increased rf power, all particles obtain so much kinetic energy that no ordered structures can exist. After 244 s, most particles are in the solid state, confirming a timescale for crystallization of minutes. During the phase transition, the particles in the solid state create clusters. The clusters originate preferably from the lower part of the examined region. They grow mainly against the direction of gravity and are less pronounced in the horizontal direction. While the individual solid clusters increase in size, they merge with each other. Nevertheless, no compact crystallization front is observed.

Due to the crystallization process, the amount of particles in the solid state and therefore the probability p increases (see Fig. 1). The critical value for p is reached after about 178 s, when the largest solid cluster connects the upper with the lower boundary for the first time. The ratio of particles in the solid state and the total number of particles in the examined region give an upper limit of 0.3 for the critical probability p_c.

Figure 2 shows the amount $N(L)$ of boxes where at least one particle of the cluster is included versus the length of the boxes L in a double logarithmic scale. The slope of the linear fit gives a fractal dimension of $d_f = 2.72 \pm 0.03$. Changing the threshold for connected particles (3) varies the number of particles identified to be in the solid or liquid state. At a lower threshold the critical probability p_c is reached earlier, while at a higher threshold it is achieved later. Nevertheless, the absolute value for the fractal dimension at (or slightly above) the critical probability remains constant. Since the fractal dimension appears to be time independent, we do not expect that a finite scanning time affects its value. Of course, the exact structure of a cluster at a certain moment cannot be extracted. After all, this does not have an influence on the final results.
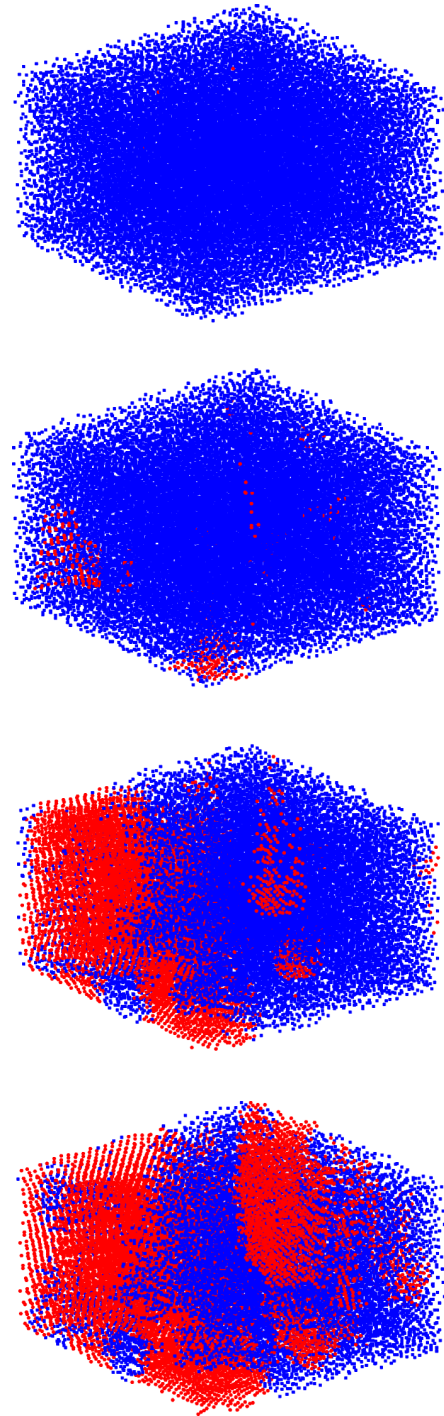

FIG. 1. The positions of particles in the solid (red/light) and liquid (blue/dark) state, 0, 66, 178, and 244 s (from top to bottom) after the crystallization process has begun. Due to their high thermal speed, the absolute position of the particles in the liquid state may have an error.

In Fig. 3 the distance to the nearest neighbor as well as the density of the particles are plotted, based on particles embedded completely in the solid state. Due to gravity, the interparticle distances are compressed. Averaged over all times in a cluster, the density of particles increases from 78 ± 3 mm^{-3}
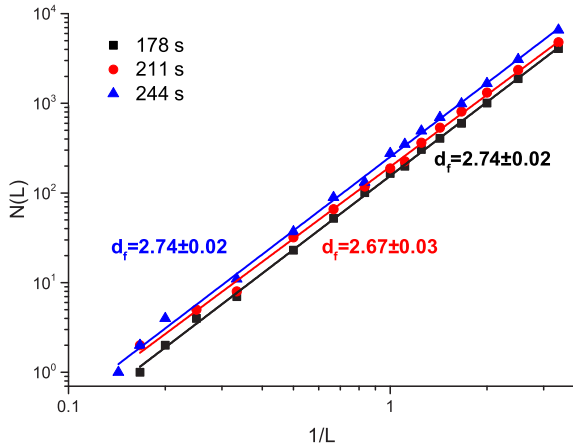
FIG. 2. The relation between the minimum amount of boxes needed to cover the largest solid cluster $N(L)$ and the corresponding length of the box L. The scans are done at 178 s , 211 s, and 244 s after the start of crystallization.

in the upper 20% to 87 ± 3 mm^{-3} in the lower 20% of the examined region. While crystallization progresses, the mean number density of particles and the average interparticle distance as well as their standard deviations remain constant over time. In previous experiments it was shown that the variation of particle density or interparticle distance during a phase transition was very small [8,13].

V. CONCLUSION

The crystallization process of a three-dimensional complex plasma with more than 36 000 particles under gravity conditions was resolved temporally and spatially. To this end, at different times after the start of crystallization, a space-resolved local method was used to identify whether each single particle was in the solid or liquid state. It has been confirmed that the timescales and size scales for phase transitions in a complex plasma are in a range of a few minutes and millimeters, respectively. The plasma parameters are in a steady state only microseconds after the rf power is lowered [38] and the charge of the particles needs milliseconds to be in equilibrium. During the crystallization process, no significant change of the particle density took place. The different timescales of the involved processes allowed the assumption that the background plasma and the mean charge of the particles were constant.

Crystallization takes place by the growth of different solid clusters, starting from the lower part under gravity. These clusters primarily expand vertically and, secondarily, horizontally. At later times they merge with each other. About 178 s after the start of crystallization, the extent of the largest solid cluster was in the range of the size of the examined region. At this time, the probability to determine a specific particle to be in the solid state was about 0.3, resulting in a critical value of $p_c \lesssim 0.3$. After the critical probability was attained, the box-counting method yielded a fractal dimension of $d_f = 2.72 \pm 0.03$, which lies between the values for epitaxial growth ($d = 3$) and for diffusion-limited growth ($d_f \approx 2.5$), indicating the observed crystallization process was governed by both growth mechanisms. This observation is in accordance with former observations of complex plasmas in two dimensions [13]. Since the calculated fractal dimension is much higher than for diffusion-limited cluster-cluster growth ($d_f \approx 1.8$), this phenomenon can be excluded as the dominant growth process. Since reversibility can also increase the fractal dimension, reversible diffusion-limited aggregation could also contribute to the observed fractal dimension of $d_f = 2.72 \pm 0.03$.

It should be kept in mind that, in contrast to the formal mathematical definition of a fractal in a physical system, self-affinity is only realized in a certain range, since it has a lowest size (at least one interparticle distance $\propto 0.2$ mm) and a largest size (diameter of the examined region $\propto 10$ mm). Due to this limitation, the method which is utilized to determine the fractal dimension could influence the result [36,39]. Furthermore, it could not be excluded, based on the limited time resolution, that the critical value for the probability was reached before the scan was done. This could have an effect on the calculated fractal dimension, if the measured probability was significantly larger than the critical value. Nevertheless, Fig. 2 shows no strong time dependence for the fractal dimension. Besides this, no measurable changes in number density or in interparticle distances were observed within the clusters during crystallization.

All observed effects are in good agreement with former experiments, using two-dimensional data. Due to their lower damping rate compared to colloidal systems, complex plasmas are a valuable tool for understanding phase transitions in three dimensions.
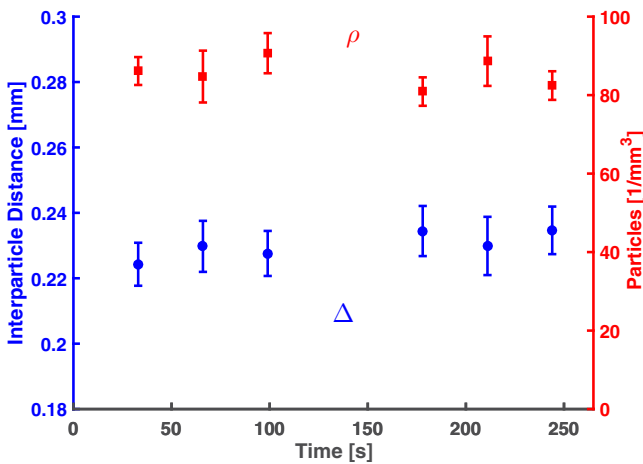

FIG. 3. The particle density (calculated by the inverse volume of the Voronoi cell [29]) and the distance to the nearest neighbor for particles within a cluster depending on the time after starting the crystallization. The standard deviation in each time step is given by the error bars.

[1] J. Anwar and D. Zahn, Angew. Chem., Int. Ed. **50**, 1996 (2011).

[2] T. Palberg, J. Phys.: Condens. Matter **11**, R323(R) (1999).

[3] V. E. Fortov, A. V. Ivlev, S. A. Khrapak, A. G. Khrapak, and G. E. Morfill, Phys. Rep. **421**, 1 (2005).

[4] A. P. Nefedov, G. E. Morfill, V. E. Fortov, H. M. Thomas, H. Rothermel, T. Hagl, A. V. Ivlev, M. Zuzic, B. A. Klumov, A. M. Lipaev, I. V. Molotkov, O. F. Petrov, Y. P. Gidzenko, S. K. Krikalev, W. Shepard, A. I. Ivanov, M. Roth, H. Binnenbruck, J. A. Goree, and Y. Semenov, New J. Phys. **5**, 33 (2003).

[5] T. Palberg, Curr. Opin. Colloid Interface Sci. **2**, 607 (1997).

[6] E. B. Tomme, D. A. Law, B. M. Annaratone, and J. E. Allen, Phys. Rev. Lett. **85**, 2518 (2000).

[7] H. M. Thomas and G. E. Morfill, Nature (London) **379**, 806 (1996).

[8] T. Sheridan, Phys. Plasmas **15**, 103702 (2008).

[9] A. Melzer, A. Homann, and A. Piel, Phys. Rev. E **53**, 2757 (1996).

[10] C. A. Knapek, D. Samsonov, S. Zhdanov, U. Konopka, and G. E. Morfill, Phys. Rev. Lett. **98**, 015004 (2007).

[11] B. Steinmüller, C. Dietz, M. Kretschmer, and M. Thoma, Phys. Plasmas **24**, 033705 (2017).

[12] M. Zuzic, A. V. Ivlev, J. Goree, G. E. Morfill, H. M. Thomas, H. Rothermel, U. Konopka, R. Sütterlin, and D. D. Goldbeck, Phys. Rev. Lett. **85**, 4064 (2000).

[13] M. Rubin-Zuzic, G. Morfill, A. Ivlev, R. Pompl, B. Klumov, W. Bunk, H. Thomas, H. Rothermel, O. Havnes, and A. Fouquet, Nat. Phys. **2**, 181 (2006).

[14] B. A. Klumov and G. Morfill, JETP Lett. **90**, 444 (2009).

[15] T. Terao and T. Nakayama, Phys. Rev. E **58**, 3490 (1998).

[16] P. Dimon, S. K. Sinha, D. A. Weitz, C. R. Safinya, G. S. Smith, W. A. Varady, and H. M. Lindsay, Phys. Rev. Lett. **57**, 595 (1986).

[17] S. D. Orrite, S. Stoll, and P. Schurtenberger, Soft Matter **1**, 364 (2005).

[18] A. C. Levi and M. Kotrla, J. Phys.: Condens. Matter **9**, 299 (1997).

[19] T. Vicsek, *Fractal Growth Phenomena*, 2nd ed. (World Scientific, Singapore, 1992).

[20] T. A. Witten, Jr., and L. M. Sander, Phys. Rev. Lett. **47**, 1400 (1981).

[21] In the DLCA model, particles are distributed randomly. In each "time step," an arbitrary chosen particle or cluster is moved in any direction. If a particle or a cluster touches another particle, they stick together.

[22] Following the DLA model, one after another particle starts far from a single cluster and walks at random, until it arrives at the cluster and sticks to it.

[23] A. Aharony and D. Stauffer, *Introduction to Percolation Theory*, 2nd ed. (Taylor & Francis, London, 2003).

[24] S. A. Khrapak, A. V. Ivlev, and G. E. Morfill, Phys. Rev. E **70**, 056405 (2004).

[25] A higher scanning velocity of ≈1.6 mm/s shows compatible results.

[26] H. Thomas, G. Morfill, and V. Tsytovich, Plasma Phys. Rep. **29**, 895 (2003).

[27] M. Thoma, M. Kretschmer, H. Rothermel, H. Thomas, and G. Morfill, Am. J. Phys. **73**, 420 (2005).

[28] S. A. Khrapak, B. A. Klumov, P. Huber, V. I. Molotkov, A. M. Lipaev, V. N. Naumkin, A. V. Ivlev, H. M. Thomas, M. Schwabe, G. E. Morfill, O. F. Petrov, V. E. Fortov, Y. Malentschenko, and S. Volkov, Phys. Rev. E **85**, 066407 (2012).

[29] V. N. Naumkin, D. I. Zhukhovitskii, V. I. Molotkov, A. M. Lipaev, V. E. Fortov, H. M. Thomas, P. Huber, and G. E. Morfill, Phys. Rev. E **94**, 033204 (2016).

[30] J. C. Crocker and D. G. Grier, J. Colloid Interface Sci. **179**, 298 (1996).

[31] Y. Ivanov and A. Melzer, Phys. Plasmas **12**, 072110 (2005).

[32] A. Piel, *Plasma Physics: An Introduction to Laboratory, Space, and Fusion Plasmas* (Springer, Berlin, 2017).

[33] W. Mickel, S. C. Kapfer, G. E. Schröder-Turk, and K. Mecke, J. Chem. Phys. **138**, 044501 (2013).

[34] C. Dietz, T. Kretz, and M. H. Thoma, Phys. Rev. E **96**, 011301(R) (2017).

[35] C. Dietz and M. H. Thoma, Phys. Rev. E **94**, 033207 (2016).

[36] S. Buczkowski, S. Kyriacos, F. Nekka, and L. Cartilier, Pattern Recognit. **31**, 411 (1998).

[37] A solid cluster is created by a group of particles in the solid state, which are Voronoi neighbors. This means such a cluster consists only of particles in the solid state, linked to each other by a chain of neighbors, also part of the cluster [23].

[38] E. Carbone, N. Sadeghi, E. Vos, S. Hübner, E. Van Veldhuizen, J. Van Dijk, S. Nijdam, and G. Kroesen, Plasma Sources Sci. Technol. **24**, 015015 (2014).

[39] B. B. Mandelbrot, Phys. Scr. **32**, 257 (1985).

EDITORS' CHOICE

Recent microgravity experiments with complex direct current plasmas

C. Dietz | M. Kretschmer | B. Steinmüller | M.H. Thoma[*]

I. Physikalisches Institut,
Justus-Liebig-Universitaet Giessen, Giessen,
Germany

*Correspondence
M.H. Thoma, I. Physikalisches Institut,
Justus-Liebig-Universitaet Giessen,
Heinrich-Buff-Ring 16, 35392 Giessen, Germany.
Email:
markus.h.thoma@exp1.physik.uni-giessen.de

Complex plasmas are low-temperature plasmas containing micrometer-sized particles. They are useful as models for strongly coupled many-body systems. Since the microparticles are strongly affected by gravity, microgravity experiments with complex plasmas are conducted. Here we report on recent microgravity experiments with the experimental facility PK-4 performed in parabolic flights. In particular, we discuss electrorheological and demixing experiments and the image analysis tools used.

KEYWORDS
complex plasmas, microgravity

1 | INTRODUCTION

Complex or dusty plasmas are plasmas containing micrometer-sized particles, for example, dust grains. They are present in astrophysical objects such as comets, protoplanetary discs, or planetary rings,[1] as well as in technological applications, for example, in plasma etching processes used in microchip production.[2] In fundamental physics they are of great interest because they are ideal models for investigating many-body systems on the microscopic and dynamical level in real time in laboratory experiments.[3–5] In these experiments, usually low-temperature plasmas at low pressures are produced in which monodisperse microparticles are injected. The microparticles are negatively charged up to several thousand elementary charges depending on the particle size due to electron collection on their surface. Therefore, they form a strongly coupled component of the plasma. One of the most exciting discoveries was the formation of the plasma crystal due to the strong inter-particle interaction.[6–9] Complex plasmas, as an example for soft matter, are particularly useful for studying general properties and mechanisms of the statistical physics of many-body systems because of the following reasons:

- Complex plasmas can be produced without much effort in small plasma chambers (table-top experiments) and the microparticles can be observed easily with cameras using laser illumination.
- From the camera images, microscopic observations of the behavior of the individual microparticles are possible.
- The positions and velocities of the microparticles can be extracted, giving the entire phase space information.
- Complex plasmas are transparent since the inter-particle distance ($d > 100\,\mu$m) is much larger than the particle sizes, allowing the observation of extended microparticle clouds.
- The microparticle dynamics can be observed in real time since the time scales of the collective phenomena, for example, plasma waves or crystallization, are of the order of seconds or minutes.
- The Coulomb coupling parameter, that is, the ratio of the interaction energy to the thermal energy of the microparticles, covers a huge range: $\Gamma = Q^2/(dk_{\mathrm{B}}T_{\mathrm{d}}) = 1 - 10^5$, where Q is the microparticle charge, d is the inter-particle distance, and T_{d} is the temperature of the microparticles corresponding to their kinetic energy. Therefore, various phases (gas, liquid, solid) and phase transitions can be investigated.
- To some extent, the interaction between the microparticles is tuneable by changing the plasma parameters or applying external fields. For example, changing the ion density n_i or temperature T_i by pressure or power variation leads

---

Invited Paper: This work is based on an invited talk given at the Spring Meeting of the German Physical Society, 13–17 of March 2017, Bremen, Germany

to a change of the Debye screening length $\lambda_D \sim \sqrt{T_i/n_i}$ and therefore also of the inter-particle potential (Yukawa) $V(r) \sim \exp(-r/\lambda_D)/r$.

These features of complex plasma experiments enable unique investigations of equilibrium and non-equilibrium statistical physics, such as the equation of state, phase transitions, and transport coefficients.

In laboratory experiments on ground, the microparticles are levitated by the electric field in the plasma sheath above the bottom of the plasma chamber. Therefore, usually only microparticle clouds with a small vertical extension can be produced, although exceptions exist (see e.g. Steinmüller et al. [10]). However, ground experiments are of particular interest for the statistical physics of two-dimensional (2D) systems.[11] For example, the solid–liquid phase transition of these systems may show an intermediate phase, called hexatic, as predicted by the KTHNY theory.[12] Indications for such a phase have been found in the melting of 2D plasma crystals.[13]

Another more recent interesting example was investigated theoretically as well as experimentally by Ivlev et al.[14] Here, the thermodynamics of systems with a non-reciprocal interaction, that is, an interaction that does not obey Newton's Third Law ("action = reaction"), was considered. For example, wake potentials belong to this class if one just considers the force between a moving object in a medium and another behind it attracted by the wake, and neglects the atomistic interactions taking place in the medium. Such a situation is often found in complex plasmas where ion streaming generates a wake potential between two microparticles leading to string formation. Ivlev et al. investigated quasi-2D systems with two different particle sizes where the smaller particles are levitated just above the larger ones and attract the lower particles by a wake interaction. They showed that in such systems the upper particles have a different (higher) temperature than the lower ones although the system is in thermal equilibrium.

Extended three-dimensional (3D) systems, on the other hand, are studied best under microgravity conditions. Laboratory experiments on ground are strongly affected by gravity, as is also the case for other soft matter systems where the mesoscopic component is subjected to gravity effects such as sedimentation and convection. In particular, in the case of complex plasmas, there are the following disturbing effects:

- An electrostatic field, typically of the order of a few V/cm is necessary to levitate the charged microparticles.
- Such a field does not exist in the quasi-neutral bulk plasma but only in the plasma sheath. Therefore, only particle clouds of a few vertical layers can be produced, which are compressed by gravity. In addition, the plasma conditions in the sheath are complicated. For example, there exists ion streaming due to the electric field leading to a distortion of the Debye sphere around a microparticle and anisotropic interactions (wakes).
- The gravitational force is comparable to the inter-particle forces, changing the structure and dynamics of complex plasmas.
- Some experiments, in particular with large particles of the order 20 µm and larger, are impossible because the electric field in the plasma sheath is not strong enough to suspend these particles.

Therefore, microgravity experiments have been performed already since the 1990s onboard of the Russian space station MIR[15] and in sounding rockets (TEXUS).[16] Later, the experiments PKE-Nevedov (PK-3)[17] and PK-3 Plus[18] were operated successfully on the International Space Station (ISS) from 2001 to 2013. In 2014, the complex plasma facility PK-4 ("Plasmakristallexperiment 4")[19] was launched to the ISS. In addition, numerous parabolic flight experiments with different complex plasma devices were conducted.

2 | THE PK-4 PROJECT

Complex plasmas were mostly studied in compact plasma chambers using radio frequency (rf) discharges, as was the case also for PKE-Nefedov and PK-3 Plus. An alternative is dc discharges.[20] Preliminary experiments with complex dc plasmas were also performed under microgravity.[21] In 2002, the joint project of the Max-Planck-Institute for Extraterrestrial Physics (Garching) and the Joint Institute for High Temperatures (Moscow) PK-4 was started aiming at a complex dc experiment for the ISS. Laboratory set-ups and a parabolic flight rack were constructed, and experiments on ground and in nine parabolic flight campaigns were performed with funding from the German Aerospace Center (DLR). The aim of these experiments was to test and optimize protypes of an ISS facility and to conduct scientific experiments, which led to more than 20 peer-reviewed publications until now.

An example is self-excited plasma waves observed in parabolic flights, as shown in Figure 1.[19] The plasma frequency of the dust acoustic waves[22], given by

$$\omega_{pl} = \sqrt{\frac{4\pi\, Q^2 n_d}{m_d}} \tag{1}$$

where n_d is the microparticle density and m_d their mass, is of the order 10–100 Hz and hence observable by the naked eye. Even the dynamics of the individual particles within the waves, for example, surfing from wavefront to wavefront, can be studied.
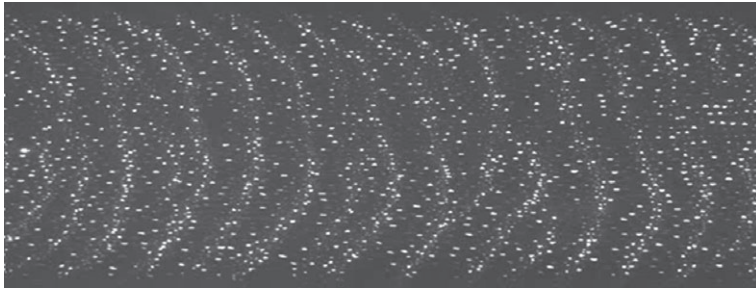
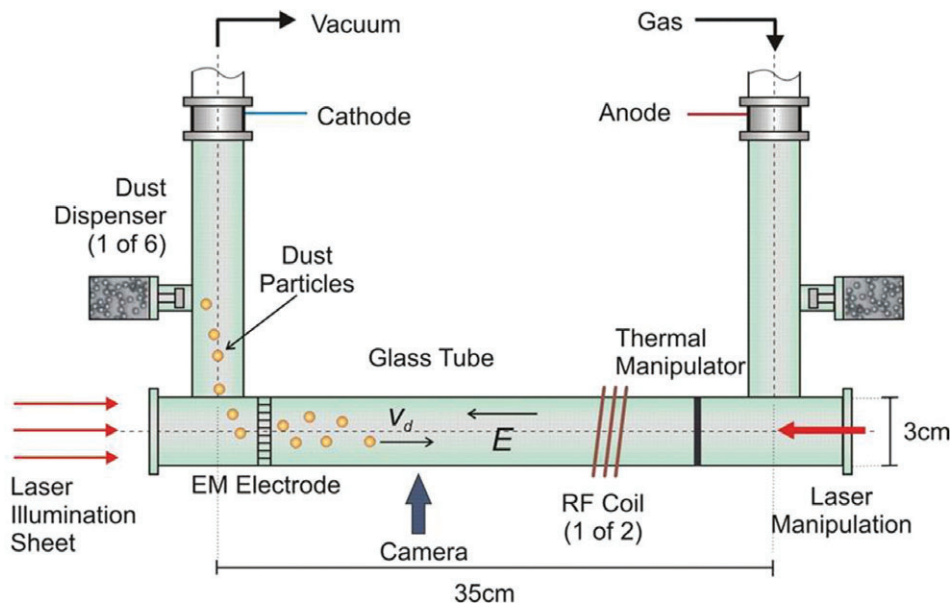FIGURE 1   Dust waves in PK-4 under microgravity

FIGURE 2   Sketch of the PK-4 plasma chamber

The parabolic flight set-up was used in nine parabolic flight campaigns from 2003 to 2012. At the same time, this set-up was used as an engineering model for the ISS flight model. The technical details of this facility are described in Pustylnik et al.[23].

In 2006, PK-4 became a project of the European Space Agency (ESA) involving more international scientists. In 2014, the flight model was launched from Baikonur with a Progress transporter to the ISS and accommodated in the European Columbus Module.

The heart of the PK-4 experiment is a U-shaped glass tube of 80 cm length and 3 cm diameter (Figure 2). At its end there are cylindrical dc electrodes powered by a high-voltage generator up to 3 kV producing the plasma. A gas/vacuum system provides a minimum gas pressure in the chamber of 10^{-3} Pa and argon or neon gas with pressures between 5 and 250 Pa. Two kinds of particle injectors (three shaker and three gas jet dispensers) are attached to the glass tube for injecting spherical melamine formaldehyde (MF) or silica particles of various diameters between 1 and 11 μm. A laser sheet (laser diode, 532 nm wavelength) illuminates the microparticles along the horizontal part of the tube, and two CCD cameras (2 MPixel each and frame rate 35–200 Hz) record the images. Both cameras are movable along and perpendicular to the glass tube, allowing the observation of the microparticles in the positive column of the discharge over a longitudinal range of 20 cm and scans across the tube for extracting 3D information. In addition, there is an overview camera for observing the plasma glow and a spectrometer for local plasma diagnostics.

PK-4 is not a dedicated experiment but rather a laboratory facility allowing the performance of many different measurements in a way as flexible as possible. Therefore, various devices are incorporated for particle manipulation such as trapping of the particles, accelerating the particles, or producing shock waves and shear flow. For this purpose, the dc can be changed into ac between 100 and 5,000 Hz by polarity switching. In addition, two external rf coils can be used for creating a combined dc/rf plasma, an internal ring electrode can be powered by short pulses for creating shock waves, an infrared laser diode (0–20 W) can produce shear flow by radiation pressure, and a thermal heating wire creates a temperature gradient for the thermophoretic transport of microparticles. In contrast to the previous ISS experiments PKE-Nefedov and PK-3 Plus, where in particular plasma crystals were studied in compact rf chambers, PK-4 is especially suited for flow experiments in complex plasma liquids due to its elongated chamber geometry.

The parabolic flight rack was transferred in 2015 to the University Giessen where it was reconstructed (Figure 3) for a parabolic flight campaign in 2016. The rack structure was completely redesigned, and one CCD camera was replaced by a modern CMOS
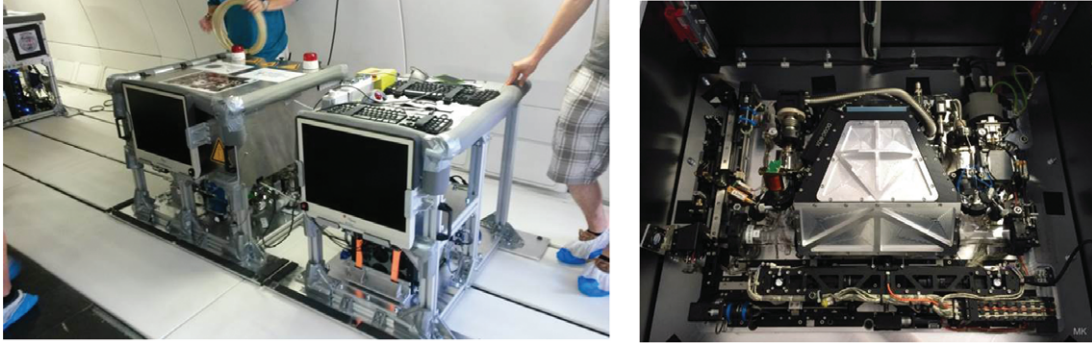
FIGURE 3 Parabolic flight set-up of PK-4: the racks (left) and the integrated base plate containing the plasma chamber (right)
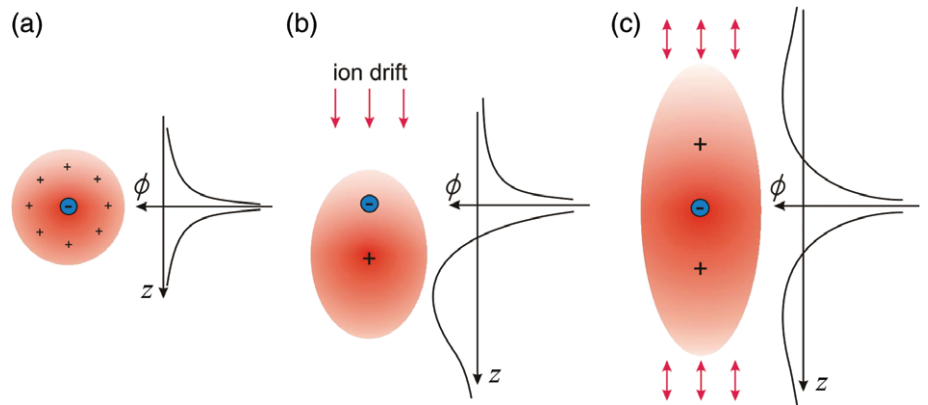

FIGURE 4 Particle potential in the case of (a) no field (a), (b) a dc field, and (c) an ac field

camera with a higher resolution and frame rate. This campaign was dedicated to two experiments, namely electrorheology and demixing.

3 | ELECTRORHEOLOGY

Electrorheological fluids are non-conducting liquids containing nano or microparticles that change their flow behaviour if an external electric field is applied. For example, the viscosity can be increased by several orders of magnitude, as used in brakes or shock absorbers. This effect is caused by inducing a dipole interaction between the particles leading to string formation.[24]

Complex plasmas can be used to simulate those systems by applying an external ac field. First experiments were done with PK-3 Plus onboard the ISS.[25] In Figure 4 the mechanism is sketched. In the absence of an electric field (a), the interaction potential of a negatively charged microparticle is given by the repulsive and isotropic Yukawa potential. In the presence of a dc field (b), an ion streaming is generated, leading to a non-reciprocal wake interaction between the particles corresponding to a non-Hamiltonian system. In the case of an ac field (c), with a frequency much larger than the dust plasma frequency[1] but much lower than the ion plasma frequency (a few MHz), the ions stream back and forth creating a symmetric ion wake around a particle (Hamiltonian system) within a stable particle cloud. The interaction potential is then given by a superposition of the repulsive Yukawa interaction and an attractive dipole–dipole interaction[26]:

$$W(r, \theta) \simeq Q^2 \left[\frac{\exp(-r/\lambda_{\mathrm{D}})}{r} - 0.43 \frac{M_{\mathrm{T}}^2 \lambda_{\mathrm{D}}^2}{r^3} (3\cos^2\theta - 1) \right],$$ (2)

where M_{T} is the Mach number, which is the ratio of ion drift velocity to thermal ion velocity.

In PK-4, electrorheological experiments under microgravity were performed in two parabolic flight campaigns in 2008 and 2009.[27] Here, a polarity switching frequency of 1,000 Hz was applied to the dc electrodes for generating a longitudinal electric ac field inside of the glass tube. In this way, a stable microparticle cloud was observed showing extended longitudinal strings (Figure 5). Because of the microgravity, the cloud was located in the centre of the tube where the radial electric field from the sheath of the glass walls does not disturb the string formation. The string formation was analysed by the scaling index analysis (see below) for detecting anisotropic structures in the particle system. Using the same parameters (particle size, gas pressure, current) in the pure dc mode, much less or no string formation was found. This was explained by the fact that non-Hamiltonian
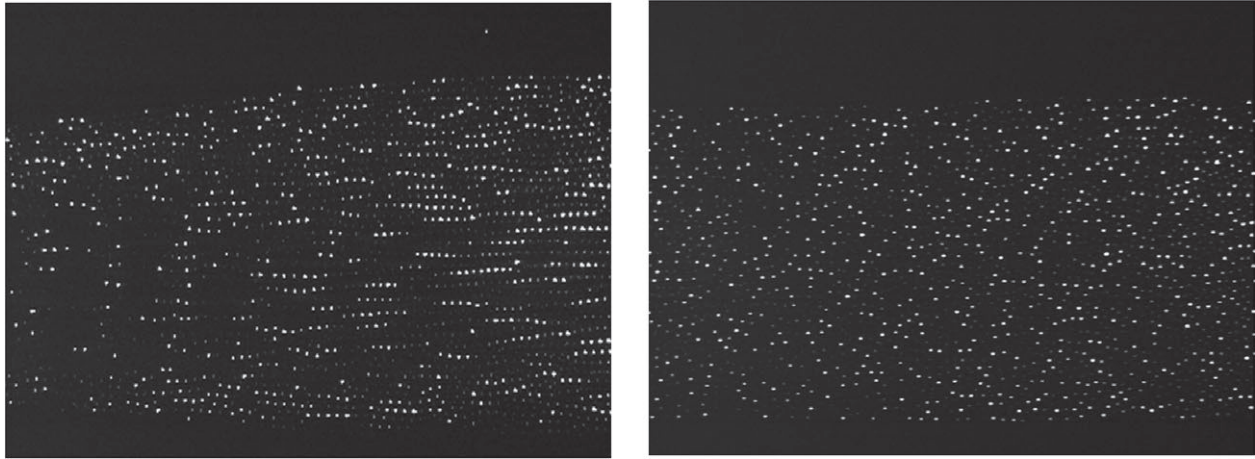
FIGURE 5 String formation in an ac field (left), and isotropic system in a dc field (right). The discharge current is 1 mA, the particle diameter is 6.86 μm, and the gas pressure is 60 Pa corresponding to a Mach number of 0.4
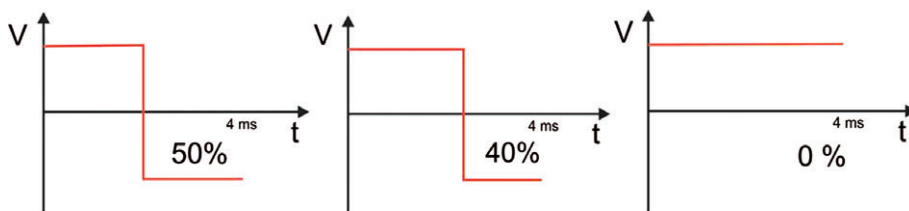

FIGURE 6 Duty cycle variation from an symmetric ac field (50%) to a dc field (0%)
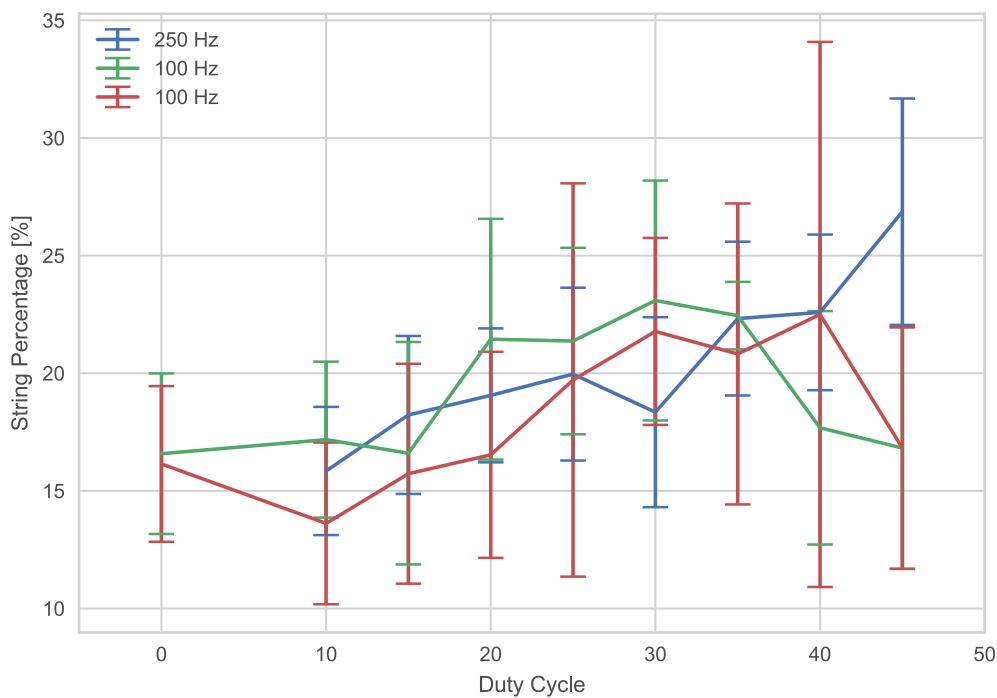

FIGURE 7 String formation depending on the duty cycle

systems (dc) are more sensitive to instabilities, preventing the string formation, than Hamiltonian ones (ac). These findings were confirmed by molecular dynamics (MD) simulations.

In the parabolic flight campaign in 2016, we were interested in the phase transition from a string fluid to a nearly isotropic one by changing the duty cycle of the polarity switching (Figure 6). Polarity switching frequencies of 100 and 250 Hz at a dc current of 1 mA and a gas pressure of 60 Pa with MF particles of 6.86 μm diameter were utilized. Using an analysis based on scaling indices and a neural network, as described below, it was found that the string formation decreased in the dc compared to the ac mode (Figure 7). However, the decrease was less pronounced than in the earlier experiments, which requires further investigations.
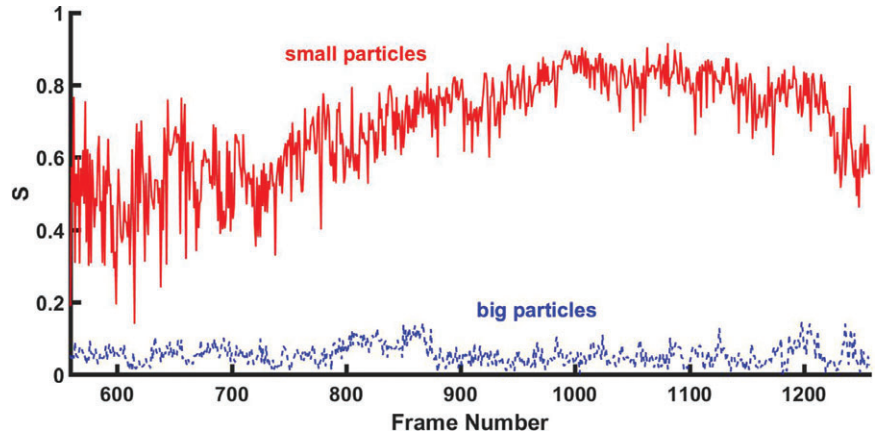
FIGURE 8 Lane formation analysis using the anistropic scaling index S at a gas pressure of $100\,\text{Pa}$ and a dc current in the polarity switching mode of $1\,\text{mA}$. $S = 1$ means perfect alignment, and $S = 0$ is random alignment

4 | DEMIXING

Phase separation of a system containing two different species takes place if there is an attractive interaction within the same species and a repulsive interaction between them like in water–oil mixtures. However, also a heterogeneous mixture with only repulsive particle interactions can demix if the repulsive force between particles of the same species is weaker than that between particles of different species.[28] So a complex plasma consisting of particles with different sizes (and therefore different charges), where all particles repel each other, can demix. This was shown using the experiment PK-3 Plus on the ISS.[29] Demixing starts if the radius of the smaller particles is less than ∼0.7 times the radius of the bigger ones.[28]

In the parabolic flight campaign with PK-4 in 2016, we filled two different particles (MF particles of $3.27\,\mu\text{m}$ diameter and silica particles of $2.06\,\mu\text{m}$ diameter) in one dispenser. This experiment is not possible on the ISS since the dispensers of the flight model contain only particles of one size and the astronauts have no access to the interior of the apparatus. On ground, the particles arrive in the field of view of the cameras already demixed, caused by a separation due to gravity because larger particles are located lower, i.e. closer to the bottom of the glass tube where the electric field is strong enough to levitate the larger particles. Therefore, only under microgravity conditions can one observe the binary particle mixture and its demixing.

The demixing proceeds via lane formation, i.e. the particles in the clouds penetrating each other arranging themselves in lanes, a generic process found in interpenetrating systems.[30] The lane formation was also observed in the parabolic flight experiments in the fall of 2016. The analysis of lane formation was done by using the scaling index method (see below). It was found that the small particles tended to form clear lanes, whereas the larger ones did not (Figure 8). Further analysis and interpretation of these results are in progress.

5 | IMAGE ANALYSIS

At the University of Giessen, various image analysis tools for identifying structures in complex plasmas have been adopted and developed further. To detect the particle positions in the images retrieved from the camera system, an algorithm due to Crocker and Grier [31] was used. From the particle positions, the crystalline lattices are determined by using various analysis methods,[10,32,33] which can also be used for the investigation of string and lane formation. Here we used the scaling index method.

5.1 | Scaling index method

The scaling index method has been successfully applied to characterize bone structures in medicine,[34] electrorheological complex plasmas,[25] and lane formation in complex binary plasmas.[30] The anisotropic scaling index characterizes the dimensionality of the local structure defined around a point $\mathbf{r}_i$ with a number of neighbours N. It is defined as follows:

$$\alpha(\mathbf{r}_i, R) = \frac{2 \sum_{j=1}^{N} (d_{ij}/R)^2 \exp(-(d_{ij}/R)^2)}{\sum_{j=1}^{N} \exp(-(d_{ij}/R)^2)} \tag{3}$$

The scale is denoted as R, and d_{ij} is the distance between two points $d_{ij} = |\mathbf{r}_i - \mathbf{r}_j|$, with j being the index of a neighbouring point. As stated before, the scaling index is a measure of the dimensionality with respect to the scale R. This means $\alpha(\mathbf{r}_i, R)$ is close to zero for point-like structures, close to 1 for line-like structures, and so on.[30,35,36]

In this work, especially the detection of line-like structures due to string formation in electrorheological plasmas and lane formation in binary mixtures is of interest. Because lanes and strings have a pronounced direction (see Figure 5) it is convenient to increase the sensitivity of the scaling index by using an aspect ratio ε (>1) in the direction of the vector $\mathbf{u} = (\cos\theta, \sin\theta)$ (due to symmetry effects, $-\pi/2 \leq \theta \leq \pi/2$). The distance of two points $\mathbf{r}_1 = (x_1, y_1)$ and $\mathbf{r}_2 = (x_2, y_2)$ is given in two dimensions after rotation and stretching as

$$d_{ij}(\varepsilon, \theta) = \sqrt{[(x_1 - x_2)\sin\theta - (y_1 - y_2)\cos\theta]^2 + \varepsilon^2[(x_1 - x_2)\cos\theta + (y_1 - y_2)\sin\theta]^2}. \tag{4}$$

This means the anisotropic scaling index[3] also depends on the aspect ratio ε and the angle, that is, $\alpha(\mathbf{r}_i, R, \varepsilon, \theta)$. This makes it possible to scan for anisotropic behaviour by varying R and θ.

To determine a "preferred" direction, for each particle i, it is convenient to maximize $\alpha(\mathbf{r}_i, R, \varepsilon, \theta_i + \pi/2) - \alpha(\mathbf{r}_i, R, \varepsilon, \theta_i)$. This will result in an angle θ_i, from which the "preferred" direction vector $\mathbf{u}_i = (\cos\theta_i, \sin\theta_i)$ can be determined. A global quantity of "laning" of the particles can be calculated using the global tensor T:

$$T = \frac{2}{N}\sum_{j=1}^{N} \mathbf{u}_j \otimes \mathbf{u}_j - \mathbb{1}. \tag{5}$$

Here, $\otimes$ denotes the Kronecker product and $\mathbb{1}$ the identity matrix. The largest eigenvalue of T is called the laning-order parameter S. If all particles are perfectly aligned, $S = 1$; if they are in complete random phase, $S = 0$. Corresponding to the laning-order parameter, the eigenvector $\langle\mathbf{u}\rangle$ can be determined. The global laning angle Θ is defined as

$$\cos\Theta = \langle\mathbf{u}\rangle\mathbf{e}_x \tag{6}$$

where $\mathbf{e}_x$ is the unit vector in the x-direction, $\mathbf{e}_x = (1, 0)$. In case of laning, $\Theta = 0$, and in case of isotropic distribution $\Theta = \pi/2$.[30,35,36]

5.2 | Demixing

To analyse the demixing, the different particles species have to be distinguished by their size. When illuminated by the laser sheet, the big particles reflect more light than the small particles. Furthermore, the small particles move through the cloud of the rather stationary big ones. Because of the movement and the exposure time, they appear as tracks in the recorded picture, whereas the big ones create only a bright dot. Both criteria (the overall brightness and the ratio of the length to the width of the particle images) allow us to distinguish between small and big particles.[30]

For the investigation of demixing, a region of 7.5×7.5 mm^2 was chosen, where about 350 small and 1,000 big particles were identified. During the demixing process, the small particles create lanes to penetrate the cloud of the big ones. To describe this lane formation mathematically, the anisotropic scaling index with a stretching factor of $\varepsilon = 5$ was applied. The rotational angle was calculated numerically in the range $-\pi/2$ to $+\pi/2$ with a resolution of $\pi/80$. To give reasonable results, the scale R has to be some multiple of the inter-particle distance. Therefore, we used $R = d_{nn} \times 15$, where d_{nn} is the average distance between the nearest neighbours. Figure 8 shows the evolution of the laning-order parameter S calculated for each individual frame.

For the small particles, the global laning angle is $\Theta_s = 0.05 \pm 0.03$ and for big particles $\Theta_b = 1.07 \pm 0.47$ (in units of radians), indicating a strong lane formation of the small particles, whereas the bigger ones are distributed in a more isotropic manner.

5.3 | Local string classification

For future investigations we will train a neural network using the sklearn library[37] to discriminate between particles in a "string" and particles outside a string (see Figure 5). For this discrimination, we calculate the anisotropic scaling index α for six different angles θ_l and scales R_k. This leads to a 36-dimensional vector $\alpha(\mathbf{r}_i, R_k, \theta_l)$. This vector can now be used to identify particles in strings.

Because strings are not highly symmetric like crystals,[32,33] we use a large neighbourhood of six average neighbour distances d_0 around the particle i. The scales R_k are six equidistant numbers from 1–3 neighbour distances: $R_k \in d_0 \ldots 3d_0$. The six angles are calculated in the range $\theta_l \in -\pi/4 \ldots \pi/4$. The aspect ratio is constant ($\varepsilon = 5$).

To train the neural network, we need labeled data where it is exactly known whether a particle is in a string or not. To achieve this, we generate artificial data that represent the occurrence of strings in a dusty plasma. The artificial data consist of strings and random particles on a grid (see Figure 9a). To emulate disturbances of the particles, a normal-distributed noise between 3% and 13% of the average particle distance is added to the data. In this artificial dataset, we know exactly which particles are part of a string, and we use this to teach the neural network how to discriminate these particles in our experimental data. By using another set of artificial data, we can test the accuracy of the classification, which results in 91% correctly classified particles.
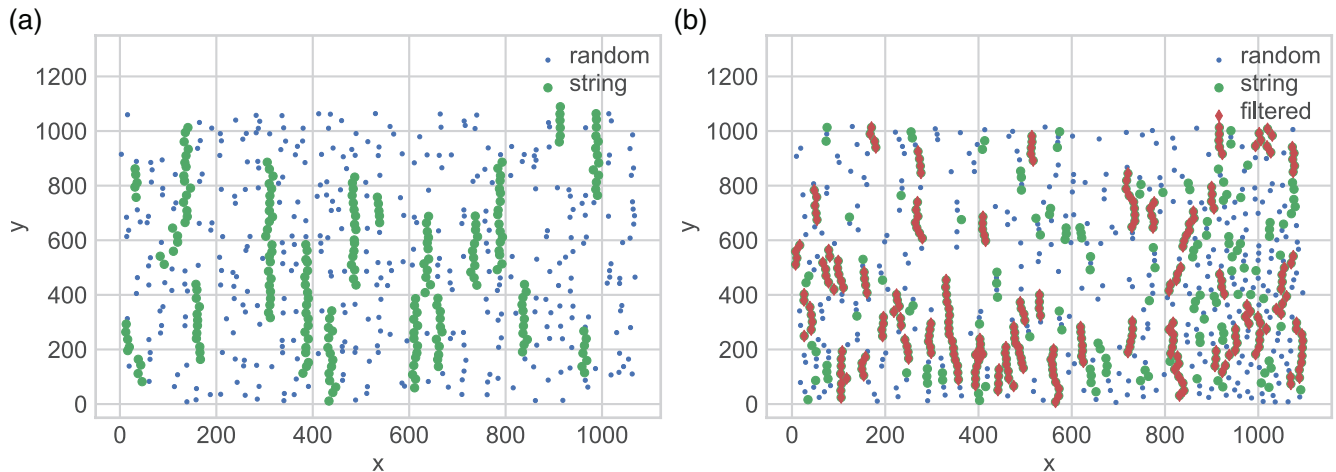
FIGURE 9 (a) Example for training data at 13% of noise. (b) Result from local classification on the measured data. Particles directly retrieved from the classification are in green, and the identified strings above a length of three particles are in red

With this state-of-the-art method of classification, we are now able to locally measure whether a particle is part of a string. An example of the classification is shown in Figure 9b. It is apparent that the approach does not perform perfectly, and a significant number of falsely classified particles is in the data. To improve this, we post-process the particles by connecting string particles with their nearest neighbours and use a custom community detection algorithm to find chains in the string particles. With the identification of the chains, we can filter out particles that are in a chain shorter than four particles, which is also shown in Figure 9b. This leads to a more satisfactory result. The percentage of particles in a string can then be calculated as in Figure 7.

6 | CONCLUSIONS

PK-4 allows novel experiments and investigations with extended 3D complex plasmas under microgravity conditions. In particular, fluid systems and phase transitions can be studied on the microscopic and dynamic level in real time and great detail. Experiments on board the ISS in long-term and high-quality microgravity started in 2015 and will be conducted for several years further on. After all, parabolic flight experiments in short-term reduced gravity are useful since they can be complementary to the ISS experiments where the experimental apparatus cannot be changed. For example, in parabolic flights we can use particle mixtures in a dispenser.

We investigated the phase transition in electrorheological plasmas and the lane formation in the demixing process of binary particle systems in parabolic flight experiments in 2016 and analysed the results using powerful image analysis tools. Preliminary results were presented in this paper. However, further analysis and additional microgravity experiments are required.

REFERENCES

[1] C. K. Goertz, *Rev. Geophys.* **1989**, *27*, 271.
[2] A. Bouchoule Ed., *Dusty Plasmas*, John Wiley, Chichester **1999**.
[3] V. E. Fortov, A. V. Ivlev, S. A. Khrapak, A. G. Khrapak, G. E. Morfill, *Phys. Rep.* **2005**, *421*, 1.
[4] G. E. Morfill, A. V. Ivlev, *Rev. Mod. Phys.* **2009**, *81*, 1353.
[5] A. V. Ivlev, H. Loewen, G. E. Morfill, C. P. Royall, *Complex Plasmas and Colloidal Dispersions: Particle-resolved Studies of Classical Liquids and Solids*. Series in Soft Condensed Matter, Vol. *5*, World Scientific, New Jersey **2012**.
[6] J. H. Chu, I. Lin, *Phys. Rev. Lett.* **1994**, *72*, 4009.
[7] H. Thomas, G. E. Morfill, V. Demmel, J. Goree, B. Feuerbacher, D. Moehlmann, *Phys. Rev. Lett.* **1994**, *73*, 652.
[8] Y. Hayashi, S. Tachibana, *Jpn. J. Appl. Phys.* **1994**, *33*, L804.
[9] A. Melzer, T. Trottenberg, A. Piel, *Phys. Lett. A* **1994**, *191*, 301.
[10] B. Steinmüller, C. Dietz, M. Kretschmer, M. H. Thoma, *Phys. Plasmas* **2017**, *24*, 033705.
[11] V. Nosenko, S. K. Zhdanov, A. V. Ivlev, C. A. Knapek, G. E. Morfill, *Phys. Rev. Lett.* **2009**, *103*, 015001.
[12] B. I. Halperin, D. R. Nelson, *Phys. Rev. Lett.* **1978**, *41*, 121; D. R. Nelson, B. I. Halperin, *Phys. Rev. B* **1979**, *19*, 2457; A. P. Young, *Phys. Rev. B* **1979**, *19*, 1855.
[13] H. M. Thoma, G. E. Morfill, *Nature* **1996**, *379*, 806.

[14] A. V. Ivlev, J. Bartnick, M. Heinen, C.-R. Du, V. Nosenko, H. Loewen, *Phys. Rev. X* **2015**, *5*, 011035.

[15] V. E. Fortov, A. P. Nefedov, O. S. Vaulina, A. M. Lipaev, V. I. Molotkov, A. A. Samaryan, V. P. Nikitski, A. I. Ivanov, S. F. Savin, A. V. Kalmykov, A. Ya. Solov'ev, P. V. Vinogradov, *JETP* **1998**, *87*, 1087.

[16] G. E. Morfill, H. M. Thomas, U. Konopka, H. Rothermel, M. Zuzic, A. Ivlev, J. Goree, *Phys. Rev. Lett.* **1999**, *83*, 1598.

[17] A. P. Nefedov, G. E. Morfill, V. E. Fortov, H. M. Thomas, H. Rothermel, T. Hagl, A. V. Ivlev, M. Zuzic, B. A. Klumov, A. M. Lipaev, V. I. Molotkov, O. F. Petrov, Y. P. Gidzenko, S. K. Krikalev, W. Shepherd, A. I. Ivanov, M. Roth, H. Binnenbruck, J. A. Goree, Y. P. Semenov, *New J. Phys.* **2003**, *5*, 33.

[18] H. M. Thomas, G. E. Morfill, V. E. Fortov, A. V. Ivlev, V. I. Molotkov, A. M. Lipaev, T. Hagl, H. Rothermel, S. A. Khrapak, R. K. Suetterlin, M. Rubin-Zuzic, O. F. Petrov, V. I. Tokarev, S. K. Krikalev, *New J. Phys.* **2008**, *10*, 033036.

[19] M. H. Thoma, M. A. Fink, H. Höfner, M. Kretschmer, S. A. Khrapak, S. V. Ratynskaia, V. V. Yaroshenko, G. E. Morfill, O. F. Petrov, A. D. Usachev, A. V. Zobnin, V. E. Fortov, *IEEE Trans. Plasma Sci.* **2007**, *35*, 255.

[20] V. I. Molotkov, O. F. Petrov, M. Y. Pustylnik, V. M. Torchinskii, V. E. Fortov, A. G. Khrapak, *High Temp.* **2004**, *42*, 827.

[21] V. E. Fortov, A. P. Nefedov, O. S. Vaulina, O. F. Petrov, V. I. Molotkov, V. M. Torchinskii, V. E. Fortov, A. V. Chernyshev, A. M. Lipaev, A. I. Ivanov, A. Y. Kaleri, Y. P. Semenov, S. V. Zaletin, *JETP* **2002**, *95*, 673.

[22] N. N. Rao, P. K. Shukla, M. Y. Yu, *Planet. Space Sci.* **1990**, *38*, 543.

[23] M. Y. Pustylnik, M. A. Fink, V. Nosenko, T. Antonova, T. Hagl, H. M. Thomas, A. V. Zobnin, A. M. Lipaev, A. D. Usachev, V. I. Molotkov, O. F. Petrov, V. E. Fortov, C. Rau, C. Deysenroth, S. Albrecht, M. Kretschmer, M. H. Thoma, G. E. Morfill, R. Seurig, A. Stettner, V. A. Alyamovskaya, A. Orr, E. Kufner, E. G. Lavrenko, G. I. Padalka, E. O. Serova, A. M. Samokutyayev, S. Christoforetti, *Rev. Sci. Instrum.* **2016**, *87*, 093505.

[24] W. M. Winslow, *J. Appl. Phys.* **1949**, *20*, 1137.

[25] A. V. Ivlev, G. E. Morfill, H. M. Thomas, C. Räth, G. Joyce, P. Huber, R. Kompaneets, V. E. Fortov, A. M. Lipaev, V. I. Molotkov, T. Reiter, M. Turin, P. Vinogradov, *Phys. Rev. Lett.* **2008**, *100*, 095003.

[26] R. Kompaneets, U. Konopka, A. V. Ivlev, V. Tsytovich, G. Morfill, *Phys. Plasmas* **2007**, *14*, 052108.

[27] A. V. Ivlev, M. H. Thoma, C. Raeth, G. Joyce, G. E. Morfill, *Phys. Rev. Lett.* **2011**, *106*, 155001.

[28] A. V. Ivlev, S. K. Zhdanov, H. M. Thomas, G. E. Morfill, *EPL* **2009**, *85*, 45001.

[29] A. Wysocki, C. Räth, A. V. Ivlev, K. R. Sütterlin, H. M. Thomas, S. Khrapak, S. Zhdanov, V. E. Fortov, A. M. Lipaev, V. I. Molotkov, O. F. Petrov, H. Löwen, G. E. Morfill, *Phys. Rev. Lett.* **2010**, *105*, 045001.

[30] K. R. Sütterlin, A. Wysocki, A. V. Ivlev, C. Räth, H. M. Thomas, M. Rubin-Zuzic, W. J. Goedheer, V. E. Fortov, A. M. Lipaev, V. I. Molotkov, O. F. Petrov, G. E. Morfill, H. Löwen, *Phys. Rev. Lett.* **2009**, *102*, 085003.

[31] J. C. Crocker, D. G. Grier, *J. Colloid Interface Sci.* **1996**, *179*(1), 298.

[32] C. Dietz, M. H. Thoma, *Phys. Rev. E* **2016**, *94*, 033207.

[33] C. Dietz, T. Kretz, M. H. Thoma, *Phys. Rev. E* **2017**, *96*, 011301(R).

[34] C. Räth, R. Monetti, J. Bauer, I. Sidorenko, D. Müller, M. Matsuura, E-M. Lochmüller, P. Zysset, F. Eckstein, *New J. Phys.* **2008**, *10*, 125010.

[35] K. Jiang, C. R. Du, K. R. Suetterlin, A. V. Ivlev, G. E. Morfill, *EPL* **2010**, *92*, 65002.

[36] K. R. Sütterlin, H. M. Thomas, A. V. Ivlev, G. E. Morfill, V. E. Fortov, A. M. Lipaev, V. I. Molotkov, O. F. Petrov, A. Wysocki, H. Lowen, *IEEE Trans. Plasma Sci.* **2010**, *38*(4), 861.

[37] F. Pedregosa, *J. Mach. Learn. Res.* **2011**, *12*, 2825.

Erklärung

Ich erkläre: Ich habe die vorgelegte Dissertation selbstständig und ohne unerlaubte fremde Hilfe und nur mit den Hilfen angefertigt, die ich in der Dissertation angegeben habe. Alle Textstellen, die wörtlich oder sinngemäß aus veröffentlichten Schriften entnommen sind, und alle Angaben, die auf mündlichen Auskünften beruhen, sind als solche kenntlich gemacht. Ich stimme einer evtl. Überprüfung meiner Dissertation durch eine Antiplagiat-Software zu. Bei den von mir durchgeführten und in der Dissertation erwähnten Untersuchungen habe ich die Grundsätze guter wissenschaftlicher Praxis, wie sie in der „Satzung der Justus-Liebig-Universität Gießen zur Sicherung guter wissenschaftlicher Praxis" niedergelegt sind, eingehalten.

_____   _____
        Ort, Datum   Benjamin Steinmüller